Politecnico di Milano
Physics Department
Doctoral Programme in Physics

Enhanced Infrared Spectroscopies

Doctoral Dissertation of:
Francesco Rusconi

Supervisor:
Prof. Paolo Biagioni

Tutor:
Prof. Marco Finazzi

The Chair of the Doctoral Program:
Prof. Marco Finazzi

2023 – XXXIV cycle

Contents

List of Figures

List of Tables

Abstract

Since its first discovery, infrared (IR) light has been studied for its peculiar interaction with matter. This comes from its capability to excite molecular vibrations, which define absorption lines specific to the studied specimen, providing a "molecular fingerprint". For this reason, IR spectroscopic techniques represent one of the most employed tools to chemically characterize a sample. These techniques benefit also from a well-developed instrumental technology, and typically involve quick, low-cost and non-invasive measurements, making their employment favorable in industrial and security settings. However, the interaction between IR light and molecules is generally weak, because the typical IR wavelength is much larger than the dimensions of molecules. In order to better mediate this interaction, we employ nanostructured systems. The focus in this thesis' title is on the word "enhanced". I will present and discuss how we designed, characterized and employed nanostructured systems properly tailored to have electromagnetic resonances and enhance the selective detection of a given molecule. Indeed, these resonances confine the fields in localized hotspots, which are very sensitive to the surrounding environment and have characteristic dimensions similar to the ones of molecules. In this thesis, I will discuss two works: the modelling of a tip-enhanced technique, used to probe the IR absorption on the nanoscale, and the design of a platform exploiting high-quality dielectric resonances in the mid-IR. Both works aim to provide a technological advancement in the field of infrared spectroscopies. The first work gives a solid theoretical background to the technique under study, in particular pointing out the key ingredients in the heat conduction at the nanoscale. The platform demonstrated in the second work can be employed in vibrational sensing, but presents also intriguing perspective extensions, e.g. in enhanced chiroptical detection in the mid-IR. In general, the systems I am going to discuss are analyzed under several points of view, e.g. the mechanical, thermal and material points of view, but I will mainly focus on their optical properties. Indeed, the aim of my research presented here is to model and enhance the bridge between light and matter at the nanoscale, providing valid ways to probe molecules optically and retrieve strong vibrational signals.

Keywords: infrared spectroscopy; nanoantennas; tip-enhanced spectroscopy; molecular sensing.

Chapter 1

Introduction to infrared spectroscopies

1.1 Brief history of infrared spectroscopy

In the context of light-matter interaction, infrared (IR) radiation plays a crucial role, since it can excite and probe molecular vibrations. IR light was first discovered in the year 1800, by William Herschel. He used a dispersive prism to separate the spectrum of the visible light and, with a blackened thermometer, measure the heating associated to the absorption of each colour. When he moved the thermometer beyond the red rays, he measured an even larger increase in temperature, though there was no visible light. From this observation, the existence of an invisible light able to carry heat, at longer wavelengths than visible light, was theorized. It is significative that a light-matter mechanism triggered the discovery of IR light, already suggesting its key importance in the study of matter, down to the basic constituents of the materials. Indeed, scientists soon discovered its peculiar interaction with matter and since the second part of the XIX century IR light has been globally employed to characterize the chemical composition of many materials. The first vibrational spectra were measured in 1881 by Abney and Festing, in the so called near-infrared (NIR) region, the closest IR region to the visible light (extending from 780 nm to 2.5 µm) [15]. From these spectra, they already observed that the presence of a specific chemical bond would cause the same absorption peaks even in different compounds. Thus, the IR spectra were used as "fingerprint" of the molecules under study, since they carried the information necessary to label the chemical bonds in the molecules. This observation exposed the underlying great potential of IR spectroscopy, motivating many efforts to study and characterize materials by means of vibrational spectroscopy, which ended in an empirical classification based on the repetition of known absorption features. These preliminary works mainly targeted organic compounds (carbon-carbon or carbon-hydrogen based materials). Thanks to the efforts of Angstrom, Julius and Coblentz among others, in the first years of the XX century more than one hundred organic materials were catalogued, with spectral characterizations up to 25 µm, reaching the so-called mid-infrared (MIR) region. All these efforts

already showed the crucial role of the infrared light in the investigation of matter.

For this reason, in parallel, optical setups dedicated to IR spectroscopy were developed. Complete schemes were already present at the end of XIX century, but the XX century witnessed a great technological step, with the advent of IR interferometers. The first IR interferometer was developed in 1937 (by Erwin Lehrer and Karl Friedrich Luft, for the company Badische Anilin- and Soda-Fabrik), then improved to a double-beam interferometer in 1942. These models were primarily used to chemically characterize gas samples, in a much easier and simpler way than the methods used previously. This demonstration, coupled with the technological advancement, led to a transition towards industrial settings. By the 1960s, IR interferometers were used globally. The successive integration of computers represented the last big technological leap in IR spectroscopy. Indeed, computers allowed to compute easily Fourier-transformed interferograms and retrieve the absorption spectra, increasing the popularity of Fourier-Transform Interferometers (FTIR), which soon became the norm in IR spectroscopy. One of the following sections will be dedicated to the functioning principles of a FTIR, given its relevance.

Nowadays, IR spectroscopy is employed in all kinds of settings, from laboratory environment to mass-production sites, everywhere in the world [1]. Indeed, it represents a rapid, simple, cost-effective and direct characterization of the material under study. Moreover, it does not require complex procedure in the sample preparation and can study samples in solid, liquid or gaseous state. Another advantage is that IR setups, FTIR above all, are often commercial and widespread systems, and thus, user-friendly, sustained by a strong background knowledge. The simplicity of IR spectroscopy extends also to the data analysis procedure: indeed, an IR spectrum probes the direct absorption of the light, which is a linear phenomenon and easy to interpret.

Overall, by employing IR spectroscopy one can easily obtain meaningful information about the chemical composition of a material. For its qualities, it is often employed in a rather vast range of settings, i.e. characterization of unknown materials, quality control, detection of hazardous substances, both in research, industrial and security settings.

1.2 Infrared absorption

IR spectroscopy is based on the peculiar interaction between the IR light, capable to excite molecular vibrations, and matter. The spectral features correspondent to the molecular vibrations give a distinctive label for the studied compounds: the same bands appear whenever the same chemical bonds are present. The complete set of absorption bands forms the so-called "molecular fingerprint" of the sample. Indeed, by looking at these spectral features, one can recognize and reconstruct the chemical composition of the given specimen. In this context, the spectral region where fundamental molecular vibrations fall is called "fingerprint region", extending between 5 and 15 µm.

In this section, we will discuss the physical principles dictating the interaction between IR light and molecules. First of all, let us consider the motion of a molecule composed by n atoms. Since every atom can move along each dimension of space, the molecule possess $3n$ degrees of freedom. These are divided into translational, rotational

and vibrational degrees of freedom. We are interested in the vibrational modes, which are characterized by a change in the interatomic distance. The translations and rotations instead keep the latter fixed. These modes interest each axis for a total of $3 + 3 = 6$ degrees of freedom. Thus, the remaining $3n - 6$ degrees of freedom are vibrational. Mechanically, we can describe the atoms as a mass, and their bonds as a spring [1, 16, 17]. In this picture, the vibration of a diatomic molecule can be described by the harmonic motion:

$$x(t) = x_0 \cos(2\pi\nu t + \phi), \tag{1.1}$$

where $x(t)$ is the displacement of the oscillating atom from equilibrium, x_0 the amplitude of the oscillation, f the frequency of oscillation and ϕ the phase. The frequency of the oscillation can be written as:

$$\nu = \frac{1}{2\pi}\sqrt{k(\frac{1}{m_1} + \frac{1}{m_2})}, \tag{1.2}$$

where m_1 and m_2 are the masses of the two atoms. This frequency is a function of the masses of the atoms and the elastic constant of the bond, which are specific of the molecule considered. The atoms oscillate with the same frequency, but different amplitude, keeping the centre of mass in its position. Following this description, both vibrating atoms are described by a harmonic potential energy of the form $U = \frac{1}{2}kx^2$. With this potential, quantum mechanics predicts that the molecule can only assume discrete levels of energy:

$$E_i = h\nu(n + 1/2) \quad n = 0, 1, 2.... \tag{1.3}$$

The spacing between two levels, $\Delta E = h\nu$, gives an estimate of the typical energy interesting a vibrational transition, which falls in the IR part of the radiation spectrum. In a harmonic potential, the energy levels are equally distant, however a more realistic description takes into account an anharmonic potential, for which the energy levels are not equally distant, showing a smaller spacing at high energies. In order to be excited, and undergo a vibrational transition, the molecule needs to acquire energy. This can be obtained with the interaction of an electromagnetic field. To describe this interaction, the electric properties of the molecule have to be considered. Indeed, the interaction between light and molecules is possible only when molecules possess a non-null electric dipole moment, and the molecular vibration corresponds to an oscillating dipole. On a qualitative level, it can be explained as the electromagnetic wave coupling with the molecular dipole, making it vibrate along one of its modes. Even electrically neutral molecules often present a dipole moment, coming from the partial charges on the atoms, arising in polar bonds. These partial charges can be effectively modelled as point charges positioned at the ends of the bond, retrieving the dipolar distribution. On the other hand, molecules showing a null dipole moment, i.e. homonuclear molecules, such as H_2, O_2 or P_4, cannot be investigated through direct IR absorption. These types of molecules are typically examined by means of Raman spectroscopy, a complementary technique to IR spectroscopy, which does not detect direct IR absorption. Raman spectroscopy

will be briefly discussed in the section 1.5. These considerations can be summarized in a selection rule for IR spectroscopy: only the vibrations causing a change in the dipole moment of the molecule are IR active [1, 16, 17]. Indeed, it can be demonstrated that:

$$I_{\mathrm{IR}} \propto \left(\frac{\partial \mu}{\partial Q}\right)^2 \tag{1.4}$$

where I_{IR} is the IR absorption intensity, μ is the dipole moment of the molecule and Q the vibrational coordinate. So, the intensity of IR absorption is proportional to the square of the change in the dipole moment.

IR absorption is observed when the electromagnetic fields oscillate with a frequency matching the one of a vibrational mode. Energetically this means that a photon of energy $h\nu$ is absorbed by the molecule, which uses that energy to vibrate. Given the discrete nature of these modes, the IR light-molecule interaction has a resonant behavior. Thus in an IR spectrum, the features corresponding to molecular vibrations appear as peaks at the resonant frequency.

1.3 Experimental observation of IR absorption

In a typical IR spectroscopic experiment, a broadband light with intensity $I_0(\bar{\nu})$ is shined upon a sample, then the transmitted intensity $I(\bar{\nu})$ is collected [1]. The reference intensity $I_0(\bar{\nu})$ is usually collected by removing the sample from the optical path. The two quantities are then compared by their ratio, which defines the transmittance of the sample:

$$T(\bar{\nu}) = \frac{I(\bar{\nu})}{I_0(\bar{\nu})}. \tag{1.5}$$

The transmittance is dependent on the wavenumber (or the wavelength), so a spectrum is retrieved. In certain situations, the transmittance is not the best quantity to measure, e.g. some samples are deposited over strongly reflecting substrates, so the transmitted intensity is low. For this resaon, the reflecance of the sample is also often studied: $R(\bar{\nu}) = \frac{I_{\mathrm{refl}}(\bar{\nu})}{I_{0,\mathrm{refl}}(\bar{\nu})}$. In this case, the reference $I_{0,\mathrm{refl}}$ is obtained by putting a perfect reflector in place of the sample, e.g. a gold mirror in the IR.

A typical IR spectrum presents sharp dips, which mark the excitation of molecular vibrations, while elsewhere it is relatively flat. Since the frequency of these features depends only on properties specific to the chemical bond (masses of the atoms, elastic constant of the bond), the absorption dip represents a label for it. The most common and significative vibrational modes are reported in IR databases, which make them easy to recognize. Fig.? reports some of them. By analysing the IR spectrum and the spectral position of the vibrational modes, one can reconstruct the chemical composition of the sample. So, IR spectroscopy is a valid tool in the chemical characterization of an unknown substance. The information coming from the IR spectrum can also be used backwards: one can use the frequency of the absorption peaks to determine the physical properties of a chemical bond, like the masses of the atoms or its elastic constant.

We have discussed the frequency of the peaks, but not their amplitude. The amplitude of the absorption peaks does not only depend on the material properties, but also on the quantity of matter. Indeed, by Lambert-Beer law we have: $T(\bar{\nu}) = \frac{I(\bar{\nu})}{I_0(\bar{\nu})} = \exp(-\alpha d)$, where α is the absorption coefficient and d the thickness of the material. This leads to another significant quantity, the absorbance: $A = -\log(1/T) = \alpha d$. IR spectroscopic data are often reported in this way, from which one can extrapolate α or d.

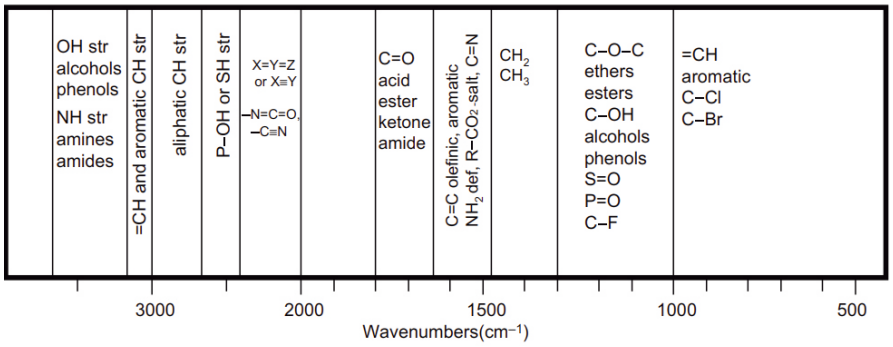

Figure 1.1: A chart reporting the spectral position of fundamental molecular vibrations. Adapted from ref. [1].

1.4 The Fourier-Transform Infrared Spectrometer

The Fourier-Transform Infrared (FTIR) spectrometers are one of the most employed set-ups to perform IR spectroscopy. Indeed, nowadays FTIR spectrometers are commercially available as standard and stand-alone set-ups, which can be found in laboratory as well as industrial settings. A typical FTIR measurement is versatile, since it can probe solid, liquid and gaseous samples, simple and fast, qualities which are particularly appealing for everyday standard spectroscopy.

We can picture a FTIR spectrometer starting from the configuration of a Michelson interferometer, to describe its working principle [1, 18]. A Michelson interferometer is composed by a light source, a beam splitter, a fixed mirror and a movable mirror (fig.1.2). The motion of the movable mirror changes the length of one optical path of the interferometer. Light travelling through that optical path is delayed respect to the other one (governed by the fixed mirror) at the detector, thus two beams interfere. This creates the interferometric pattern measured by the detector. In a typical FTIR measurement, one interferometric mirror moves with a constant speed, so that the optical path difference changes continuously. This translates into a sinusoidal interfering pattern at the detector. Since the illumination typically comes from a broadband source, the wavelengths of the illumination interfere differently. The maximum of intensity is measured when there is no difference between the two optical paths (the so-called zero path difference condition), which corresponds to a strong peak at the centre of the interferogram. At the sides of this peak, the interferogram presents a less intense modulation, resulting

from the sum of all the interference patterns of the source wavelengths, which are not in phase. This interferometric pattern, numerically, corresponds to the Fourier transform of the light intensity spetrum. So after collection, the interferogram is Fourier-transformed and the spectrum is retrieved.

The interferometric optical path difference is measured by employing a laser, typically a He:Ne laser. When it is shined in the interferometer, it also produces an interferometric pattern, with maxima separated by the laser wavelength (for He:Ne, $\lambda = 633$ nm). This represents the ruler for the optical path difference, so that the IR signal is collected et every maximum of the laser interferogram. In the end, this allows one to relate each point of the sample interferogram to the proper optical path difference.

An important aspect of FTIR spectroscopy is the spectral resolution, the smallest wavelength (or frequency) difference that can be resolved by the interferometer. In wavenumber, the spectral resolution corresponds to the inverse of the maximum optical path difference: $\Delta\bar{\nu} = \frac{1}{\Delta l_{\max}}$. Nowadays, commercial FTIR setups can resolve spectral differences below 1 cm^{-1}.

The main advantages of employing a FTIR spectrometer are:

- Felglett's advantage, which comes from multiplex detection. Indeed, the simultaneous collection of information at several wavelengths increases the signal-to-noise ratio, which in a measurement is mainly limited by the detector noise.

- Connes' advantage, arising from the use of a laser to measure the optical path difference, which ultimately determines the accuracy in the wavelength scale. The use of a laser guarantees a very accurate measurement of the mirror movement.

- Jacquinot's advantage, interesting the instrument's throughput. Indeed, this depends on the diameter of the collimated IR beam. The diameter of the beam is only limited by a single circular aperture, used to control its convergence. Moreover, all the light is collected by a single detector.

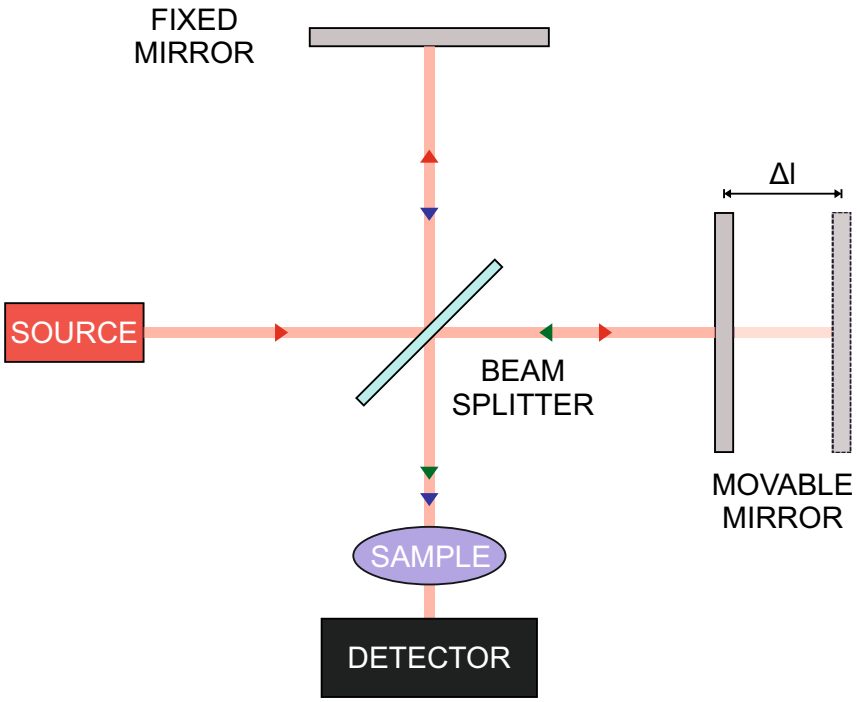

Figure 1.2: Sketch of a Michelson interferometer, representing the functioning of a FTIR spectrometer.

1.5 Raman spectroscopy vs IR spectroscopy

For sake of completeness, we should mention that another important technique used to investigate molecular vibrations is Raman spectroscopy. Even if it covers the same energy range of IR spectroscopy, this technique typically gives complementary information with respect to IR absorption. Given the importance of Raman spectroscopy, it is discussed in this paragraph, even if it is not object of this thesis.

Raman spectroscopy is a scattering technique [16]. This is the first difference with IR spectroscopy, which directly probes the absorption of molecules. In Raman scattering, the light, typically in the ultraviolet or visible spectral range, interacts with a molecule. Thus, the molecule is brought to an excited state and can re-emit light at the same frequency, corresponding to Rayleigh scattering, or at a different frequency. In this case, after the whole process, the molecule can access a different vibrational level from the initial one, thanks to the inelastic interaction with the higher-energy photon. This is the so-called Raman spectroscopy. The difference between input and output frequency gives information on the energy of a vibrational excitation.

Raman spectroscopy is based on an inelastic scattering process, which typically is much less probable than elastic scattering. For this reason, it is usually associated to weak signals, which also have to be enhanced similarly to IR absorption: the so-called

Surface Enhanced Raman Spectroscopy (SERS) [19].

In Raman scattering, the interaction between light and the molecule is mediated by the polarizability of the molecule. It can be demonstrated that only the vibrations causing a change in the polarizability of the molecule are available in Raman spectroscopy, indeed Raman intensity has a square dependence on the change in the polarizability:

$$I_{\mathrm{RAMAN}} \propto \left(\frac{\partial \alpha}{\partial Q}\right)^2 \tag{1.6}$$

where I_{RAMAN} is the Raman intensity, α is the polarizability of the molecule and Q the vibrational coordinate. On the other hand, as discussed, IR absorption intensity is proportional to the square of the change in the dipole moment of the molecule. Polar molecules have already a dipolar behavior, so their polarizability is small, for this reason they typically are Raman inactive, and IR active. Vice versa, in homonuclear molecules an external electric field can induce a strong dipole, making them appealing for Raman spectroscopy, and weak in IR activity. In general, symmetrical molecules and in-phase vibrations are usually studied by Raman spectroscopy, while asymmetrical and out-of-phase vibrations are usually investigated by IR spectroscopy. For these reasons, these techniques probe the same physical signals (molecular vibrations) but in a complementary way. In fig.1.3, a comparison between the energy exchange in IR absorption and Raman scattering is reported.

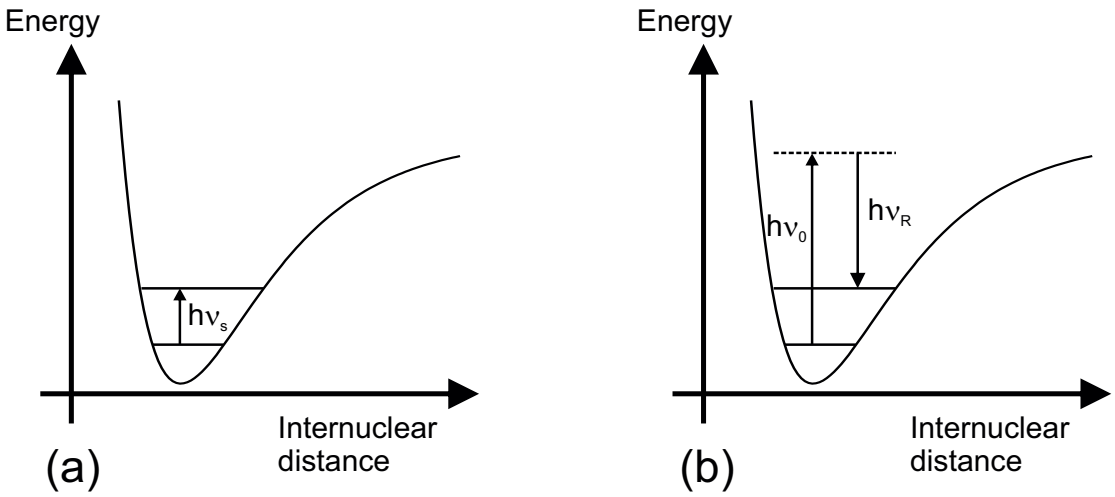

Figure 1.3: The energy exchange in IR absorption (a) and Raman scattering (b).

1.6 Surface-enhanced infrared absorption

The main point of this thesis is the design, realization and analysis of nanotechnologies employed in the detection of vibrational signals. Indeed, the coupling between IR light

and molecules is typically poor, due to the strong mismatch between the wavelength of the light and the dimension of molecules, around three orders of magnitudes (µm vs nm). This is where nanotechnology comes into play. Our aim is to employ nanostructured systems able to strongly affect the local behavior of the electromagnetic fields. These systems are based on the concept of optical resonances, resulting in electromagnetic hotspots, characterized by strongly confined and enhanced fields. The confinement reduces the spatial mismatch between light and molecules, while the enhancement increases the sensitivity to molecular signals.

Most of these efforts fall in the field of Surface Enhanced Infrared Absorption (SEIRA) approaches. The first demonstrations of SEIRA were given in the last decade of the XX century [20]. In the meantime, the knowledge on resonant nanoparticles, often called nanoantennas, was increasing thanks to the publication of seminal works. Soon, the scientific community realized the potential of nanoantennas in biosensing. Indeed, the tunable, confined and strong resonances supported by nanoantennas represent an ideal probe for vibrational signals [21]. This is the specific technology I will focus on.

The scope of these electromagnetic resonances is to enhance the detection of molecules. Indeed, they are sensitive to changes in the optical environment. The insertion of a small quantity of molecules produces two effects to the surrounding environment: a change in the refractive index and the introduction of absorption peaks. The electromagnetic resonances are sensitive to both effects. The first one usually produces a spectral shift of the resonance, proportional to the refractive index of the molecules. So, this kind of sensing does not probe absorption and it is not specific to the probed molecules, just to their refractive index. This type of sensing is typically called refractometric sensing.

On the other hand, the nanostructure resonances also couple with the vibrational lines of the molecules, enhancing their absorption. This enhancement makes their detection easier, representing the SEIRA signal. Since both effects are always present, often it is difficult to single out their contribution. The best approach in this case is to employ accurate optical simulations, from which one can separate the two effects and retrieve the real SEIRA signal.

The collected SEIRA signal is a scattering signal, coming from a complex phenomenon of interference between the molecular dipole and the dipolar resonance of the nanostructure, meaning that it does not probe the IR absorption directly. This is also the typical situation for tip-enhanced scattering techniques. However, in the next chapter we will discuss a novel tip-enhanced method, the photothermal induced resonance technique, which mechanically probes the IR absorption on the nanoscale.

1.7 Outline of the thesis

The aim of this introduction was to give context and clarify the aim of my research, reviewing also the general concepts representing the basis of the thesis. This thesis presents two main chapters, describing the two main activities I focused on during my PhD. Both chapters follow a stand-alone structure, stating the aim and the context of the work, describing the core of the activity and discussing the obtained results.

The first work is focused on the modelling of an experimental technique, named Photothermal Induced Resonance. My contribution to this work is mainly in theoretical modelling, through numerical simulations.

The second work aims at developing a platform of dielectric antennas working in the mid-infrared, thanks to the employment of an epsilon-near-zero material. In this case, I contributed to the design and the optimization of the platform, by means of numerical simulations, the fabrication process in a clean room environment, the characterization, both with experimental measurements and simulations, and a sensing experiment.

In the following sections of this introduction, I will discuss some key ingredients general to both works: the tools employed to model the nanostructures, plasmonic and dielectric optical resonances.

1.8 Tools employed in the modelling

1.8.1 Solving Maxwell's equations at the nanoscale

In order to study the electromagnetic environment at the nanoscale we need a proper tool to solve Maxwell's equations. Indeed, this step is crucial to describe and design nanostructured systems with a tailored electromagnetic response, which is our final aim. Moreover, Maxwell's equations can be analytically solved only for certain geometries, strongly symmetrical, but we need to be capable of solving them for any kind of geometry. In order to do this, we employ a numerical solution. The finite-difference time-domain (FDTD) method is one of the most used methods to solve numerically Maxwell's equations for any kind of geometry. It is especially exploited in the study of electromagnetic environments of small dimensions, down to the nanoscale. Being so widely employed, it benefits from a strong theoretical background.

The main idea behind the FDTD method was first proposed by K.Yee in 1966. The algorithm focuses on solving the curl equations:

$$\frac{\partial \mathbf{D}}{\partial t} = \nabla \times \mathbf{H}; \tag{1.7}$$

$$\mathbf{D} = \epsilon_0 \epsilon_\mathrm{r} \mathbf{E}; \tag{1.8}$$

$$\frac{\partial \mathbf{H}}{\partial t} = -\frac{1}{\mu_0} \nabla \times \mathbf{E}. \tag{1.9}$$

In these equations, $\mathbf{D}$ is the displacement field, $\mathbf{E}$ is the electric field and $\mathbf{H}$ is the magnetic field. ϵ_0 and μ_0 are respectively the vacuum permittivity and permeability, while ϵ_r is the relative permittivity. FDTD takes into account the modelling of dispersive materials (i.e. materials showing a permittivity dependent on the frequency), but it is valid only for non-magnetic media (at optical frequencies, this is typically the case). The aim of FDTD is to discretize the spatial and temporal dimensions [22]. It arranges space in a three-dimensional orthogonal grid: in fig.1.4 the Yee cell, the unit cell of the

discretization, is reported. The unit cell is a cube having Δx, Δy, Δz as edges, in the x, y, z direction, respectively. In the end, the simulation environment is divided in a cartesian mesh, where every point is identified by the coordinates $(x, y, z)_{i,j,k} = (i\Delta x, j\Delta y, k\Delta z)$, where i, j, k are integers.

In this picture, the electric fields are calculated along the edges of the cube, while the magnetic fields are computed on the vectors normal to the faces of the cube, or vice versa, depending on the polarization of the light. Every point of the grid is associated to an appropriate value of the permittivity modelling the medium, which carries the information needed to simulate the optical interaction between the medium and light. In order to solve the curl equations, the temporal evolution of the fields is also needed. Thus, an interval Δt is defined as the unit of the temporal discretization and time t can be written as sum of Δt, $t = n\Delta t$, where n is an integer number. In the end, a field $f(x, y, z, t)$, at a given point in space and time, will be written as:

$$f(x, y, z, t) = f(i\Delta x, j\Delta y, k\Delta z, n\Delta t) = f^n_{i,j,k}. \tag{1.10}$$

By expressing the electric and magnetic fields in this form, Maxwell's curl equations can be solved at every node of the Yee grid, granted that the values of the fields at time $t = 0$ are known. At the end, we obtain a full expression of the fields at every point of the Yee grid, as the result of the numerical approximation of the solution of Maxwell's curl equations. This description is valid for the originary formulation of the FDTD method, however nowadays commercial software use more complex alogorithms. The main improvement of these approaches is the possibility to employ a non-uniform mesh, with higher accuracy where field gradients are expected to be stronger. In our works, we employ this kind of commercial software [23]. The boundary conditions are of key importance in properly modelling the optical environment. In particular, we will exploit the Perfectly Matched Layer (PML) and the periodic boundary conditions. The PML boundary conditions impose an absorbing layer at the selected boundary. This layer matches the optical impedence of the surrounding material, in order to avoid spurious reflections. PMLs are typically employed when one wants to extend indefinetely a material, e.g. when modelling a substrate or the free space.

Periodic boundary conditions replicate the simulation environment in an infinite array. They do this just in their dimension of competence, meaning that one could have an infinite array in one dimension and PML boundary conditions in another one. This kind of boundary condition is usally employed when a periodic array of nanostructures has to be modelled, e.g. an infinite array of nanoantennas.

As discussed, the FDTD method solves Maxwell's equations in the time domain. However, some results, such as the transmission of an object, are more easily analyzed in the frequency domain. The passage from one domain to the other is performed by employing Fourier transformations.

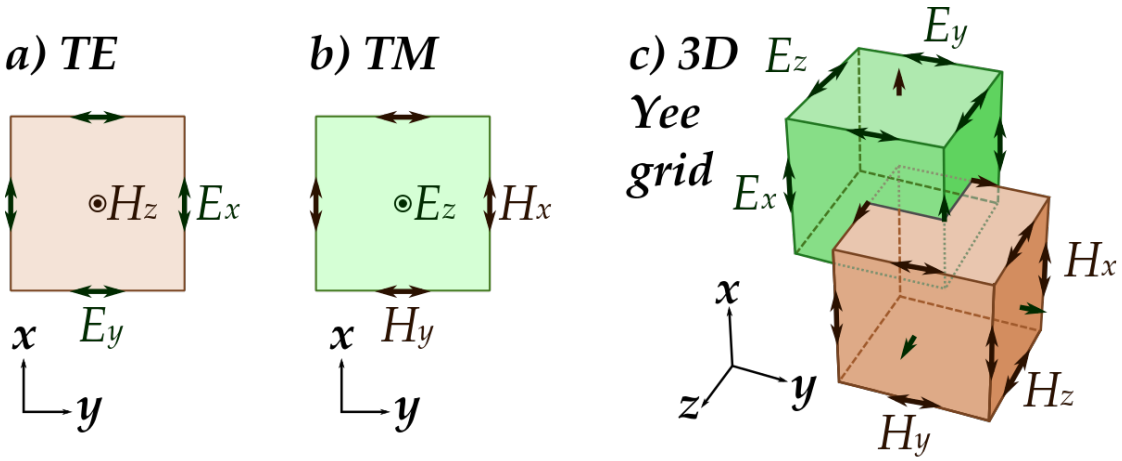

Figure 1.4: Representation of the cartesian Yee grid used to discretize the optical environment in FDTD.

1.8.2 Heat conduction at the nanoscale

The development and establishment of technologies working at the nanoscale has raised a strong interest in proper modelling the heat transfer at such a small scale. Indeed, at this scale, thermal dynamics have to be compared with other phenomena into play, since the characteristic heat diffusion time scales with the square of the thickness of the sample. Moreover, the small scale highlights the interfacial effects, which can overcome the bulk contribution. In addition, in the present work, we employ systems properly tailored to sustain strong and localized electromagnetic fields, which, because of the optical absorption, act as a thermal source. This means that the thermal sources we use have a strongly confined distribution, which requires an accurate treatment. All these effects show the non-trivial nature of thermal modelling of the systems we are considering. In particular, we will analyze these effects in detail in chapter 2, which is focused on modelling an experimental technique probing thermal effects on the nanoscale.

Let us discuss the thermalization dynamics with a simple model. Starting from Fourier's law, we have:

$$\Phi = -\eta \nabla T \tag{1.11}$$

where Φ is the heat flux, meaning the heat energy passing through a surface of 1 m^2 in 1 s, η is the thermal conductivity of the medium and ∇T the gradient of temperature causing the flow of energy. By combining it with the heat transport equation:

$$\rho c_p \frac{\partial T}{\partial t} = -\nabla \cdot \Phi \tag{1.12}$$

where ρ is the density of the medium, c_p its specific heat, we obtain:

$$\rho c_{\mathrm{p}} \frac{\partial T}{\partial t} = \eta \nabla^2 T. \tag{1.13}$$

Now, we can define the parameter $a = \frac{\eta}{\rho c_p}$, which is the so-called thermal diffusivity. The same equation can then be re-written as:

$$\nabla^2 T = \frac{1}{a}\frac{\partial T}{\partial t}. \tag{1.14}$$

In order to understand the thermalization dynamics, in relation with the spatial scale, we need a thermal source, the simplest one being a point in space and time. The equation becomes:

$$\nabla^2 T - \frac{1}{a}\frac{\partial T}{\partial t} = S\delta(t)\delta(\mathbf{r}). \tag{1.15}$$

where S represents the amplitude of the heat pulse. The temperature distribution coming from the differential equation is:

$$T(\mathbf{r}, t) = \frac{S}{(4\pi r t)^{\frac{3}{2}}} e^{-\frac{r^2}{4at}}. \tag{1.16}$$

This expression represents a gaussian profile of temperature expanding isotropically with a characteristic width $w = 2\sqrt{at}$ after a time t. So, the time needed by this heat pulse to diffuse over a sphere of radius R will be on the order of $t_d = \frac{R^2}{a}$. Here, we can appreciate the square dependence of the diffiusion time on the distance. This is crucial in the investigation of the characteristic scales for heat diffusion. Indeed, taking a reasonable value for $a = 10^{-6}$ $m^2\,s^{-1}$ and a radius of 1 nm, we obtain a time $t_d = 1$ ps. This value is on the same order of magnitude of the average phonon relaxation time, meaning that the equations cited above have to be adjusted. Indeed, Fourier's law, as written in eq.1.11, states that a difference in temperature causes an istantaneous heat flux. This approximation could lose its validity in a nanoscale setting. Thus, Fourier's law is adjusted by considering the mean phonon relaxation time τ:

$$\tau\frac{\partial \Phi}{\partial t} + \Phi = -\eta\nabla T. \tag{1.17}$$

When τ is small with respect to the characteristic time t_d of the system, the term $\tau\frac{\partial \Phi}{\partial t}$ becomes negligible and the macroscopic laws are still valid. In our case, the smallest geometries we will analyze have a characteristic length of 10 nm, associated to a t_d on the order of 100 ps, still much larger than τ.

For this reason, in our analysis, the equation of heat transport will take the form:

$$\rho c_p\frac{\partial T}{\partial t} - \eta(\nabla^2 T) = Q, \tag{1.18}$$

where Q is a source of thermal energy per unit volume. In order to solve this equation numerically, we will use a commercial solver (referred to as HEAT) coupled to the software used to solve optical simulations [24]. The source term Q is represented by the optical absorption of the sample obtained in the optical simulations. This means that after performing optical simulations, in FDTD, and collecting the optical power absorbed by the system, this power is transferred to HEAT and used as the heat source for the

thermal simulations. The parameters required to perform the thermal simulations are the density, the specific heat and the thermal conductivity of all materials involved: these are properties easily determined experimentally and found in literature. If the system has enough time to thermalize in the considered timescale, we are considering a steady-state situation. This is expressed by eliminating the transient term from the equation: $\frac{\partial T}{\partial t} = 0$. A steady-state simulation models a thermal environment which has enough time to reach equilibrium and provides the spatial temperature distribution at equilibrium. On the other hand, a transient simulation provides also the temporal evolution of the thermal environment. In the end, we will obtain the temporal and spatial distribution of the temperature, provided properly defined initial and boundary conditions.

The boundary conditions are of key importance in thermal modelling. HEAT only solves the thermal transport equation in solid-state media, while the fluids are modelled as boundary conditions. So, in our simulations the terms of convection and radiation will be described as boundary conditions imposed at the interfaces between the solid media and air. However, at our scale, these two terms usually have a negligible contribution. The other boundary conditions offered by the software are of fixed temperature at an interface, or fixed power passing through an interface. The boundary condition that we will use the most in our modelling is the fixed temperature at a certain interface, which models the confined nature of the heating phenomena we will consider. Indeed, we must not forget that the nanostructured systems we are studying are supported by much bigger objects (i.e., a substrate or the cantilever) which usually are not affected by physical phenomena at the nanoscale. For this reason, in a thermal charaterization, these bodies will be unperturbed and effectively act as heat sinks.

HEAT models the simulation environment through the fine-element method (FEM). The working principle of FEM is the division of the environment in smaller domains, which are the so-called elements. The elements form a mesh approximating the simulated geometry and every node of the mesh is associated with a proper set of material properties. In FEM, the mesh is not required to be cartesian, like in FDTD. A characteristic representation of an FEM mesh is reported in fig.1.5. The domains are smaller in areas where the temperature gradients are expected to be higher, in order to increase the accuracy of the approximation in those zones. Each domain is associated with a set of equations and the entirety of these sets form a universal system of equations modelling the original problem. In this way, a complex problem is broken down in smaller and easier equations, which are solved numerically. The main advantages of employing FEM are:

- The employment of a polygonal meshing allows for an accurate representation of complex geomteries, especially curved surfaces, which are difficult to approximate with a cartesian grid like the Yee grid.
- The possibility to design an environment with heterogenous material properties.
- Good precision in modelling the local effects, thanks to a dense mesh in areas characterized by non-uniform temperature distributions.

The last two advantages here reported are shared also by non-uniform FDTD meshing methods.

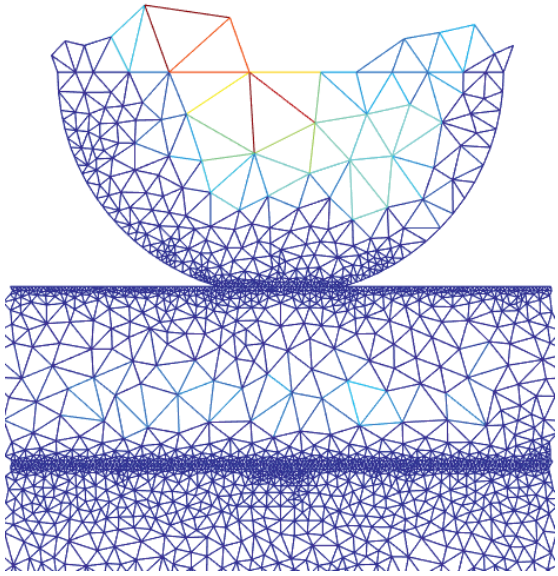

Figure 1.5: Representative partition of a thermal environment with a FEM mesh.

1.9 Light scattering and nanoantennas

1.9.1 Mie resonances

When light encounters an obstacle on its path, i.e., a discontinuity in the medium in which the radiation is travelling, many phenomena can occur. One of them is the deviation of the light rays from their original path. This phenomenon is generally referred to as scattering. Since it originates from the heterogeneity of the media, the physical cause of scattering has to be found in the composition of matter, and its interaction with light.

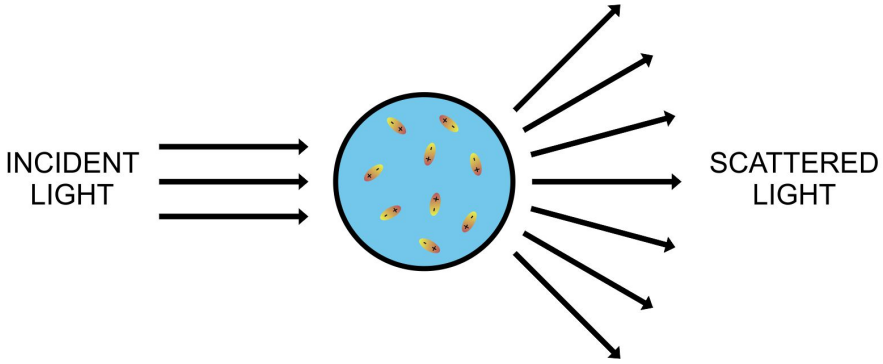

Figure 1.6: Pictorial depiction of the physical origin of light scattering.

In this context, we can imagine a plane wave hitting a portion of matter, described as an aggregate of molecules, which can be treated on an optical level as discrete electric charges (as depicted in fig. 1.6). The oscillating electromagnetic fields carried by the light interact with these charges and force them to oscillate at the same frequency. This secondary radiation is what we call scattered light [25–27]. Charge oscillations induce local field enhcancement, which we also want to optimize in the design of nanostructures. For this reason, scattering and local field enhancement are closely related in these nanostructures. Light scattering is a ubiquitous phenomenon. In fact, most media are optically dense, meaning that the wavelength of the light (400-700 nm for visible, even higher for IR) is larger than the distance between two molecules, representing the optical obstacle responsible for scattering (in gases, the least dense media, this separation is around tens of Å, in standard conditions). So, when light travels in a medium it constantly encounters optical discontinuities. Moreover, since the scattered light is re-emitted at the same wavelength of the incident one, it also affects many of the surrounding molecules. Indeed, by considering the total response of the molecular assembly, it is possible to explain optical phenomena as diffusion, diffraction, reflection and refraction, which are a consequence of scattering, ultimately.

From all these considerations, we can see how scattering plays a crucial role in light-matter interaction. In particular, it is interesting to study how scattering can be used for optical control and enhancement, that is, study how to optimize the scattering from an engineered particle. In the end, such a particle can work as a basic constituent of photonic technologies.

An analytical solution to the problem of scattering from a single particle has been proposed by Gustav Mie in 1908 [28]. The solution is valid under the condition of spherical symmetry and is written as an infinite series of spherical multipolar harmonics. The pertinence of the Mie solution is irrespective of the size of the particle: it converges to the Rayleigh scattering in the small particle regime and to geometric optics in the large particle regime. In particular, Mie theory predicts the establishment of optical resonances in properly tuned nanoparticles. They are the so-called Mie resonances. These resonances mainly depend on the size of the particle and its refractive index. At

optical frequencies, the typical size of a resonant nanoparticle interests the range between hundreds of nm and a few µm.

These resonances are generally observed in particles made of high permittivity (ϵ) media, both dielectric and metallic. The main difference between the two is the sign of the permittivity, which is negative for metals and positive for dielectrics. For metals, these resonances are interpreted as localized surface plasmon resonances (LSPRs), which have been extensively exploited for optical control at the nanoscale in the last two decades, establishing their own field of study: plasmonics. However, scattering cross-sections showing multipolar resonances have been demonstrated also in dielectric particles, typically made of high index seminconductors. Indeed, dielectric particles also show magnetic resonances, which are typically hindered by the screening effect of metals in plasmonic scatterers [29]. Magnetic resonances are essential for a specific set of applications, e.g. to loacally enhance molecular chiral signals, which is done by tailoring the interaction between the electric and magnetic resonances of the nanoparticle [30]. This will be explained in more detail in the last section of this chapter.

In the multipolar description, we can express the scattered electric field as:

$$\begin{aligned}&\mathbf{E}_{\text{sca}} = \mathbf{E}_{\text{ED}} + \mathbf{E}_{\text{MD}} + \mathbf{E}_{\text{EQ}} + ... = \\ =&\frac{k^2}{(4\pi\epsilon_0)}\frac{e^{ikr}}{r}[(\mathbf{u}\times\mathbf{p})\times\mathbf{u}] - \frac{1}{c}(\mathbf{u}\times\mathbf{m}) - \frac{ik}{6}[(\mathbf{u}\times\mathbf{Q})\times\mathbf{u}] + ...\end{aligned} \tag{1.19}$$

where k is the wavevector of the light, r the radius of the spherical particle, ϵ_0 the vacuum permittivity, $\mathbf{u}$ the unit vector along the propagation of light and $\mathbf{p}$, $\mathbf{m}$ and $\mathbf{Q}$ the momenta associated to each multipolar contributions [respectively, electric (ED) and magnetic (MD) dipole, electric quadrupole (EQ)].

The scattering cross section of such a particle will show resonant peaks. The most interesting resonances for us are the the electric dipole and the magnetic dipole resonance.

In the end, the ratio $2rn/\lambda$, where n is the refractive index of the particle, will dictate the spectral position of each resonance [31]. In particular, as n increases, the particle sustains a better scattering efficiency. Even if this analysis was originally carried out for a spherical geometry, its validity can be qualitatively extended to all kind of shapes. In this case, it is important to define a characteristic dimension of the particle, which replaces the sphere radius in the comparison with the wavelength of the incident light. However, in this case an analytical solution cannot be found, and numerical methods have to be employed.

Indeed, we can design a dielectric particle showing Mie resonances in the infrared. We consider a pillar with radius $r = 3$ µm, height $h = 1.6$ µm, made of a lossless material with a refractive index $n = 3.5$ in vacuum. Looking at the IR scattering spectrum of this particle (fig. 1.7), we can see several peaks, around 10, 12 and 16 µm. In fig. 1.8 the vectorial representation of the electric field is reported for the three resonances. From this picture, we can notice that the resonance at lower energies corresponds to the electric dipole resonance, followed by the magnetic dipole resonance (the one in the middle), while at higher energies we find the electric quadrupole resonance.

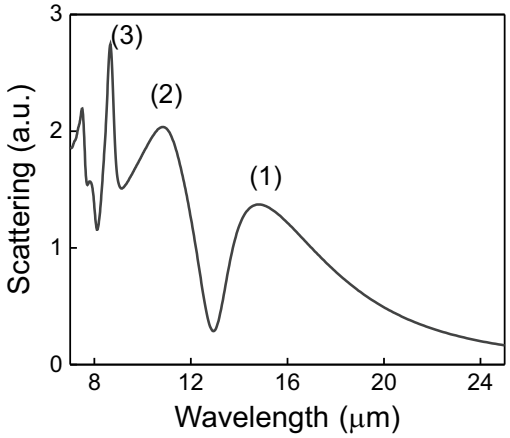

Figure 1.7: The scattering spectrum of a cylindrical dielectric antenna with $r = 3$ µm, $h = 1.6$ µm and $n = 3.5$ in vacuum. The peaks in the spectrum represent: (1) the electric dipole, (2) the magnetic dipole and (3) the electric quadrupole resonances.

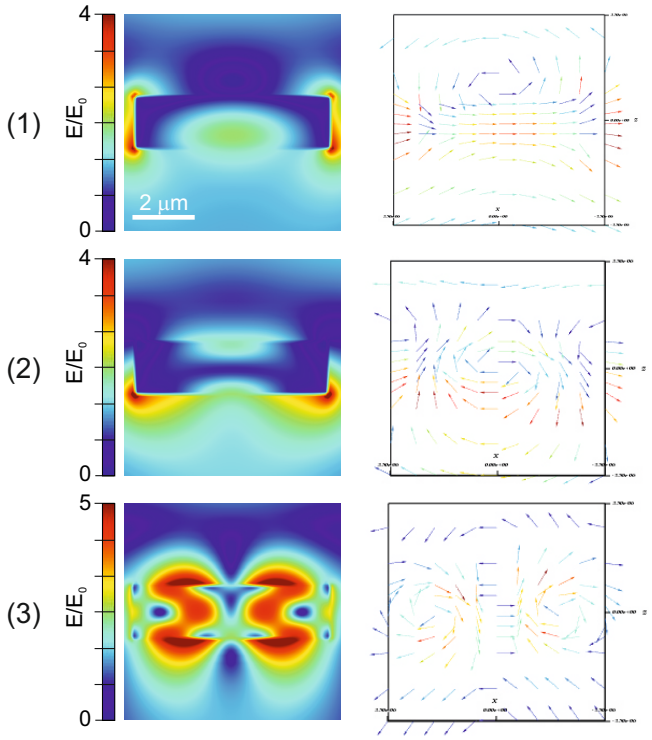

Figure 1.8: On the left, the intensity, on the right the vectorial representation of the electric field at the (1), (2) and (3) resonance conditions. From these maps, we can see that (1) corresponds to the electric dipole resonance of the particle, (2) the magnetic dipole resonance and (3) the magnetic quadrupole resonance.

In general, plasmonic and dielectric resonances share common qualities:

- High-field enhancement close to the particle.
- Resonant behavior in the polarizability of the particle, enhancing its scattering and absorption.
- Strong tunability: by changing the aspect ratio of the particle, we can control the spectral position of the resonances.

The capability of these particles to couple free-space radiation to strong near-fields mimics the behavior of radio-frequencies antennas. Moreover, exploiting state-of-the-art fabrication processes, it is possible to fabricate particles with a refractive index and characteristic dimensions which grant resonances in the visible and infrared range (from hundreds of nanometers to tens of micrometers). In the end, these particles will act as antennas working at optical frequencies, which are often referred to as nanoantennas for their typical size (on the scale of hundreds of nanometers to micrometers).

1.9.2 Plasmonic resonances

The Drude model illustrates the optical properties of a material which can be described as a gas of free electrons moving in a fixed lattice of positive and larger charges, the ion cores. The interaction between stationary positive and free negative charges creates peculiar phenomena, which characterize the optical response of the material. Indeed, upon excitation by an electromagnetic field, the electron cloud moves. However, when displaced, the electrons feel the Coulomb interaction with the positive nuclei. In this way, a collective oscillatory motion of the negative charges is established. This simple model, in order to be accurate, requires that matter waves can propagate freely in the ion lattice and electron-electron scattering is inefficient [32]. These two requirements are satisfied in certain media, such as metals or heavily-doped semiconductors in the IR.

The Drude model describes the permittivity of these materials as:

$$\epsilon(\omega) = \epsilon_\infty - \frac{\omega_p^2}{\omega^2 + i\gamma\omega}, \tag{1.20}$$

where ϵ_∞ is the response of the material at high frequencies (which is constant), ω_p is the plasma frequency of the medium, ω is the frequency and γ represents the losses due to electron collisions. The plasma frequency is expressed as $\omega_p = \sqrt{\frac{ne^2}{m^*\epsilon_0}}$, where n is the density of free electrons, e is the electron charge, m^* its effective mass and ϵ_0 the vacuum permittivity. $\epsilon(\omega)$ can be decomposed in two terms, a real and an imaginary part:

$$\epsilon(\omega) = \epsilon'(\omega) + \epsilon''(\omega) = \epsilon_\infty - \frac{\omega_p^2}{\omega^2 - \gamma^2} + \frac{i\gamma\omega_p^2}{\omega(\omega^2 - \gamma^2)}. \tag{1.21}$$

The imaginary part describes the losses inside the material, while the real part represents the material proneness to be polarized. Following this model, there are values

of ω for which $\epsilon'(\omega)$ is negative (i.e., at low frequencies). In this regime, interesting optical phenomena occur. Indeed, at the interface between a material with $\epsilon'_{\mathrm{m}}(\omega) < 0$ and a lossless dielectric medium, with $\epsilon_{\mathrm{d}}(\omega) > 0$, collective surface oscillations of the free electrons can be excited. These oscillations require the configuration just described [$\epsilon'_{\mathrm{m}}(\omega) < 0$ and $\epsilon_{\mathrm{d}}(\omega) > 0$], meaning that it is a prerogative of the plasmonic-dielectric interfacial interaction. Charge oscillations propagate along the interface carrying out an electromagnetic wave, which is confined in the direction perpendicular to the interface, both in the dielectric and plasmonic media (fig.1.9). The electron oscillations and the associated electromagnetic waves represent the so-called surface plasmon polaritons (SPPs). The exponential decay of SPPs enables a sub-diffraction confinement in the direction perpendicular to the metal-dielectric interface. This property has great appeal in nano-optics, the branch of physics studying light control at the nanoscale, and in this context, a dedicated field of study, known as plasmonics, has gained more and more interest over the years. In particular, in the last two decades, plasmonics has been widely employed in nano-optical applications [33, 34]. Indeed, starting from the simple metal-dielectric interface, SPPs can be engineered in more complex technologies, such as metal-insulator-metal (or insulator-metal-insulator) structures, leading e.g. to sub-diffraction plasmonic waveguides [35, 36].

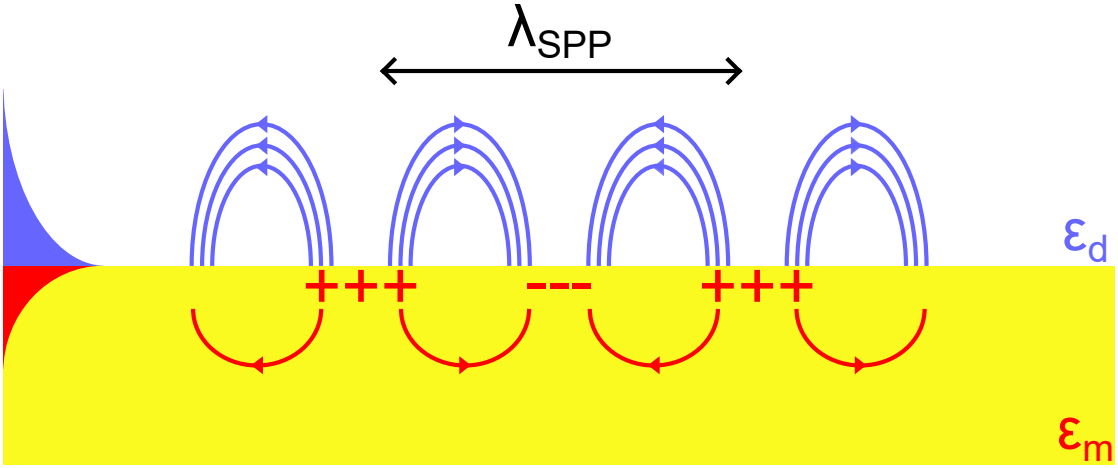

Figure 1.9: Surface plasmon polariton propagating along the interface between a metal (with a permittivity ϵ_{m}) and a dielectric (with a permittivity ϵ_{d}). In the direction perpendicular to the interface, the SPP shows an exponential decay, depicted on the left part of the image.

Another application of plasmonics is the establishment of optical resonances in sub-wavelength particles, often referred to as plasmonic nanoantennas [37]. The broad field of nanoantennas (both plasmonic and dielectric) will be the main focus of chapter 3, however the general physical properties of plasmonic nanoresonators will be discussed here, since these concepts are often used through the whole thesis. In the case of plasmonic nanoparticles, the electron oscillations are confined within a volume characterized

by a sub-wavelength dimension (while in SPPs, they are free to move along the metal-dielectric interface). For this reason, these resonances are localized and not propagating like the SPPs, so they are called Localized Surface Plasmon Resonances (LSPRs). Let us derive the expression of an LSPR for a spherical nanoparticle. Being much smaller than the excitation wavelength, the particle can be considered to be immersed in a homogenous field. In this situation, the response of the particle is uniform, showing no retardation effects, and the phase of the field is fixed. This approach is referred to as quasi-static approximation. The simplest geometry to analyze LSPRs is a sphere. In this case, we can write an analytic expression of the particle response, described by the induced dipole moment:

$$\mu_{\mathrm{d}} = 4\pi r^3 \epsilon_0 \frac{\epsilon_{\mathrm{m}} - \epsilon_{\mathrm{d}}}{\epsilon_{\mathrm{m}} + 2\epsilon_{\mathrm{d}}} E_0, \tag{1.22}$$

where E_0 is the amplitude of the incident field, ϵ_{m} the permittivity of the metallic particle, ϵ_{d} the permittivity of the surrounding environment. As discussed, ϵ_{m} has a real and imaginary part ($\epsilon_{\mathrm{m}}=\epsilon'_{\mathrm{m}}+\epsilon''_{\mathrm{m}}$): the resonance condition is met around the value when the real part of the denominator in eq.1.22 goes to zero, giving a high value of the dipole moment. At resonance, the near-field intensity and the scattering are greatly increased. If we consider the metal objecte immersed in air, $\epsilon_{\mathrm{d}} = 1$, the resonant condition is reached when $\epsilon'_{\mathrm{m}} = -2$. Again, as said for SPPs, a material with negative permittivity is needed to reach this condition (e.g. Au, Ag in the visible) [38].

At resonance, the sphere has a dipolar behavior, meaning that at the sides of the particle there will be excess charge distributions of opposite sign, which act like two-point like charges in an electric dipole. In eq.1.22, we can see that the resonance condition is strongly dependent on ϵ_{d}, representing the environment surrounding the particle. This is the basic principle of sensing with LSPRs: if ϵ_{d} slightly changes, meaning that there is a small perturbation in the environment, such as a small number of molecules, the resonant condition shifts. From eq.1.22 we can appreciate that the resonance condition is irrespective of the particle's geometry, it only depends on the permittivity of the material. This is because we are considering a geometry with spherical symmetry and a quasistatic condition. If we break the symmetry, and consider a prolate ellipsoid, we obtain a dipole moment of the form:

$$\mu_{\mathrm{d}} = V \frac{\epsilon_{\mathrm{m}} - \epsilon_d}{P_j \epsilon_{\mathrm{m}} + (1 - P_j)\epsilon_{\mathrm{d}}} E_0, \tag{1.23}$$

where V is the volume of the particle. In this expression, the denominator is a function of P_j, which depends on the aspect ratio, the ratio between the two axes of the particle [37]. This represents a more realistic situation and highlights a further degree of freedom: the tunability of LSPRs through the geometry of the particle. In other words, by changing the aspect ratio we can move the spectral position of the resonance. In fig.1.10 a comparison between a sphere and an ellipsoid of Au is reported. We can appreciate that the resonance shifts when the aspect ratio of the particle is modified, by comparing the scattering spectra in panels a and b. This approach is qualitatively valid for other kinds of shapes, for which an analytical expression is not available. For this reason, the

resonance in less regular shapes are designed and investigated through numerical methods: in our case, we employ a commercial FDTD software solution [23]. Plasmonics will be exploited in the following work. The key concept we have to keep in mind is the ability of plasmonic resonances to confine the light in sub-wavelength hotspots: their employment strongly modifies light-matter interaction at the nanoscale.

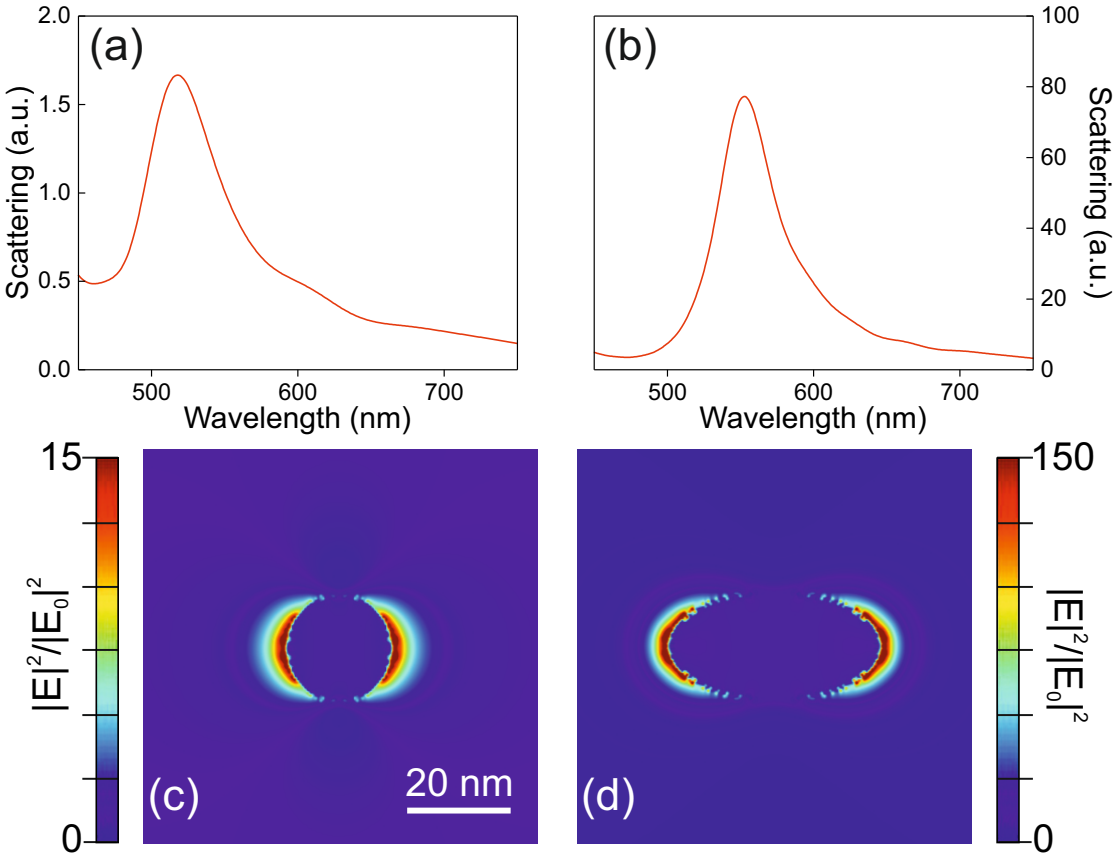

Figure 1.10: In (a), the simulated scattering spectrum of a Au sphere of radius $r = 10$ nm. In (b) the simulated scattering spectrum of a Au ellispoid of radii $r_1 = 10$ nm, $r_2 = 20$ nm, $r_3 = 10$ nm. In (c) and (d), the field distribution at resonance for the sphere and the ellipsoid, respectively.

Chapter 2

Modelling a PTIR experiment

Abstract Photothermal induced resonance (PTIR) is a novel and promising technique able to determine the chemical composition of a surface with nanoscale resolution, by combining an IR light, illuminating the sample, with an atomic force microscope (AFM) tip, measuring its local thermal expansion. Being a recently developed technique, it does not benefit from a strong, common theoretical background. This work aims at developing a solid theoretical model of a PTIR experiment. This analysis starts from two PTIR datasets, obtained by employing two different AFM probes: a standard pyramidal Au-coated silicon tip and a triangular Pd antenna sustained by a silicon nitride (Si_3N_4) cantilever. The latter is specifically designed to have a strong optical confinement (exploiting the antenna resonance), more sensitive to superficial effects and thus particularly suitable for PTIR. The experimental data study the dependence of the PTIR signal on the thickness of a whisker of PMMA, between 10 and 400 nm. The experimental data show two different behaviors associated with the two AFM probes, a consequence of the diverse optical confinement: the signal is linear for the Au probe and sublinear for the Pd one. Both behaviors are not explained by the PTIR models found in literature, which would predict a quadratic dependence for both tips.

We propose a detailed theoretical model highlighting the crucial parameters responsible for this deviation, by employing commercial software for optical and thermal simulations. In particular, we focus on three physical effects: the optical confinement coming from the AFM probes, the insulation caused by interfacial thermal resistances (ITRs) and the thermalization dynamics. The first two effects contribute to creating a tight distribution of temperature increase inside the PMMA whisker, while the latter takes into account the slow thermal dynamics of high-thickness samples, important in determining the weight of the heating and cooling processes in the PTIR signal. These effects contribute differently to the PTIR signal based on the sample thickness. In the end, the dependence of the signal on the thickness is modified for both AFM probes: the Au tip shows a roughly linear trend, whereas the Pd tip presents a sublinear behavior. These results are in good agreement with the experimental ones.

In conclusion, in this work we present a solid and complete model of a PTIR measurement. The key parts of the model are not only relevant to this specific work, but also

to characterize any kind of PTIR experiment. Indeed, the role of ITRs is crucial in the quantitative determination of the temperature increase or its distribution in the sample. For instance, this model has been applied in a work in collaboration with the Sapienza University of Rome, to characterize the conformal changes in a photosensitive protein due to illumination. In this case, a reasonable estimate of the temperature increase is crucial, so the employment of ITR is needed.

The experiments presented in this chapter were carried at the Sapienza University of Rome, the fabrication of the Pd tip was done at Kelvin Nanotechnology in Glasgow, the design of the Pd tip and all the simulations were performed at Politecnico di Milano. In particular, my personal contribution concerns the theoretical modelling and the related analysis of the experimental data.

2.1 Introduction to PTIR

2.1.1 The PTIR technique

The photothermal induced resonance technique (PTIR) is a nanospectroscopic technique combining the information coming from infrared spectroscopy and the nanoscale resolution of an AFM scanning measurement [39, 40]. In this technique, an infrared light is shined upon the sample, which absorbs it. The optical absorption causes the heating of the sample, which is relaxed by thermal expansion. In the end, this expansion is felt by an atmoic force microscopy (AFM) tip operated in contact-mode. By spanning the illumination wavelength, a spectrum can be produced. Indeed, the optical absorption becomes resonant when the light targets a vibrational absorption line characterizing the superficial chemical composition of the sample. So, the wavelengths associated to higher optical absorption label the molecular vibrations which define the chemical fingerprint of the sample. On the other hand, by scanning the AFM tip, the sample topography can be studied. Combining the two ingredients, we obtain a superficial map with spectral information in the IR: this information characterizes chemically the sample surface with a nanometric resolution.

In fig.2.1 a typical set-up for PTIR is sketched. We can see the source of the illumination on the left, represented by the laser. The light can be shined in continuous or pulsed regime. In the continuous regime the sample has the time to fully thermalize, so the PTIR measurement probes its steady-state thermal response. This is also true for long pulses (i.e. 1 µs, for samples with a thickness up to hundreds of nanometers). On the other hand, in a pulsed regime there is the possibility to couple the repetition rate of the laser with a bending mode of the AFM cantilever: this magnifies the PTIR signal by the quality-factor of the cantilever resonance. This is the configuration used in our experiment, thus it will be explained in detail in a dedicated paragraph.

The PTIR resolution is ideally limited by the AFM resolution. However, since in a PTIR measurment the AFM tip probes the thermal expansion of the sample, another point has to be considered. Indeed, the thermal expansion depends on the material properties and the field distribution in the sample. These ingredients contribute in defining the surface sensitivity of a PTIR measurement. A steep change in the temperature would be more easily detected by the AFM tip, since it would mean a stronger contrast with the surrounding areas of the sample. We cannot tailor the material properties, which in our experiment are uniform, since we are considering a homogeneous sample. However, we can tailor the field distribution inside the material. This is done by employing plasmonic resonances, which are able to create intense electromagnetic hotspots at the nanoscale. In the end, the optical absorption shows a strongly confined profile, increasing the sensitivity of the AFM detection.

To complete the set-up, we find an AFM tip scanning the sample, while a laser coupled with a photodiode measures the deflection of the cantilever, which represents the PTIR signal.

PTIR is employed in a rich range of applications. Indeed, in the last years, PTIR has been employed in the nanoscale analysis of polymeric films [41, 42], in biological

studies [43], e.g. subcellular imagining [44] or the study of protein photocycles [3], or in the characterization of nanostructured systems [45–47], for example, to image the field distribution of an integrated waveguide mode [48]. To summarize, PTIR is a versatile technique, which gathers crucial information in the MIR, thus especially interesting for biologic and IR-working technologies, by enhancing and then probing the optical absorption of a film in the fingerprint region.

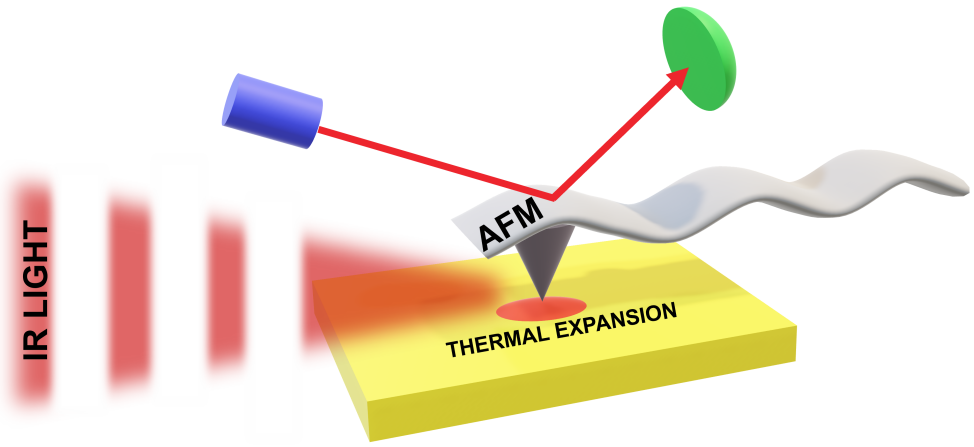

Figure 2.1: Sketch of a typical PTIR set-up.

2.1.2 Comparison with similar techniques

PTIR operates in a range of applications which are already covered by other tip-enhanced techniques, the most important ones being scattering-type scanning near field optical microscopy (s-SNOM) and tip-enhanced Raman spectroscopy (TERS). Both techniques enable spectroscopical analysis at the nanoscale and imaging with a sub-wavelength resolution, however there are fundamental differences with PTIR.

The major discrepancy stands in the physical phenomenon probed by the different techniques. Indeed, PTIR investigates directly the absorption of the excitation light, by probing the thermal expansion of the sample, while s-SNOM and TERS study the light scattered by the sample [40]. In particular, s-SNOM investigates elastic scattering (meaning that wavelength of the scattered light is the same of the excitation light) [49], while TERS probes Raman frequency shifts in the scattered light, which requires an inelastic process [50]. For this reason, the performances of s-SNOM and especially TERS benefit from samples with good scattering efficiencies. This requirement does not hold in the case of PTIR, which just needs a sample absorbing in the MIR. As discussed in the introduction, this represents a very common situation, since all materials

have vibrational resonances in the infrared. Moreover, both s-SNOM and TERS, being scattering-detecting techniques, typically interest surface effects, while PTIR is related to the thermal expansion of the sample, and can investigate deeper parts of the sample. In the case of TERS, the scattering efficiency is also increased by employing AFM tips specifically designed for the technique. This represents a technological drawback of TERS, since the specific tips are the product of complex and difficult to reproduce fabrication processes. On the other hand, PTIR has been widely demonstrated with commercial AFM probes. Regarding s-SNOM, the detected signal has to be discussed. Indeed, probing the scattering instead has some disadvantages. First of all, the signal is more complex to interpret and in order to understand it, the whole optical response of the system (the AFM tip, the sample and the substrate) is needed (this is done with a separate characterization). Moreover, the scattering is affected by morphological changes in the sample, or even the substrate, while the absorption probes directly the chemical composition of the sample.

To conclude, PTIR provides a significant and direct measurement of the absorption spectrum of the sample. The tip enhancement increases the sensitivity of the technique, which does not need complex and dedicated optical set-ups to detect a meaningful signal. Moreover, absorption detection gives an output signal relatively easy to understand compared to scattering.

2.2 The experimental set-up

2.2.1 Description of the AFM probes

In this study, two different AFM probes are employed. The first is a gold-coated pyramidal silicon tip supported by a silicon cantilever. The geometrical modelling, as well as the SEM image of this tip, is presented in fig.2.2. This is a standard tip, typically employed in AFM-based optical measurements [51–53]. This tip is not resonant and its main optical contribution is the establishment of a lightning rod effect to confine and enhance the absorption of the sample and consequently the PTIR signal. Moreover, the gold coating allows one to exploit plasmonic effects if the sample under study is designed properly. In fact, when possible, it is convenient to fabricate the sample over a layer of Au, so that, when the Au-coated tip is scanning the sample, a plasmonic nanocavity is created between the Au apex of the AFM probe and the Au substrate sustaining the sample. The effect of this plasmonic nanocavity is to further improve and confine the electric field enhancement in the sample, consequently localizing its optical absorption. In the end, this configuration increases the signal of the PTIR technique, allowing for measurement requiring high sensitivity, like the detection of single protein patches, and high resolution, confining the optical absorption in a sub-wavelength spot [3]. In the simulations, we model this tip as an infinite Si truncated cone with an opening angle of approximately 20° and a golden semispherical apex of radius $r = 50$ nm. The Si truncated cone is covered by 25-nm-thick gold coating.

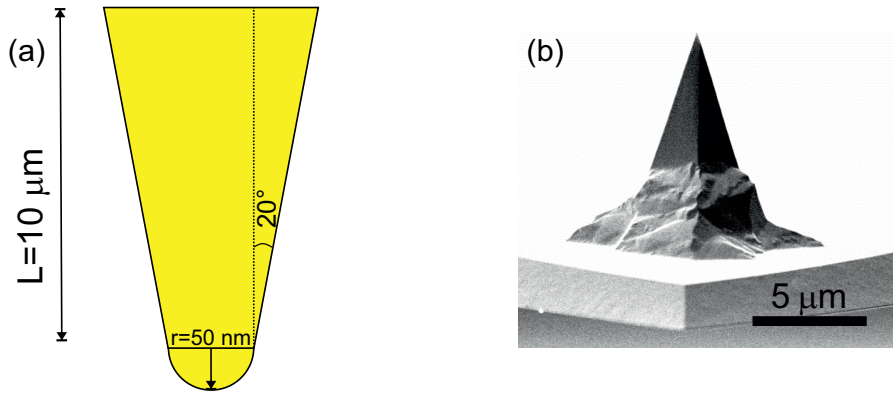

Figure 2.2: In panel a, a sketch of the Au tip with the geometrical parameters used in the modelling. In panel b, a SEM image of the tip.

The second probe is represented by the 200-nm-thick triangular-shaped tilted extremity of a silicon nitride cantilever. Its design and low heat capacity guarantee a small contribution of the probe to the local thermal environment. This probe was fabricated by Kelvin Nanotechnologies at the James Watt Nanofabrication Centre of the University of Glasgow. The main point of the fabrication process is the deposition of a 200-nm-thick Si_3N_4 film on one side of a standard Si tip. Then, the Si tip and its cantilever are removed via wet etching, leaving a free-standing Si_3N_4 cantilever attached to a Si carrier chip (fig.2.3), which is much bigger than the tip, meaning that its temperature remains unperturbed during the measurement. The AFM tip is defined by a tilted triangular extremity of the silicon nitride cantilever. The tip represents the basis over which a resonant nanoantenna is positioned. The fabrication is performed by electron beam lithography (EBL). By properly designing the nanoantenna and exploiting its resonances, we can increase the optical confinement in the sample, even more than the case of the standard Au-coated silicon tip. Indeed, its geometry is tailored to bring the first-order dipolar resonance at 6 µm, close to the vibrational line of PMMA probed by the QCL (at 5.78 µm). The material of choice is palladium. At resonance, the nanoantenna shows a field profile like the one in fig.2.3 (panel c), showing an enhancement of two orders of magnitude. Moreover, the resonant distribution of the Pd patch confines the field more effectively than in the Au tip, allowing for a better sensitivity to truly superficial effects. Both of these effects are due to the tailored geometry of the finite-length Pd patch, in contrast to the indefinitely extending gold tip, which does not have a resonant behavior. Indeed, these qualities can potentially make the Pd tip an ideal probe specifically for PTIR.

Thus, one objective of the experiment is also to compare the performance of the two tips: two identical sets of measurements are carried out, so that a direct comparison is possible.

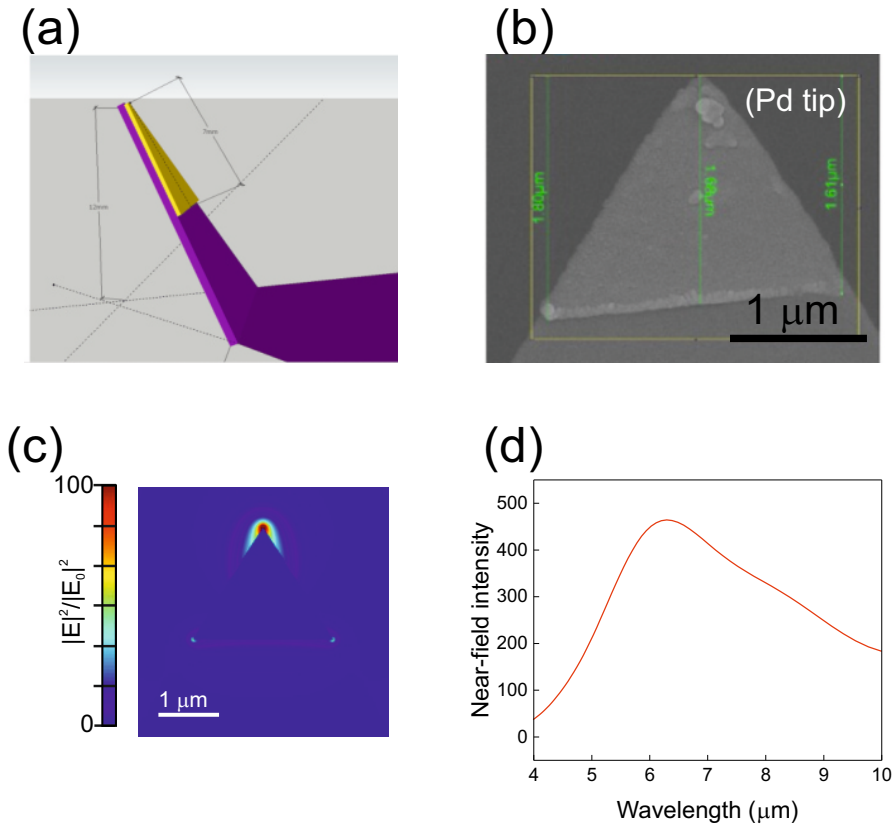

Figure 2.3: In panel a, the geometry of the AFM tip: the golden triangle represents the Pd patch, while the tilted Si_3N_4 cantilever is in purple. In panel b, the SEM image of the Pd patch. In panel c, the near-field ditribution of the Pd patch at 5.78 µm, the wavelength probed in the experiment. In panel d, the near-field intensity spectrum of the tip, showing a resonance around 6 µm

2.2.2 The REINS technique

For the detection of the PTIR signal, the resonantly enhanced infrared photoexpansion nanoscopy (REINS) technique was adopted. As previously discussed, in a PTIR experiment an infrared light illuminates the sample, whose thermal expansion is sensed by an AFM tip. As a source of illumination, we can use a pulsed laser, quantum cascade lasers (QCL) representing one of the most commonly employed archetypes. The main advantages of QCLs are their stability, compactness and tunability. Being able to sweep the wavelength and the repetition rate of the laser pulses is crucial in a PTIR experiment. Indeed, since the AFM is operated in contact mode, the cantilever shows a set of mechanical resonances, with a typical quality factor $Q \approx 50$, and these resonances can be exploited by properly tuning the repetition rate of the QCL. When the repetition rate of the illumination matches the frequency of a cantilever mechanical mode, the PTIR signal is magnified by the quality factor of the cantilever resonance. This is the main

principle of the REINS technique. This technique was first demonstrated by F. Lu and M.A. Belkin in 2011 [54].

On a practical level, in a REINS experiment, the thermal expansion of the sample forces the resonant oscillation of the cantilever around its initial position, and this is repeated at the frequency of the laser pulses. Finally, the detected PTIR signal is the amplitude of the cantilever oscillation. It is collected and demodulated by a lock-in amplifier (LIA), neglecting all the thermal and mechanical effects which are not at the laser repetition frequency. Moreover, the employment of a LIA allows for the integration over many laser pulses, to increase the signal to noise ratio. Since this technique is based on several time-dependent phenomena (thermal expansion of the sample, duration and repetition of the laser pulses, LIA integration), it is important to check and compare the temporal dynamics of all the processes, most importantly the photothermal expansion of the sample. This will be thoroughly discussed in a successive paragraph, with dedicated transient simulations.

On a theoretical level, the amplitude of the cantilever oscillation Δz_{cant} can be derived by solving the second-order differential equation describing the oscillation of the tip:

$$\frac{d^2 z_{\text{cant}}}{dt^2} + \frac{\omega_0}{Q}\frac{dz_{\text{cant}}}{dt} + \omega_0^2 z = \frac{F(t)}{m^*}, \tag{2.1}$$

where ω_0 is the cantilever mode frequency, Q the quality factor of the resonance, m^* is the effective mass of the probe tip. The REINS technique has been utilized in many applications, especially for increasing the signal to noise ratio in biosensing experiments [3, 43, 55], for example the detection of tens of molecules of a phenolic compound [56]. In our experiment, we have two different AFM probes, the Au and the Pd tips. Their mechanical modes have been characterized at Sapienza University with an Anasys Instrument nanoIR2 microscope, collecting the mechanical contribution of the thermal noise. First, let us consider the Pd tip. This tip is not only peculiar for its confinement, but also on a mechanical level. Indeed, machanically, the tip is represented by a 200-nm-thick tilted layer of Si_3N_4, forming an angle of 20° with the sample surface. This is completely different from the conical shape of the typical AFM probes, such as the Au tip. The bending mode spectrum of this tip, when in contact with the QCL turned on, is depicted in fig.2.4. The red, blue and green curves correspond to different repetition rates of the QCL pulse: 100, 120 and 140 kHz respectively. When the repetition rate matches one of the bending modes appearing in this configuration the signal is greatly increased. This can be seen in the red curve, when the third harmonic of the QCL repetition rate (300 kHz) almost mathces the mode at 305 kHz: the peak is strongly magnified compared to the blue and green curves. This corresponds to the REINS situation. The mode at 305 kHz is the one chosen to be employed in the Pd set of measurements, and it will be excited with a matching repetition rate of the laser, at 305 kHz. The Q-factor of this mode can be estimated by measuring its linewidth (around 5 kHz): $Q \approx 60$.

For the Au tip, mounted on a standard Si cantilever, the bending modes are weaker and are observable only in the REINS condition. The mode used in this case is at 200 kHz with a linewidth around 5 kHz, giving a Q-factor around 50.

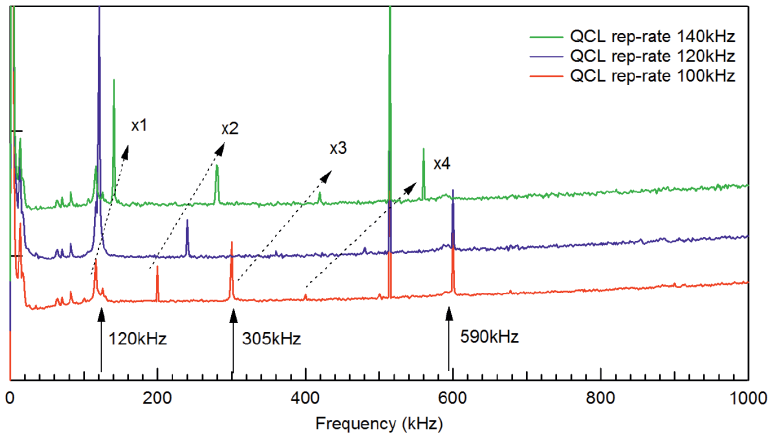

Figure 2.4: The spectrum of the contact-mode AFM mechanical resonances when the QCL has a repetition rate of 100 (red curve), 120 (blue curve) and 140 (green curve) kHz for the Pd tip. When the repetiton rate matches the frequency of a peak, the resonance is greatly enhanced (can be seen at 120 kHz for the blue curve). This is the so-called REINS configuration.

2.3 The PTIR experiment

The experiments presented in this section have been performed at Sapienza University, by employing the Anasys nanoIR2 setup, specifically designed for PTIR measurements. The effect of the two AFM probes is studied, with two separate sets of mesurements. The sample under investigation is a whisker of polymethilmethacrylate (PMMA), with a thickness increasing from 10 nm to 600 nm over a 10-µm length, while the width changes from 30 nm to 2 µm (fig.2.5). The sample is fabricated via electron beam lithography (EBL) over a 300-nm-thick gold film, deposited on top of a Si substrate. As already discussed, the presence of a gold-substrate allows for the establishment of a plasmonic nanocavity between the metallic tip, the Au lightning rod or the Pd antenna, and the Au-substrate. Thus, the nanocavity overlaps with the sample scanning position, improving the optical absorption and confinement inside the film. In the end, this configuration increases the sensitivity and resolution of the PTIR signal.

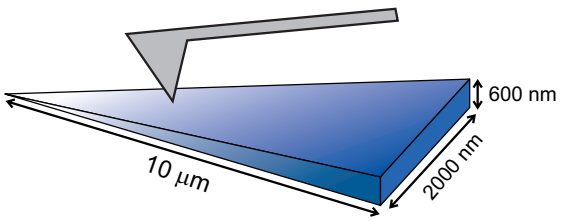

Figure 2.5: Pictorial depiction of the PMMA whisker investigated by the AFM tip

The source of illumination is a QCL emitting in the wavelength range of 5.8 to 6.3 µm. The QCL illuminates the sample forming an angle of 70° with the normal to the whisker surface. The intensity of the light is around 10^7 W m^{-2}, while the repetition rate matches one of the bending modes of the cantilever (200 kHz for the Au tip, 305 kHz for the Pd tip) in a REINS configuration, enhancing the signal by the Q-factor of the cantilever bending modes. The pulses are 260-ns long: this timescale is crucial in modelling the thermalization dynamics of the sample. The target wavelength is 5.78 µm, which excites a vibrational mode of PMMA and is reachable by the QCL. Both AFM probes are operated in contact mode, detecting the thermal expansion consequent to the resonant optical absorption of the PMMA whisker. The geometry of the sample allows us to study how each tip affects the dependence of the PTIR signal on the thickness, by performing the same measurement at several positions on the whisker, corresponding to different values of the thickness. The PTIR raw data consist in the signal on a portion of spectrum, reaching the minimum wavelength of the QCL. The PTIR raw data is reported in fig.2.6 for both tips (panel a for the Au tip and panel b for the Pd probe) and increasing thickness of PMMA. From this data, we can perform a Lorentzian fitting of the PMMA absorption line. In fig.2.6, an AFM topography map (panel c) and a representative PTIR map are also reported (panel d).

After the fitting process, we retrieve two trends of the PTIR signal as a function of the film thickness, which represent a meaningful experimental benchmark of the PTIR technique. From this dataset, the behavior associated with the two tips can also be compared, to extrapolate the effect of their optical and mechanical properties on the PTIR signal.

The results of the experiment are reported in fig.2.7. First, we can notice the different behavior coming from the two probes, meaning that the tip optical, mechanical and thermal properties effectively affect the PTIR signal. In particular, the Au tip shows a roughly linear behavior, while the Pd patch shows a sublinear dependence on the PMMA thickness. The error bars come from the standard deviation of the Lorentzian fitting of the PTIR raw data.

The two trends are not in agreement with previous models found in literature. In particular, the general theoretical background for the PTIR technique was given by Dazzi *et al.* in 2010, focusing on the mechanical modelling of a PTIR experiment. This model predicts a quadratic dependence on the sample thickness, in the case of a spehrical sample, providing a qualitative interpretation for other geometries. However, the film-on-substrate situation shows strong differences, especially in the definition of the heat flow, which is governed by the thermal boundary conditions. Also, the proposed model does not look into the effect of a non-uniform field distribution, leading to a more confined temperature increase, while this could be a factor in our case. Indeed, the measurements I am discussing are discordant with the predicted quadratic behavior of the PTIR signal on the thickness and show a dependence on the properties of the AFM tip. Aside from this general analysis, more specific models have been presented in the literature. One of them was proposed by Lu *et al.* in 2014, where the PTIR signal is studied as a function of the AFM indentation depth [55]. This model is valid for

extremely thin samples, such as molecular monolayers, so it cannot be extended to our situation. O'Callahan *et al.*, in 2018, studied the forces acting on the AFM probe in a PTIR measurement [57]. However, they developed a simplified model, in which the heat transport equation is not considered, and the thermal expansion is a direct consequence of the optical absorption in the sample. Since PTIR is a relatively novel technique, a common theoretical environment has not been estabilshed.

Thus, our aim is to develop a more complete model, explaining our results. In particular, our final aim is to single out the main physical contributions responsible for the deviation of these results from what we would expect employing previous models.

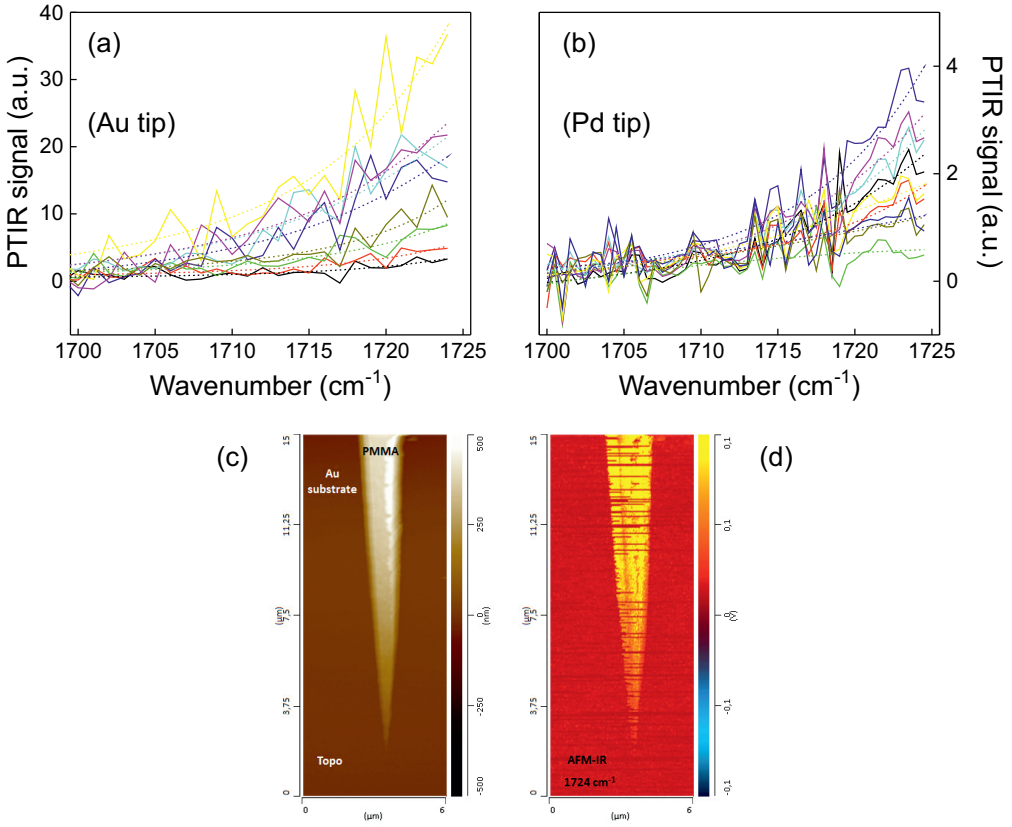

Figure 2.6: In (a) and (b), the PTIR raw data for the Au and Pd tip, respectively (solid lines are the PTIR raw data, dotted lines represent the correspondent lorentzian fit). In (c), the AFM topography map of the PMMA whisker. In (d), a representative PTIR map.

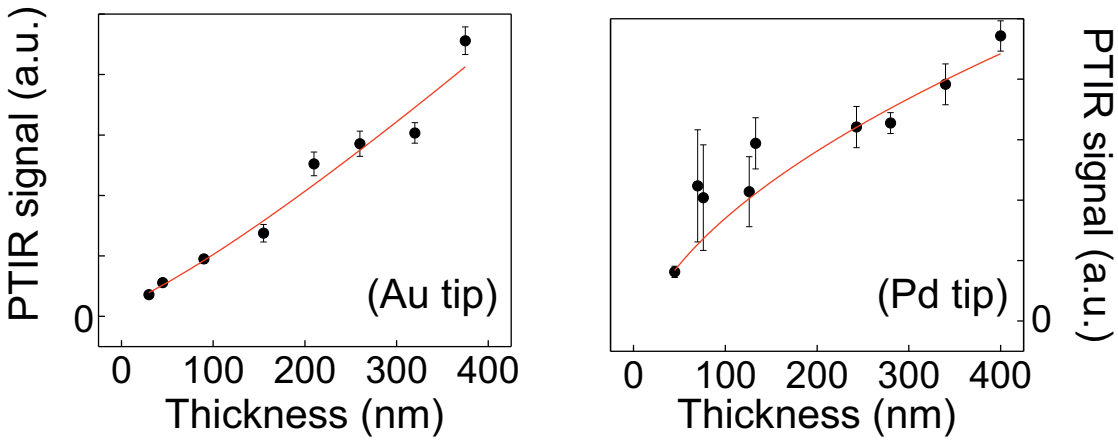

Figure 2.7: The dependence of the PTIR signal on the thickness of the sample, experimentally collected employing the Au (panel a) and the Pd tip (panel b). The red line is a guide for the eye.

2.4 The PTIR modelling

2.4.1 The simulated PTIR signal

The PTIR signal collected in the experiment is the oscillation amplitude of the AFM cantilever, which is caused by the thermal expansion of the sample acting on the tip. The oscillation amplitude is found as the solution of the equation:

$$\frac{d^2 z_{\text{cant}}}{dt^2} + \frac{\omega_0}{Q}\frac{dz_{\text{cant}}}{dt} + \omega_0^2 z = \frac{F_{\text{driving}}(t)}{m^*}, \tag{2.2}$$

as already reported in section 2.2.2. The driving force of the cantilver oscillations $F_{\text{driving}}(t)$ is the periodic repetition of the thermal expansion force $F_{th}(t)$ at every QCL pulse. This can be expressed as:

$$F_{\text{th}}(t) = E\frac{\Delta z(t)}{z_0}, \tag{2.3}$$

where E is Young's modulus of the sample, Δz is the thermal expansion and z_0 the total thickness of the film. At every instant, we calculate the thermal expansion Δz with the integral:

$$\Delta z(t) = \int_0^{z_0} \alpha_{\text{th}} \Delta T(z,t) dz, \tag{2.4}$$

where α_{th} is the linear thermal expansion coefficient fo the material, $\Delta T(z,t)$ is the temperature increase distribution along the thickness of the film. Thus, all we need to know is the temperature distribution inside the film at every instant in time, in order to compute the thermal expansion force. In a steady-state scenario, the sample has enough

time to fully thermalize and F_{th} is constant in time during the pulse duration. In this case, $F_{\text{driving}}(t)$ is a square wave of amplitude F_{th}, lasting the duration of a QCL pulse $\Delta\tau_{\text{QCL}} = 260$ ns and repeating with a period $T = 1/f_{\text{QCL}}$. In this case, the solution of the eq.2.2 $z_{\text{cant}}(t)$ is directly proportional to the amplitude of the square wave, the thermal expansion force at steady-state. So, when we perform steady-state simulations the PTIR signal is represented by F_{th}. This approach has been already extensively used in literature [55, 57]. When the steady-state approximation is not valid, F_{th} has a temporal dependence. In this case, the driving force $F_{\text{driving}}(t)$ corresponds to the time-dependent thermal expansion triggered at every QCL pulse and eq.2.2 has to be solved numerically. Thus, $z_{\text{cant}}(t)$ is explicitly calculated and corresponds to the PTIR signal.

2.4.2 The simulation workflow

In this paragraph, I will report all the steps performed in order to model the PTIR measurement. The whole model is composed of optical simulations, thermal simulations and the differential equation describing the AFM cantilever motion. First, we perform optical simulations to find the optical absorption of the sample. These simulations are done with the FDTD method [23]. Their output is a matrix reporting the optical power absorbed in every cell of the sample mesh. This matrix is then imported in the solver HEAT, performing the thermal simulations [24]. Here, the optical absorption matrix acts as a heat source, which is turned on for the laser pulse duration. As a result, we obtain the temperature distribution in the sample and its temporal evolution. The temperature increase is associated to a thermal expansion force acting on the AFM tip. This term represents the driving force in the differential equation describing the motion of the cantilever. The differential equation is solved with a commercial numerical solver [58]. The result is the oscillatory motion of the cantilever. In the end, we compute the amplitude of this oscillation to retrieve the PTIR signal.

All the simulations reported are in two dimensions, while the third one is considered infinite. Indeed, the length of the PMMA whisker, which is around 10 µm, is much larger than the other characteristic dimensions of the sample, on the order of 1 µm maximum. Moreover, the main features of the two tips (lightning-rod effect and localized resonance) can be fairly captured also in the frame of a 2D simulation. This is done to reduce the memory and temporal requirements of every simulation. In order to study the behavior of the PTIR signal with the sample thickness, we simulate different 2D geometries of the PMMA film, following the scaling of the whisker. In table 2.1, the simulated dimensions (width and thickness) are reported. The same PMMA geometries are simulated for both AFM probes, the Au and Pd tips. In the end we obtain two sets of simulated data replicating the experimental dataset.

Thickness [nm]	Width [nm]
10	33
20	65
40	130
80	260
120	390
160	520
240	780
320	1040
400	1300

Table 2.1: Set of simulated dimensions for the PMMA whisker.

2.4.3 Optical simulations

Following the simulation workflow, we start with optical simulations to evaluate the power absorbed by the PMMA whisker. For both tips we employ a plane wave illumination centered at 5.8 µm wavelength, impinging with a 70° inclination on the PMMA film. The plane wave is modelled in FDTD with a total-field scattered-field (TFSF) source. The boundary conditions are modelled through perfectly matched layer (PML) boundaries, extending indefinitely the air surrounding the simulation environment. The optical simulation environment is reported in fig.2.8, for both tips. The PMMA is a rectangle with the dimensions taken from the actual sample cross-section as reported in table2.1. Its permittivity at 5.8 µm is modelled as $\epsilon'_{\mathrm{PMMA}} = 2.80$ and $\epsilon''_{\mathrm{PMMA}} = 0.80$. The Au tip is modelled with a sphere of radius $r = 50$ nm indented by 2 nm in the PMMA sample. The Pd tip is designed as an oblique rectangle in contact with the sample surface, with the same 2-nm indentation, while the Pd patch is a 200-nm thick rectangle not touching the sample, as inferred from the SEM images of the tip. The Au, Si_3N_4 and Pd permittivities are taken from the FDTD material library. In fig.2.9 (panels a and b) the electric field distribution near the two tips is depicted. We can see that for the Au tip, there is a strong enhancement close to the sphere, but a nonzero field is also present almost uniformly in the PMMA, whereas for the Pd tip, the field is much more confined around the Pd patch apex, showing a hotspot in air. For this reason, this tip is more sensitive to the surface of the sample: indeed, in the PMMA the field is not uniformly distributed as for the Au probe. This is also confirmed by looking at the decay of the electric field intensity along the PMMA thickness for both tips (simulated for PMMA thickness of 400 nm), also represented in fig.2.9 (panels c and d). The decay is obtained by integrating on a 200-nm-wide area below the tip to smooth any spurious effect. In the case of the Au tip, the decay stops at a constant asymptotic value, around 40% of the initial value, confirming the more uniform distribution described previously. Indeed, the decay in the Pd case does not reach an asymptotic value and decreases down to the 10% of its initial value. The different confinement of the tips is the main reason why two different behaviors are observed experimentally. In fact, when the sample

thickness is increased a larger volume absorbs light, meaning that a higher signal will be observed. However, the Pd tip confines the enhancement and therefore the absorption close to the surface, so the contribution from bulkier samples is weaker. As we will confirm with the modelling, this leads to a saturation of the PTIR signal, which is reflected by the sublinear behavior observed experimentally. On the other hand, a more uniform field is sensitive to larger absorptive volumes, leading to stronger contributions at high thicknesses. This is the case of the Au tip, showing a linear dependence on the PMMA thickness.

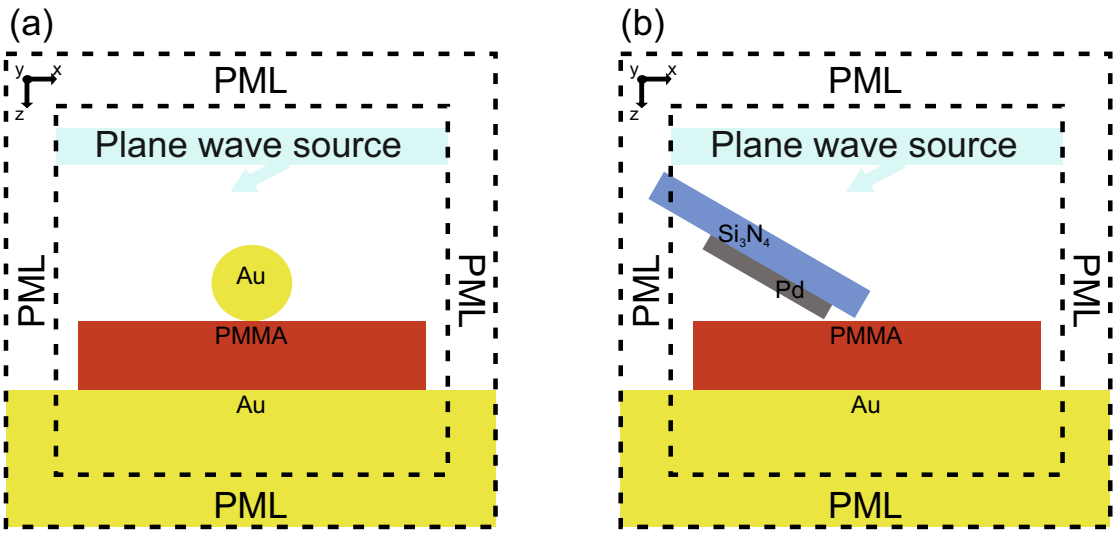

Figure 2.8: Sketch of the optical simulation environment for the Au tip (panel a) and the Pd tip (panel b).

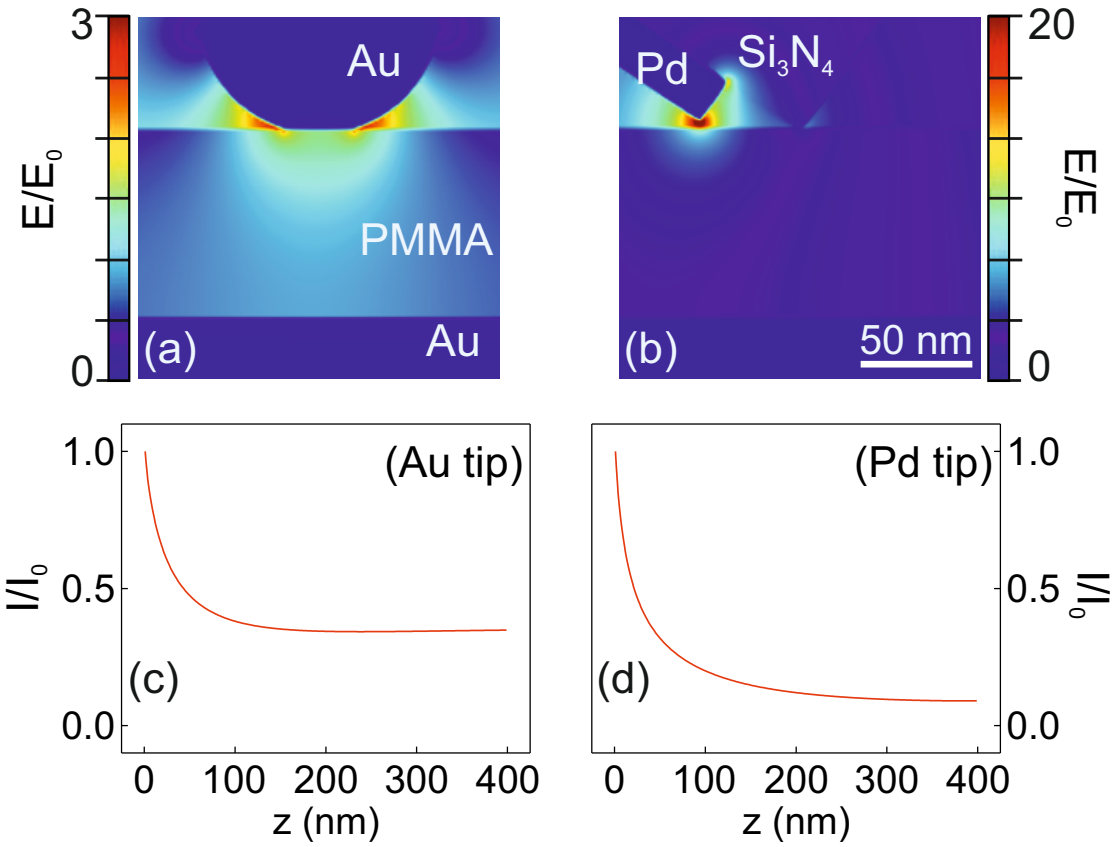

Figure 2.9: In panels a and b, the near-field fistribution for the Au and Pd tips, respectively. We can see that the resonant probe establishes a stronger and more confined field enhancement. In panels c and d, the profile of the field intensity along the 400-nm thick PMMA film, for both tips. The Au tip (panel c) shows a more uniform field than the Pd one (panel d).

At the end of the optical simulations, we collect the optical power absorbed by the PMMA per unit volume at the frequency ω (corresponding to the exictation wavelength, $\lambda = 5.8$ µm). This is done by employing an analysis tool, which computes the formula: $P_{\text{abs}} = \frac{1}{2}\epsilon_0\omega|E|^2\text{Im}(\epsilon)$ at every vertex of the FDTD mesh. In the formula, E is the electric field at the mesh vertex, $\text{Im}(\epsilon)$ the imaginary part of the material permittivity. In fig.2.10, I report two representative distributions of P_{abs} for the two AFM probes. As expected, they follow the electric field distributions in the PMMA, while the P_{abs} in the Au substrate is negligible, since Au behaves like a perfect conductor in the MIR. Finally, we obtain a matrix storing the value of P_{abs} in the sample, which will be used as a heat source for the thermal simulations.

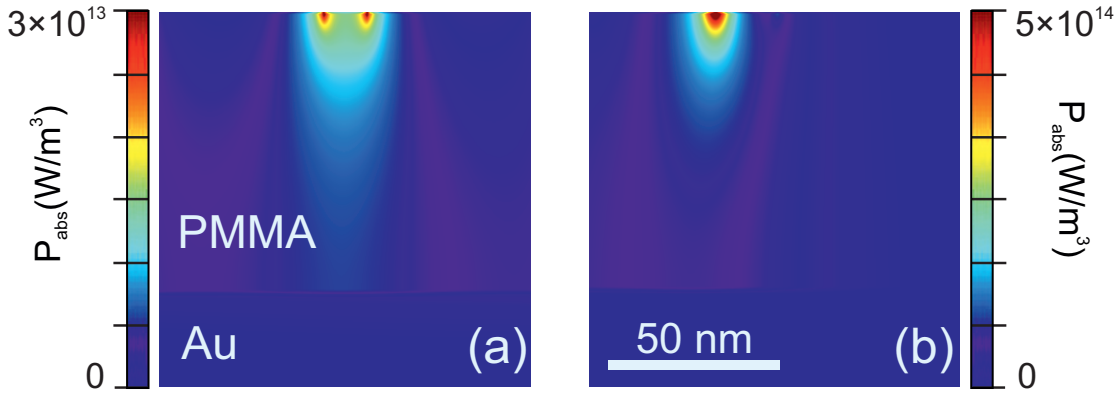

Figure 2.10: The optical power absorbed in the 80-nm-thick PMMA film, as calculated by FDTD, for the Au tip (panel a) and Pd tip (panel b).

2.4.4 First set of thermal simulations

The geometry of the thermal simulations is the same of the optical ones, apart from the addition of the Au coated cone for the Au tip. Regarding the thermal boundary conditions, we have to consider that the substrate and the cantilever have much larger volumes than the tip and the PMMA film, so their temperature will be unperturbed by the local heating of the sample. To model this situation, we impose a fixed temperature of 300 K at the cantilever and at the bottom of the Si substrate. So, the upper and lower surfaces will act like heat sinks. The material properties needed to solve the heat transport equation are the mass density, the specific heat and the heat conductivity. For Au, Si, Pd and Si_3N_4 we use the HEAT database, while for PMMA we employ a density $\rho_{\mathrm{PMMA}} = 1190\ \mathrm{kg\,m^{-3}}$, specific heat $c_{\mathrm{p,PMMA}} = 1466\ \mathrm{J\,kg^{-1}\,K^{-1}}$ and heat conductivity $\eta_{\mathrm{PMMA}} = 0.18\ \mathrm{W\,m^{-1}\,K}$. As said, the thermal source is given by the optical absorption matrix imported from FDTD. In our initial approximation, we perform steady-state simulations, so we assume that the sample has enough time to thermalize while the thermal source is on. Referring to the experiment, this means that the pulse duration of the QCL is much longer than the thermalization time of the sample. In other words, in this set of simulations, the QCL pulse duration is considered infinite. This is certainly true for thin parts of the whisker (up to 100 nm), however in the case of high thickness it may not be true. A thorough discussion on this assumption will be given within a dedicated section.

The results of this set of simulations are reported in fig.2.11. In panel a and b we can see the temperature distribution for the Au and Pd tip respectively, in the case of the 80-nm-thick simulated sample. The heating is mainly confined in the PMMA, while the tip and the substrate are unperturbed. The temperature distribution depends on the optical power absorption profile, which is tailored by the optical properties of the AFM probe. So, the same sample will show different behaviors depending on the employed tip, as we see in the experimental datasets. In particular, the Au probe is responsible for a broader and more uniform temperature increase, interesting a deeper

volume of the whisker. On the other hand, we can see a more confined hotspot below the Pd tip. These qualitative considerations are in agreement with what observed in the experimental dataset: the more confined temperature increase in the case of the Pd tip implies that the deeper parts of the whisker are not reached by the heating. This means that the PTIR signal will not increase considerably when increasing the thickness over a certain value, and indeed we observe a saturation in fig.2.7 (panel b, the sublinear behavior). On the contrary, the Au tip is associated to a more uniform heating over the whole thickness of the film, and this is confirmed by the linear experimental trend.

However, both temperature distributions share a common feature: the contact between the tip and the sample establishes a cold spot in the PMMA film. On a physical level, this means that the tips perturb the temperature distribution in the PMMA, "cooling down" the contact area with the sample. In other words, the probes impose their own temperature in the proximity of the point where they touch the PMMA film. This does not represent a physical situation. Indeed, the tips can perturb the sample, however the thermal contact between them has to be properly modelled. In this set of simulations the contact is ideal, meaning that there is no physical condition opposing to the heat flow between a body to another (i.e. the tip and the film). So, the heat going from the tip to the sample (and vice versa) only experiences a jump in the thermal conductivity due to the change of the medium. However, the contact between the two objects is not perfect, and this non-ideality perturbs the heat flow. In the following we will discuss a crucial parameter, the interface thermal resistance (ITR), which models the resistance felt by the heat flow when travelling from one medium to another one.

Panels c and d in fig.2.11 report the dependence of the PTIR signal on the sample thickness. In the steady-state situation, the PTIR signal is proportional to the thermal expansion force felt by the tip. Looking at the two graphs, we can see that the PTIR signal is superlinear for the Au tip (panel c) and roughly linear in the case of the Pd tip (panel d). First, we succesfully confirm the difference in behavior for the two probes, as observed in the experiment, mainly due to their diverse optical confinement, as discussed in the previous section. This is a first confirmation of the accuracy of our model. However, the experimental data show an approximately linear trend for the Au tip and sublinear for the Pd tip, in contrast with the trends shown in panel c and d. This means that our modelling is not describing the experiment correctly yet, especially for the Au tip.

In particular, there are two missing ingredients:

- The ITRs, modelling the heat flow through the interface between two different objects. These effectively become boundary conditions at the PMMA upper and lower surfaces.
- The finite duration of the QCL pulse, meaning that the thermal source is on for 260 ns in our simulations, and the temporal evolution of temperature increase must be considered.

In the following sections, I will present the effects of these two ingredients, first keeping the steady-state approximation and adding the interfacial thermal resistances, then

considering also the transient evolution of the system.

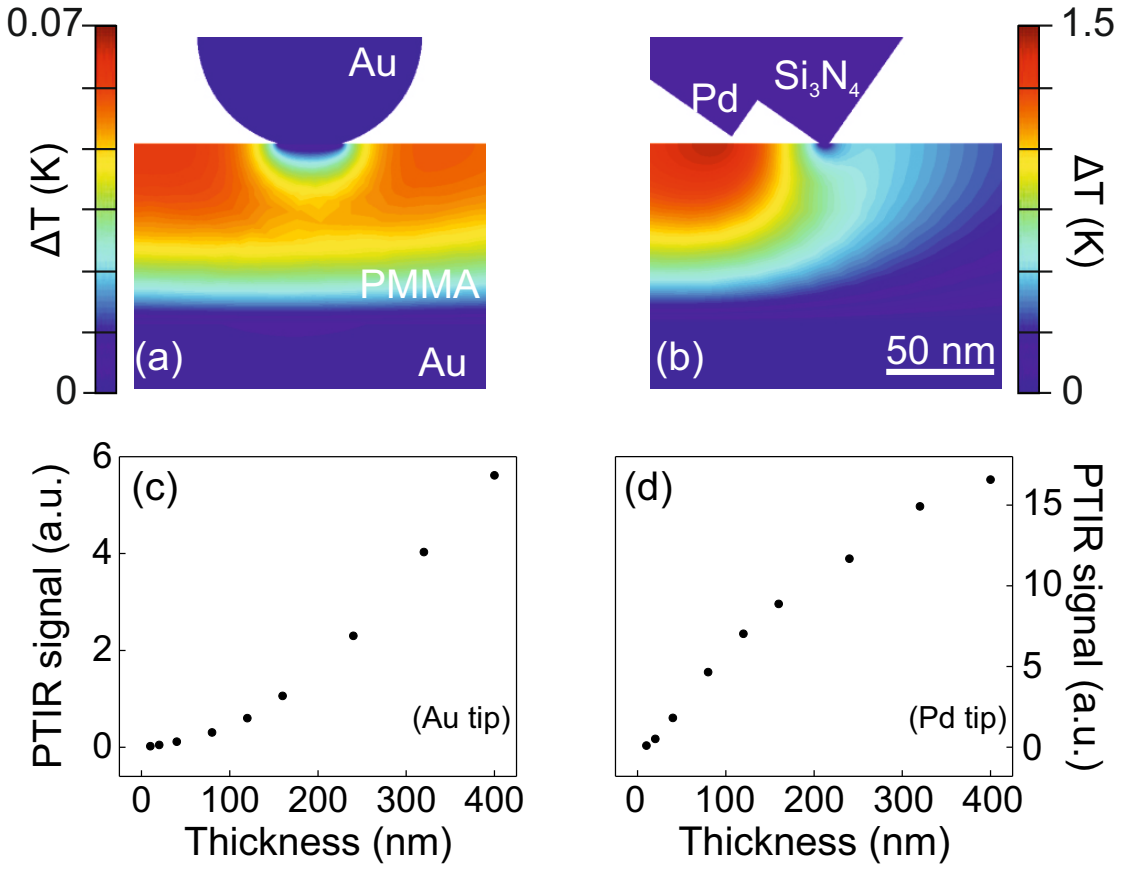

Figure 2.11: Steady-state temperature distribution in a 80-nm-thick PMMA film, for the Au (a) and the Pd tip (b). In both figures, we can appreciate a cold spot below the tip, due to the ideal thermal contact between the tip and the sample in the simulations. In panels c and d, the simulated dependence of the PTIR signal on the sample thickness. For the Au probe (c) the behavior is superlinear, for the Pd probe (d) it is roughly linear. Each trend is not in agreement with the corresponding experimental one.

2.4.5 The interfacial thermal resistances

When two bodies at different temperature are in contact, a heat current flows from the warmer to the colder body, as predicted by Fourier's law. However, when heat flows through an interface between two objects, some effects have to be considered. Indeed, the physical environment at the interface is different from the bulk one, and in a more realistic description the two bodies are not completely adherent along a flat interface. This means that the heat current feels an impedance when transferring from one body to another, which imposes a temperature discontinuity at the interface. This impedance

is the so-called interfacial thermal resistance (ITR), and it relates the heat flux to the temperature discontinuity:

$$j(z) = \frac{\Delta T}{R}, \tag{2.5}$$

where ΔT is the temperature difference across the interface and R the interfacial thermal resistance per unit area, measured in $\mathrm{W^{-1}\,m^2\,K}$. Let us first describe the effect of the ITR with a simple one-dimensional model. If we write Fourier's law in 1D, we have

$$j(z) = -\eta \frac{dT}{dz}. \tag{2.6}$$

At the interface $z = 0$, combining 2.5 with 2.6, we obtain

$$-\eta \frac{dT}{dz} = \frac{T(0^+) - T(0^-)}{R}, \tag{2.7}$$

which represents a boundary condition relating the temperature with its first derivate. This boundary condition confines the heat in the warmer body, with an effect depending on the value of R: as R increases, the confinement becomes stronger.

With these considerations in mind, it is important to understand the role of ITRs in the PTIR modelling. Indeed, the scale of the investigated PMMA whisker (hundreds of nm thick at maximum) suggests that interfacial effects can be particularly relevant. So, we have to properly design the ITRs acting at the interfaces of PMMA with the tip and the Au substrate. We explore values of ITR between 10^{-8} and 10^{-7} $\mathrm{W^{-1}\,m^2\,K}$. We chose these orders on magnitude based on two references, a review on ITR by Chen *et al.* (2022) [59] and a work by Chae *et. al* (2017) [2]. In particular, the latter describes a dedicated PTIR set-up, able to determine the heat conductivity of a very thin material (down to 10 nm of thickness). In this work, the measured heat conductivity is observed to have a dependence on the thickness of the sample, especially for very thin films (on the order of tens of nm). However, for thicknesses of hundreds of nm, the thermal conductivity reaches a constant value, corresponding to the bulk value of the material (fig.2.12). The deviation from the bulk value at small values of the thickness is attributed to the presence of ITRs, affecting the PTIR measurement. We interpret the trend in fig.2.12 as a result of a series of three thermal resistances, one from the bulk (modelled as $R_{\mathrm{bulk}} = \frac{1}{\eta_{\mathrm{bulk}}} \frac{l}{S}$, where η_{bulk} is the bulk thermal conductivity of PMMA, l the thickness of the sample and S its surface) and two at the interfaces of PMMA (equal in value, R_{int}). By employing this simple model, we can extrapolate a characteristic value of resistance of unit area at a prototypical PMMA interface, on the order of 10^{-7} $\mathrm{W^{-1}\,m^2\,K}$.

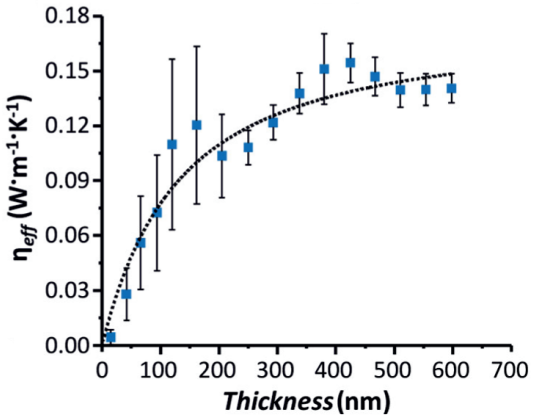

Figure 2.12: The thermal conductivity of PMMA as a function of the thickness measured by Chae *et al.*. The deviation from the constant bulk value is due to the presence of ITRs affecting the measurement. Adapted from ref. [2].

2.4.6 Understanding the role of ITR

In order to understand the role of the ITRs in the PTIR experiment, we momentarily simplify our analysis, passing from a 2D model to a 1D model. This approximation is based on the assumption of a uniform temperature in the area below the tip, so that we can just consider the temperature evolution along the vertical line passing through the tip apex. The 1D model allows for a quicker and more evident evaluation of the role of ITRs. In fact, here we can insert them as an analytical boundary condition at the upper and lower surfaces of the PMMA, while in the 2D model (in the solver HEAT) we will have to simulate them through an effective medium, which will be discussed in the next section. For this reason, we call the first approach the "semi-analytical" model: the heat equation is solved numerically by employing a commercial code, while the ITR are modelled analytically [58].

We write the heat transport equation in one dimension as:

$$-\eta \frac{d^2T}{dz^2} = Q(z). \tag{2.8}$$

Here $Q(z)$ is a source term in function of the PMMA thickness, coming from the simulated field intensity in the film (i. e. panels c and d of fig.2.9). In this model, the effect of the tip is enclosed in its optical contribution, represented by $Q(z)$. At first, as boundary conditions, we impose two heat sinks at the tip/PMMA and PMMA/substrate interfaces (de facto replicating the boundary conditions imposed in section 2.4.4, since the tip and the substrate remained unperturbed). This translates into:

$$T(0) = T(z_0) = 0, \tag{2.9}$$

where $z = 0$ and $z = z_0$ are the coordinates of the tip/PMMA and PMMA/substrate interfaces, respectively. This situation is represented in panel a of fig.2.13. We solve this

equation for the geometries of the PMMA listed in table 2.1, extracting the dependence of the PTIR signal on the sample thickness. The results obtained with this configuration are reported in fig.2.14 (panels a and b). The two trends are extremely similar to the ones reported in section 2.4.4, confirming the validity of the 1D approximation. However, they are still far from the experimental results.

Now we evaluate the role of the ITRs. In order to employ them, we change the boundary conditions to:

$$\begin{aligned} J(0) &= -\eta \frac{dT}{dz} = \frac{T(0^+) - T(0^-)}{R_1} \\ J(z_0) &= -\eta \frac{dT}{dz} = \frac{T(z_0^+) - T(z_0^-)}{R_2}. \end{aligned} \tag{2.10}$$

This situation is depicted in panel b of fig.2.13. With these boundary conditions we impose a jump in temperature at the two interfaces. We still consider the tip and the substrate unperturbed, meaning that $T(0^-) = T(z_0^+) = 300$ K, while in the PMMA in general $T(z) \neq 300$ K. The temperature jump at the two interfaces is related to the heat flux j, thus to the first derivative of the temperature itself, $\frac{dT}{dz}$. As discussed, the value of the ITR depends on the contact between the interacting bodies, which is much different at the two interfaces. However, for the sake of simplicity we will consider symmetrical values at this stage ($R_1 = R_2 = R$), improving the ITR modelling in the next section.

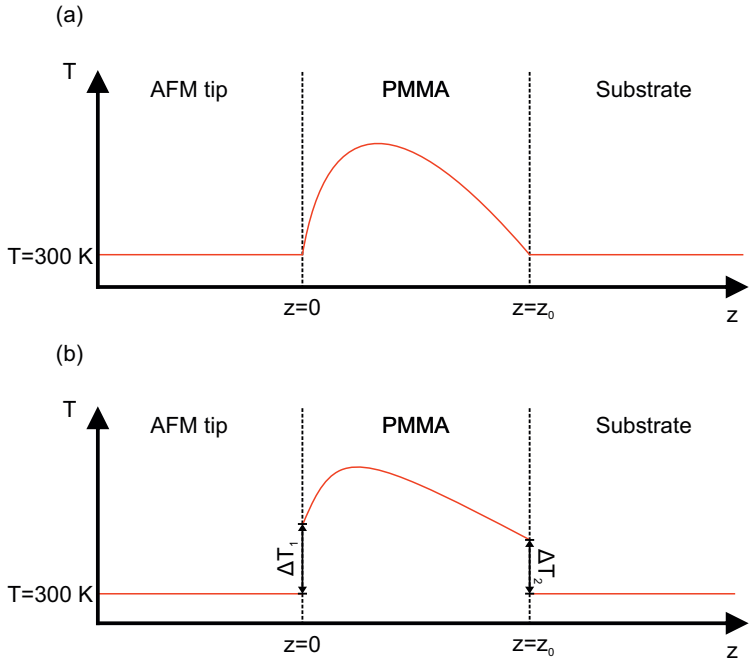

Figure 2.13: In (a), sketch of the simulated thermal environment in the semi-analytical model without ITRs. In (b), we employ ITRs at the tip/PMMA and PMMA/substrate interfaces.

The results of these simulations are depicted in panels c and d of fig.2.14, for different values of R. In these graphs we can see that the trends of the PTIR signal are changed from the previous set (panels a and b) and that they are dependent on the value of R. Indeed, as we increase R the Au plot bends towards linearity, and the Pd one tends to be sublinear. Both of them are in better agreement with the experimental results than in panels a and b, meaning that ITRs represent a crucial ingredient in modelling a PTIR experiment. Thus, in the next section, we employ them also in the 2D simulations, with a proper model.

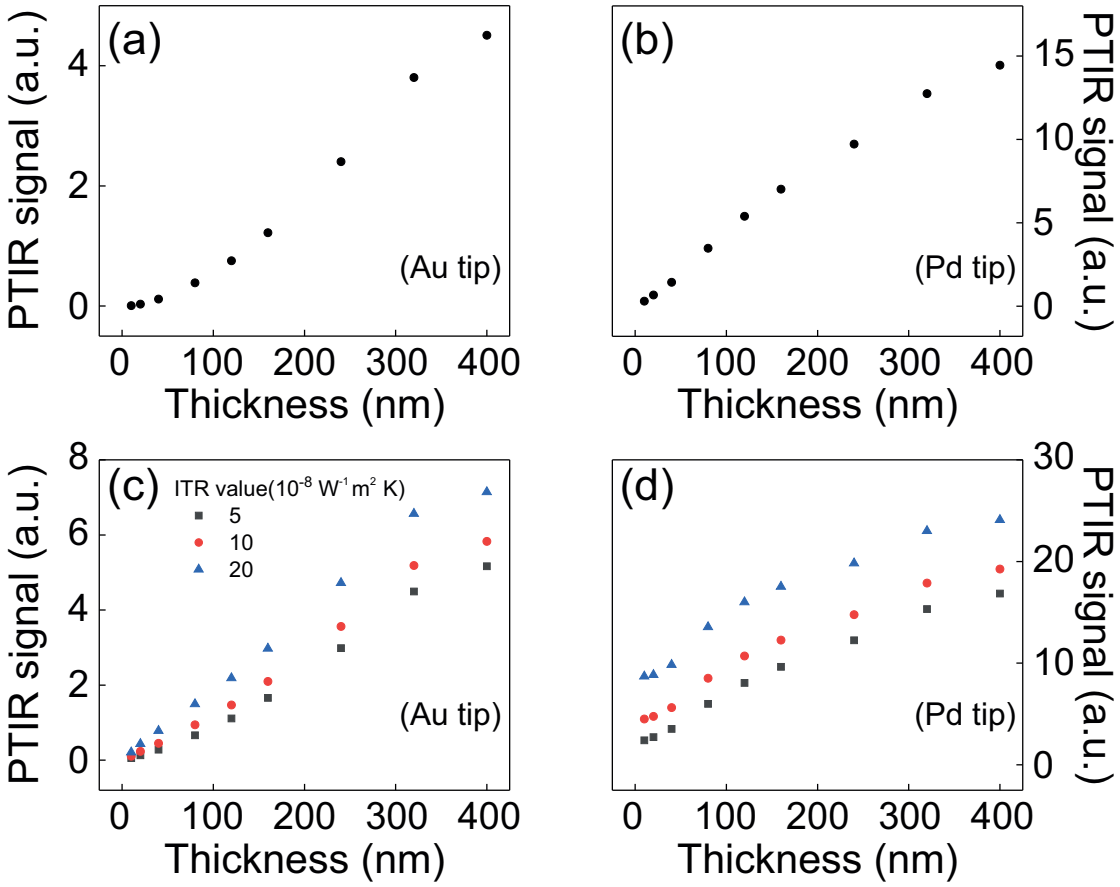

Figure 2.14: The behavior of the PTIR signal computed with the semi-analytical model. In (a) and (b) no ITR is employed, while in (c) and (d) we employ an ITR at each PMMA interface (the ITR value is reported in the legend).

2.4.7 Second set of thermal simulations

We now perform a new set of 2D simulations adding the ITR to our simulations. In order to model them, we add a strongly insulating layer at the PMMA/tip and PM-

MA/substrate interfaces and to simulate their interfacial effect we make these layers as thin as possible. HEAT can resolve 0.1 nm-thick layers with a reasonable computational cost. Thus, this is the thickness we choose for these layers. Obviously, this is an artificial model which does not actually simulate the physics behind the establishment of interfacial thermal resistances. Indeed, this would require a precise description of the phonon-phonon and phonon-electron scattering, which is beyond the scope of the commercial codes solving the heat transport equation. However, on a more effective point of view, our aim is to simulate the insulatory boundary conditions well representing the effect of ITRs, by imposing a temperature jump at the ends of the PMMA layer and heat confinement inside the film. Knowing the thickness, these layers are characterized by a proper value of their bulk thermal conductivity, which in the end gives a realistic surface resistance value. Obviously, the situation at the tip/PMMA interface is substantially different than the one at the PMMA/substrate interface. The contact is much less effective at the former interface, meaning that heat flows more difficultly. For this reason, the value of the ITR per unit area at the tip/PMMA interface is larger than the one at the PMMA/substrate interface, however it is hard to estimate, because it is not a typical film-on-film situation. The large uncertainty on this value is compensated by the negligible contribution it has on the PTIR behavior on the thickness, since it concerns a small contact area, whereas the PMMA/substrate interface is much larger. Indeed, the PMMA/substrate ITR is the most relevant in determining the PTIR dependence on the film thickness.

In fig.2.15 (panels c and d), I report the PTIR dependence on the thickness obtained from a set of simulations, for each AFM probes, in which only the value of the tip/PMMA ITR is modified. From these graphs, we can see that the PTIR signal is not significantly changing its dependence on the thickness upon an increase of an order of magnitude in the resistance value. This demonstrates the negligible impact of this ITR. However, the main contribution of this resistance concerns the temperature distribution within the PMMA film. Indeed, thanks to the insulation provided by the ITR, the cold spot at the tip/sample contact, which was present in fig.2.11, disappears. This situation is well represented in the panels a and b of fig.2.15, where the ITRs at the PMMA ends have been employed. As we can see, the temperature increase is confined inside the PMMA film, with a jump in temperature at its interfaces. The boundary conditions are completed with the fixed temperature in the Si substrate and in the cantilever, same as in the previous section.

Quantitatively, the ITR value at the tip/PMMA interface is set to 10^{-6} $W^{-1}\,m^2\,K$, while at the PMMA/substrate interface we employ three different values: $5{\cdot}10^{-8}$, 10^{-7} and $2{\cdot}10^{-7}$ $W^{-1}\,m^2\,K$. The behavior of the PTIR signal with respect the PMMA thickness is reported in panels c (for the Au tip) and d (for the Pd tip) of fig.2.15. We can see that the Au probe still shows a superlinear trend, while the Si_3N_4 is slightly sublinear. Both tips show a trend closer to the experimental ones. This is the effect of the ITRs, which can be further understood by looking at what happens as we increase the value of the PMMA/substrate resistance: low-thickness signals benefit of a larger percentage growth than the high-thickness ones. Thus, for the Au tip, the trend becomes more and

more linear, and for the Pd tip, it becomes more and more sublinear, as we increase the resistance value.

For the Pd tip, we already have a good approximation of the experimental trend, however for the Au tip this is still not the case. In order to have a more precise and a better agreement with the experimental trends, we need to go beyond the steady-state approximation.

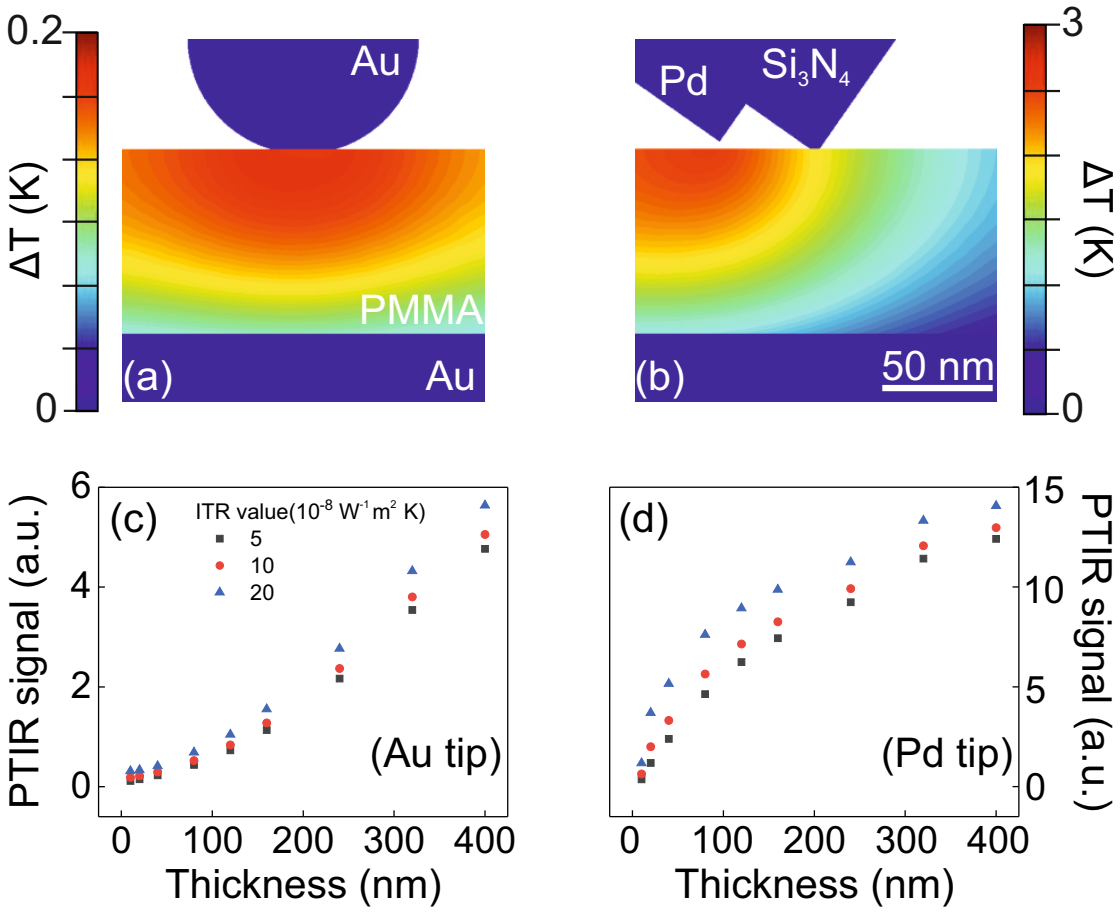

Figure 2.15: Panels a and b report the steady-state temperature distribution of a 80-nm-thick PMMA film, characterized by ITRs of 10^{-6} $W^{-1}\,m^2\,K$ at the tip/PMMA interface and $2{\cdot}10^{-7}$ $W^{-1}\,m^2\,K$ at the PMMA/substrate interface. For both the Au (a) and Pd (b) tip, the cold spot previously observed disappears, and the temperature increase is entirely confined in the PMMA film. In (c) and (d) the calculated PTIR signal as a function of the PMMA thickness. Here, the ITR at the PMMA/substrate interface has the values in the legend. The trend associated to the Au probe (c) bends towards a linear dependence, while the Pd tip (d) shows a sublinear behavior.

2.4.8 Dynamics of the thermalization

We perform a set of transient simulations to evaluate the thermalization dynamics of the sample as a function of its thickness. In this set, the thermal source (the optical absorption in the PMMA) is turned on for an unlimited amount of time, so that the sample reaches a steady-state situation, and suddenly is turned off. We collect the temporal decay of the maximum temperature inside the PMMA, for both tips and for all the values of the thickness reported in table 2.1.

At the end, we fit the temporal evolution with an exponential decay, extracting the characteristic time constant of the thermalization. In fig.2.16 the dependence of the time constant τ on the sample thickness is reported, for both tips (Au tip in panel a, Pd tip in panel b), when no ITR is employed (black points) and with ITRs at the two interfaces (red points). The value of the tip/PMMA ITR is 10^{-6} $W^{-1}\,m^2\,K$ and the value of the PMMA/substrate ITR is $2{\cdot}10^{-7}$ $W^{-1}\,m^2\,K$. From these graphs, we can observe:

- When the ITRs are employed the thermalization is slower than when there are no ITRs, meaning that the time constants with ITRs are always larger than the corresponding ones with no ITR. This is expected, because the ITRs insulate heat inside the PMMA and the heat flow faces their opposition when flowing through the interface. In the end, the cooling process is slower.

- The dependence of the time constant on the thickness is fitted with an allometric curve: $\tau = a \times z_0^b$, where τ is the time constant and z_0 the thickness. From the fit, we notice that the presence of the ITRs change the dependence of τ on z_0: for the Au tip, b changes from 2.28 (no ITR) to 1.9 (with ITR), while for Pd tip, it changes from 1.92 (no ITR) to 1.63 (with ITR). In both cases, the ITRs bend the behavior towards linearity. A similar observation was reported in the work of Chae *et al.* previously cited [2].

- Following the consideration above, it is important pointing out that the dynamics has a slightly different behavior for the two tips. This is due to the their diverse thermal properties, which govern the heat flow away from the sample, but also their optical confinement, which determines the width of the temperature hotspot.

- It is crucial to determine when the steady-state approximation is not valid anymore. The blue dotted line represents the pulse duration in the experiment: when τ is roughly above this line, the sample does not have enough time to reach the steady-state situation before the QCL is turned off, so the approximation is not valid anymore. For this reason, a more accurate model has to be taken into account.

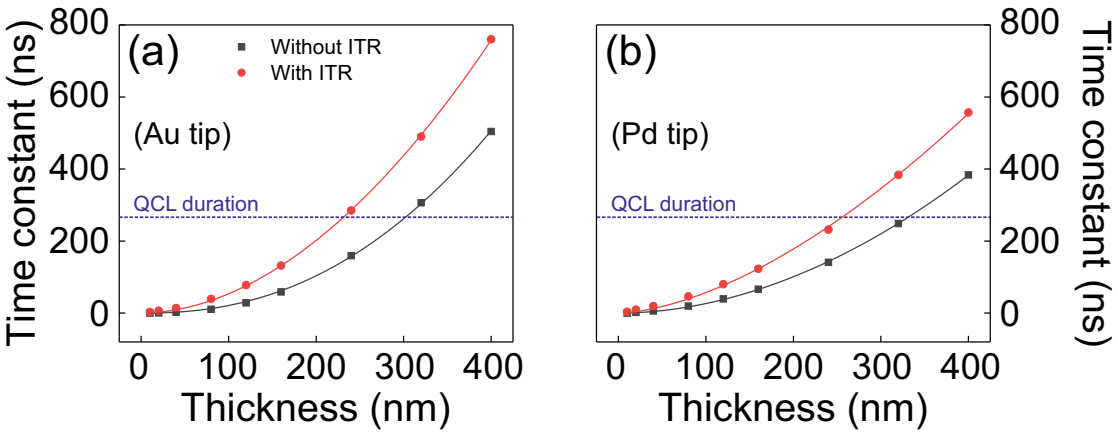

Figure 2.16: The dependence of the thermalization time constant on the PMMA thickness for the Au (a) and Pd (b) tip. The blue dotted line marks the duration of the QCL pulse: for any point roughly above that line, the steady-state approximation is not valid.

In fig.2.17 the thermal expansion of two PMMA thicknesses, 10 nm (panel a) and 320 nm (panel b), is reported, as a function of time. In these simulations, the thermal source is on for 260 ns, as the QCL in the experiment. In the graphs, the pink area highlights when the QCL is on. We can see that in panel a the sample rapidly reaches the steady-state condition, where the thermal expansion is constant with respect to time. Then, when the QCL is turned off, it rapidly goes to zero. On the other hand, the 320 nm film (panel b) does not reach the steady-state condition, because of its slow thermalization dynamics. Indeed, at 260 ns, the instant in which the QCL is turned off, the temperature inside the 320 nm film is still growing, meaning that it does not reach the steady-state value. On the other side, the decay in this case is much slower, giving a further considerable contribution to the PTIR signal.

This analysis confirms that the steady-state approximation is valid until a certain value of the thickness (roughly 100 nm), above this threshold the dynamics of the system must be taken into account.

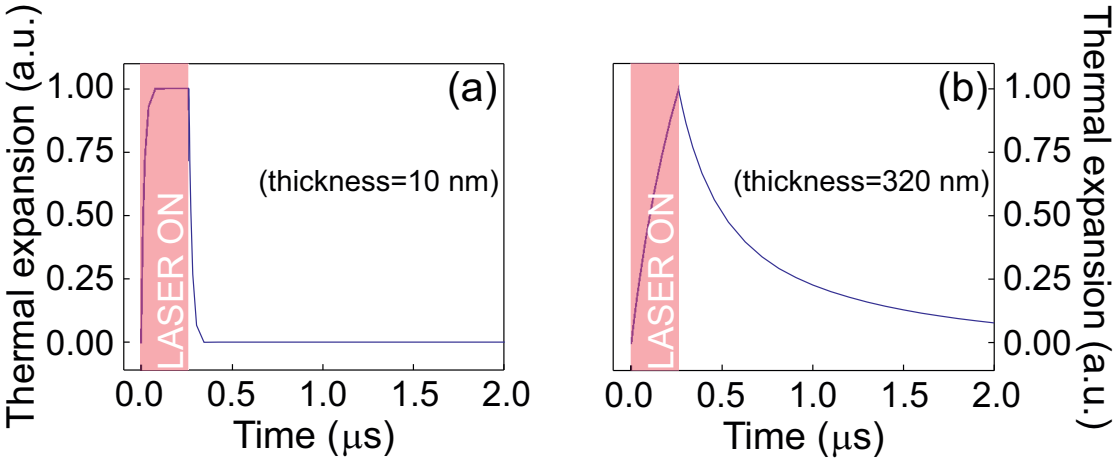

Figure 2.17: The thermal expansion as a function of time when the heat source is on for the same duration of a QCL pulse (pink area in the figure). In (a) the thickness of the film is 10 nm, in (b) it is 320 nm. The 10-nm film reaches the steady-state temperature during the QCL pulse (constant value of the thermal expansion), while the 320-nm one is too slow to reach it.

2.4.9 The complete model

Following the analysis of the previous section, we go beyond the steady-state approximation in our final model. Thus, we perform transient simulations collecting the temperature increase in the PMMA as a function of time for each PMMA thickness. The thermal environment is the same of section 2.4.7 and we investigate the same values of ITRs. The thermal expansion is calculated as in eq.2.4 for every instant in time, obtaining a behavior like the one depicted in fig.2.17. Since the experiment is performed in the REINS configuration, the QCL pulse is repeated with a frequency matching a cantilever bending mode: every 5.5 µs and 3.3 µs for the Au and Pd probe, respectively. The thermal expansion follows the QCL repetition rate. In the end, the periodic repetition of the thermal expansion force is the force felt by the AFM tip, driving its oscillatory motion: it represents the term $F_{\text{driving}}(t)$ in eq.2.2. The $F_{\text{driving}}(t)$ computed for the PMMA thickness $z_0 = 320$ nm for the Au tip and the associated cantilever oscillations are represented in fig.2.18. The PTIR signal is the asymptiotic value of the amplitude of this oscillation.

The differential equation describing the cantilever's oscillatory motion is numerically solved by employing a commercial solver [58]. The initial conditions, imposed at time $t = 0$ s, when the QCL is turned on for the first time, are of $z = 0$ and $z' = 0$, meaning the cantilever is still at the start. In fig.2.19 I report two plots, depicting the PTIR signal with respect to the PMMA thickness, for the two AFM probes. In panel a the trend associated to the Au tip becomes roughly linear, especially for high ITR values, whereas in panel b the behavior associated to the Pd probe becomes even more sublinear than before (section 2.4.7). The reason of this change is in the slow thermalization of the thicker films, which do not reach the steady-state temperature, forcing a smaller signal

on the tip. Thus, the trends flatten in the high-thickness regime. The trends showed in fig.2.19 represent a good approximation of the experimental data for both tips. The deviation from the results of the very first simulation set is due to two ingredients: the ITR and the thermalization dynamics.

This last consideration shows how these two physical ingredients are crucial in determining the PTIR signal, and, in general, in heat conduction at the nanoscale.

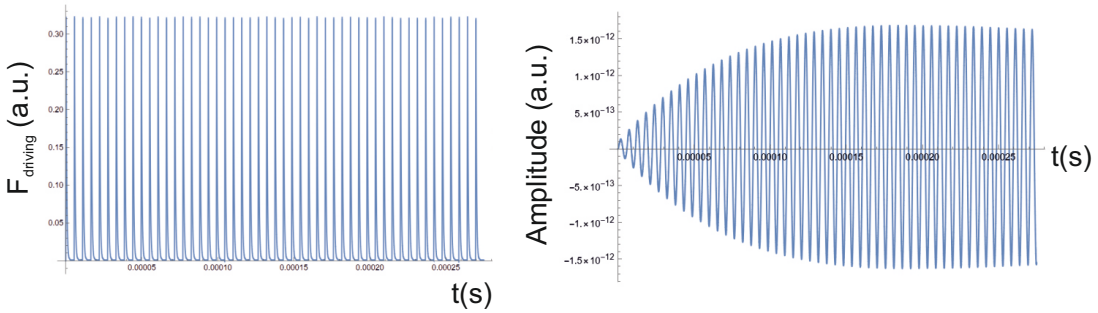

Figure 2.18: On the left, 50 repetitions of the thermal force, with a period $T = 1/f_{\mathrm{QCL}} = 5.5$ µs, driving the oscillation of the cantilever, which is represented on the right on the same time-scale.

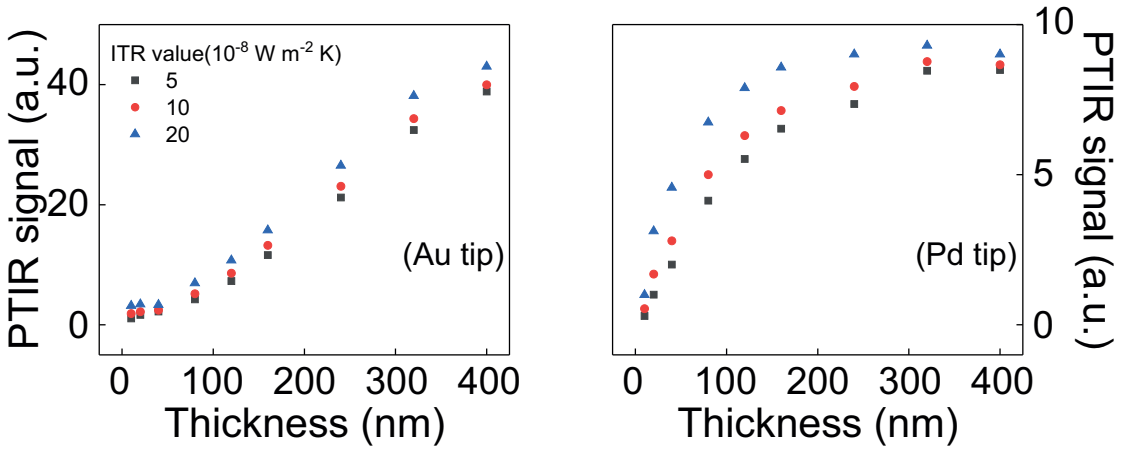

Figure 2.19: The trends obtained with the final model, which takes into account both the effects of ITRs and the thermal dynamics. The value of the ITR at the tip/PMMA interface is 10^{-6} $\mathrm{W^{-1}\,m^2\,K}$, while at the PMMA/substrate interface the ITR takes the values in the legend. The PTIR signal associated to the Au tip a shows a roughly linear dependence on the thickness, while the Pd trend b is sublinear. Both behaviors are in good agreement with the experimental data.

2.5 Conclusions and perspectives

In this work we developed a thorough and detailed model for the PTIR techinque. Starting from a solid experimental dataset, we accurately analyzed the physical ingredients having a major contribution in the determination of the PTIR signal. Studying the dependence of the PTIR signal on the sample thickness is also a relevant analysis enlighting the range of investigation of the technique. Moreover, by studying the properties of the resonant Pd tip, we can assess the effects of the AFM tip optical properties. Indeed, the optical confinement of the Pd tip allows to perform high-resolution and sensitive measurements, making it an excellent choice to study low-thickness samples, which typically give small signals, and superficial effects: both constraints often interest biological studies, so a tip with properly tailored optical properties can be beneficial.

In summary, our modelling led us to a set of conclusions:

- With optical simulations, we were able to assess the field distribution and the power abosorbed in the sample. We used this data to understand the fundamental difference in behavior of the two tips, which comes mainly from their optical properties.

- From steady-state thermal simulations we were able to retrieve the temperature distribution in the film. The first set of simulations produced two trends on the PMMA thickness which were not in agreement with the experimental data (superlinear for the Au tip, roughly linear for the Pd tip). We understood that we needed to model properly heat conduction at the interfaces.

- The role of the ITRs was analyzed in detail, both analtically and numerically. We developed a 1D model to single out the effect of the resistance boundary conditions in the heating of the film. ITRs were then modelled in the numerical simulations and we retireved more meaningful maps of the temperature distribution in the PMMA.

- The analysis of the thermal dynamics provided insight on the validity of the steady-state approximation, giving an estimate of the thermalisation times for the thicknesses considered. Moreover, it provided insight on the effect of ITRs on the thermal dynamics.

- The final model employed ITR boundary conditions and transient thermal simulations, the key ingredients in our modelling. In the end, we obtained a simulated dataset in satisfying accordance with the experimental measurements.

- In order to further improve the model, the thermal expansion should be simulated in the two dimensions of the sample surface, which was neglected in this work. Indeed, we applied a 1D model of elastic expansion.

- The thermalization dynamics could play an important role also in low-thickness samples, depending on their material properties. In particular, materials with high

mass density, high specific heat or low thermal conductance are associated with longer thermal dynamics.

The aim of this work was to provide a solid theoretical background to the modelling of the PTIR technique. The comparison with the experimental data reported at the beginnning of this chapter is crucial to benchmark the model we propose. By reaching a good agreement with the experimental data, we confirm that the model is solid. Indeed, we employed the same approach in two other collaborations with Sapienza University.

The first work, by Giliberti *et al.*, studies the conformal changes induced by light in patches of bacteriorhodopsin, a photosensitive protein [3]. The set-up exploits the plasmonic nanocavity between the Au tip and Au substrate described in this chapter, to enhance the field in the protein patches (with a thickness around 10 nm). In this case, it was important to have an estimate of the field inside the patches and the temperature increase when illumination targeted an absorption line of the proteins. For the last point, an accurate thermal model was needed. The results are reported in fig.2.20. In the temperature distribution (panel g) we can see that there is no cold spot under the Au tip: this is because an ITR was employed.

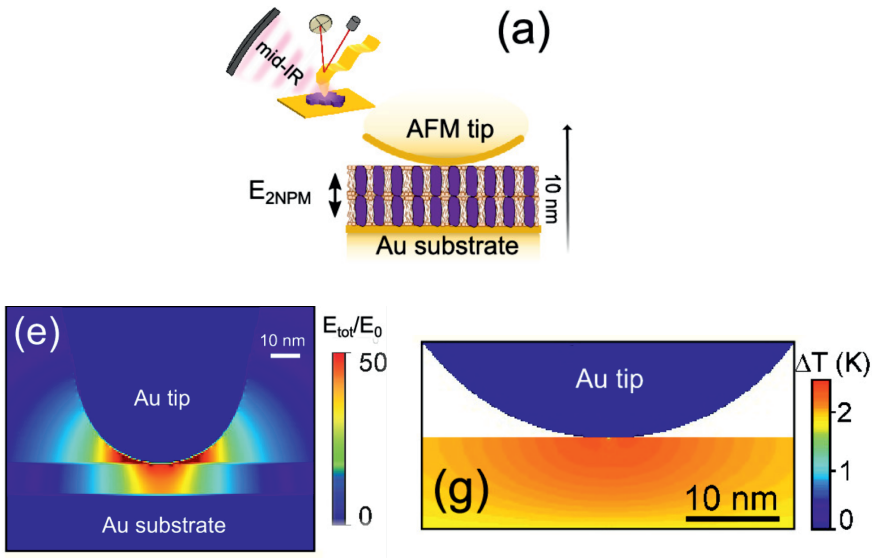

Figure 2.20: In (a), a depiction of the Au tip investigating the protein patches, over the Au substrate. In (e), the field distribution near the tip is depicted. Panel g reports the temperature distribution when the illumination targets an absorption line at 1540 cm^{-1} of the protein. Adapted from ref. [3].

The second work exploits the sub-wavelength resolution of PTIR to characterize the field distribution of an integrated mid-infrared waveguide [48]. The waveguide edge is inserted into a block made by a polymer (SU8). So the light exiting the waveguide finishes in the IR-absorbant polymer, which has a thermal expansion dependent on the

modal field profile of the waveguide. This thermal expansion can be detected by a PTIR measurement, overcoming the diffraction limit. Two PTIR maps are compared: the first is obtained with direct illumination of the SU8 with the QCL and the second with the QCL coupled to the waveguide. By looking at the two maps, one can compare the absorption profile coming from direct illumination with the one coming from the waveguide illumination. This comparison is reported in fig.2.21 (panels b and c). We employed our optical and thermal model to produce the simulated maps corresponding to this PTIR measurement (2.21, panels e and f) and numerically characterize the waveguide mode.

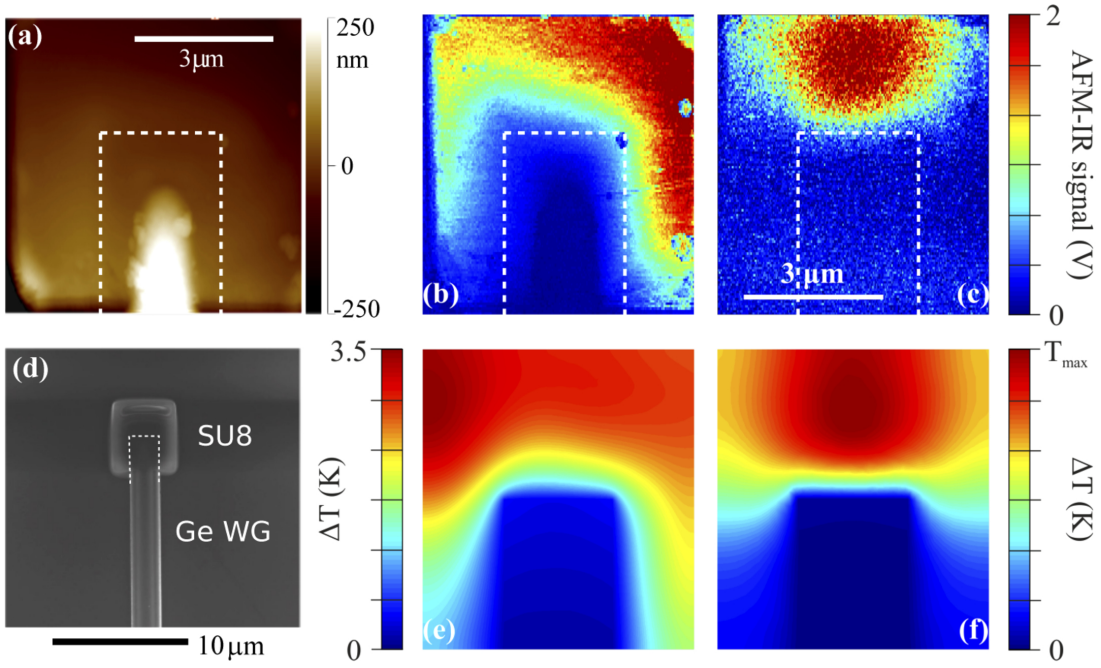

Figure 2.21: In (a), the AFM topography map of the waveguide. In (b), the PTIR map of the SU8 under direct illumination of the QCL ($\lambda = 6.6$ µm, in (c) the QCL is coupled with the waveguide. In (d), a SEM image of the waveguide. In (e) and (f) the simulated temperature maps correspondent to (b) and (c), respectively. The waveguide is marked by the white dashed line.

Chapter 3

Mid-infrared dielectric antennas on ENZ substrates

Abstract Nanoantennas have played a key role in near-field optics in the last twenty years. Indeed, their ability to enhance the electric and magnetic fields in confined hotspots is crucial for optical control at the nanoscale, making nanoantennas ideal building blocks for platforms working in the macro-fields of information processing, nonlinear optics, opto-electronics and molecular biosensing. We will focus on this point, in particular on the capability of the nanoantennas to enhance the signals coming from molecules. The standard for nanoantennas is represented by plasmonic resonators, however there are intrinsic limitations in the use of metals, mainly a troublesome extention to large-scale production. On the other hand, an alternative to plasmonic antennas has been proposed. In the last decade dielectric antennas have been proved to cover the functionalities granted by the plasmonic ones, especially in the visible and near-infrared. Indeed, dielectric antennas are typically made of undoped semiconductors, showing a large refractive index which grants optical confinement and strong resonances. In adherence with the leitmotiv of the thesis, this work focuses on the mid-infrared spectral range, so that the technology we aim to develop can benefit from the advantages of working in this range, from telecommunications to biosensing. However, the extention of dielectric resonances to the mid-infrared range is difficult. In fact, the typical process used to fabricate high-quality dielectric antennas is the epitaxial growth of crystalline semiconductors, which gives better structures than the plasmonic ones at the cost of employing similar materials for the antennas and the substrate. In VIS and NIR spectral ranges, dielectric antennas are often realized on transparent glass substrates, renouncing to the structural qualities coming from epitaxial growth, in order to have a strong index mismatch. However, in the MIR this is not possible, for the phonon absorption often presented by glasses. Thus, the employment of epitaxially growth semiconductors is needed, which suffer from similar refractive indexes of the materials employed. This condition limits optical confinement, blocking the establishment of significant resonances. The core of the following chapter is the solution that we propose to overcome this problem. As substrate, we employ a layer of a heavily doped semiconductor ($\sim 10^{19}$

cm^{-3}), showing a zero-crossing in the permittivity in the MIR (the so-called epsilon-near-zero condition). In this way, we obtain the largest possible index jump between the antennas and the substrate, saving the resonances. Also, we keep the possibility to manifacture the platfrom through an epitaxial process, preserving its structural qualities. In the end, we will give one of the first demonstrations of a platform showing dielectric resonances in the MIR, which can be exploited to sense vibrational signals coming from a small quantity of molecules. Moreover, the use of dielectric antennas allows us to exploit magnetic resonances, which are typically weak in plasmonic antennas, thus enabling the extension of specific applications to the MIR, e.g. the detection of chiroptical signals. The chapter will describe all the steps leading to the realization of the platform. First, a theroetical introduction on the physics into play is given. This is followed by a discussion on the typical substrates used for antennas in the MIR, leading to the chioce of an epsilon-near-zero material in our case. Having presented the general idea, the manifacturing process is described: from the design, to the growth and the fabrication. Then, the characterization of the platform is given, demonstrating the presence of a dielectric antenna resonance in the MIR. In the end, a first measurement of enhanced vibrational sensing is reported. As a perspective, the extention to chiral sensing is explained, by presenting the design of a suitable platform based on the same concept. This work was done in a collaboration between Politecnico di Milano and the Institut d'Électronique et des Systèmes in Montpellier, also during a 6-months exchange period I spent in Montpellier.

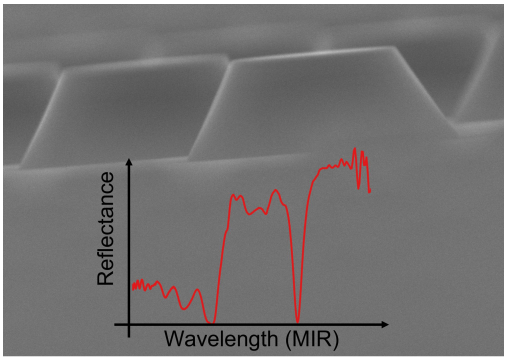

Figure 3.1: SEM side view of the final platform, composed by an array of dielectric pillars on top of a heavily-doped semiconductor layer. In the inset, a pictorial MIR reflectance spectrum of the platform. The first dip represents the resonance we designed.

3.1 Nanoantennas in the MIR

3.1.1 Advantages of nanoantennas

The development of antennas working at optical frequencies is a crucial milestone for near-field physics [37, 60–62]. In fact, their capability to control and confine light on the nanoscale is a major point of interest for nanotechnologies. For this reason, in the last two decades, nanoantennas have been employed in a vast and rich range of applications, such as nonlinear optics [63–65], information processing [66], ultrasensitive biodetection [67] and surface-enhanced spectroscopy [4, 68, 69]. Concerning the last two examples, it is worth noting the role of nanoantenna in improving the coupling between light and matter. Indeed, this enhancement enables the freedom to scale down the volume of the sample and the recovery of meaningful signals coming from a small quantity of molecules, which is often required in real-life situations, such as quality-control or the detection of pathogenic substances. In particular:

- The e.m. hotspots associated to the antenna resonances enhance the signal coming from molecules close to the antennas, granting large sensitivity.
- The tunability of their resonances allows one to properly design a sensor working in the desired spectral range.
- Since the sensor has a resonant behavior, we can perform selective detection of molecular features spectrally overlapping with the antenna resonance.

As already discussed in the introduction of this thesis, the infrared range contains crucial and distinctive information about molecules, since it is the range where molecular vibrations fall. In this spectral region the advantages of the employment of nanoantennas become even more prominent, allowing to overcome the poor IR light-molecule coupling. The weak coupling is due to a strong mismatch between the wavelength of the radiation, on the order of 10 µm, and the typical dimensions of molecules, between 1 and 10 nm. However, nanoantennas have the capability to confine light beyond the diffraction limit, creating hotspots with a characteristic dimension more similar to the one of molecules. So, the field confinement plays a crucial role in establishing an easier communication between IR light and matter. Benefiting also from the great sensitivity and tunability of their resonances, nanoantennas reveal themselves as an ideal building-block for the detection of amounts of hundreds, or even less, molecules. Indeed, in the last two decades, nanoantennas have been widely employed in biosensing, with many demonstrations of their capability to improve molecular detection [4, 6, 9]. In the end, starting from nanoantenna resonances, one can design a sensor improving the recognition of a particular chemical compound, targeting specific vibrational absorption lines, which represent the fingerprint of the sample (fig. 3.2).

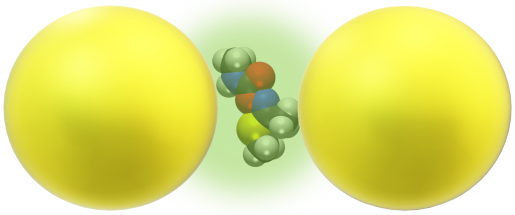

Figure 3.2: Representative depiction of a molecule-nanoantenna interaction: the molecular signals are enhanced in the electromagnetic hotspots close to the resonator.

3.1.2 Plasmonic and dielectric antennas

Metals have been the standard material of choice to fabricate nanoantennas, since their first demonstrations. Heavily-doped semiconductors, with metal-like behavior, have been recentely proposed as a valid alternative for metals [60, 70–72]. In both cases, the resonances take the form of Localized Surface Plasmon Resonances (LSPRs) (explained in detail in chapter 2), in which the free electrons of the metal are excited in collective oscillations on the surface [37, 73].

In the last decade, plasmonic antennas have been challenged by dielectric antennas. These antennas are typically made of heavily-doped semiconductors [61, 62] and their resonances arise from the displacement of bound electrons. Both plamonic and dielectric resonances are explained with Mie theory.

The comparison between these two approaches revolves especially around these points:

- Plasmonic and dielectric antennas show similar high-field enhancement, as predicted by Mie theory.
- The use of metals makes plasmonic antennas difficult to integrate on a large-scale production, since they typically employed metals (Au and Ag) are expensive and not foundry-compatible. However, recentely cheap and foundry-compatible materials (such as Al) have been succesfully proposed to fabricate plasmonic nanoantennas [69]. On the other hand, semiconductors are employed in large-scale global production processes, giving a strong background knowledge on the fabrication and the processing of these materials.
- Plasmonic antennas typically show weak magnetic resonances, as demonstrated by Finazzi *et al.* in 2015 [29]. Contrarily, in dielectric antennas strong magnetic resonances have been reported [5]. This is the main point of the comparison. As already reported, a platform sustaining magnetic resonances is eligible to enhance chiroptical sensing: this is one of our final perspectives.

Plasmonic antennas have been widely employed for sensing applications in the last two decades. One of the first examples of a gold nanoantenna enhancing molecular signals is reported in fig. 3.3. In this work, from Neubrech *et al.* in 2008 [4], the antenna is designed to have a resonance in the MIR, overlapping with the spectral features of octadecanthiol [$CH_3(CH_2)_{16}CH_2SH$]. The molecules are adsorbed on the resonators. The sensor capability to detect molecular absorptions is investigated with IR spectroscopy, by exciting the antennas with a synchrotron light and collecting their reflectance spectra.

The resonance is excited only when the polarization of the light is parallel to the long axis of the antennas. Thus, with a polarization perpendicular to the long axis of the antennas, the only spectral contribution is given by the adsorbed molecules. This is a way to check the bare signal of the molecules. The result of this measurement is represented by the red curve in fig. 3.3, showing no distinguishable signals. So, the number of molecules deposited on the antennas is too low to detect their direct absorption. On the other hand, when the plasmonic resonance is excited (black curve), we can see two sharp and evident peaks around 2800 cm^{-1}, corresponding to molecular absorption, superimposing on the broad dip, caused by the antenna resonance. This is a clear demonstration of the enhancement coming from the employment of nanoantennas, with which a very small quantity of molecules can be detected.

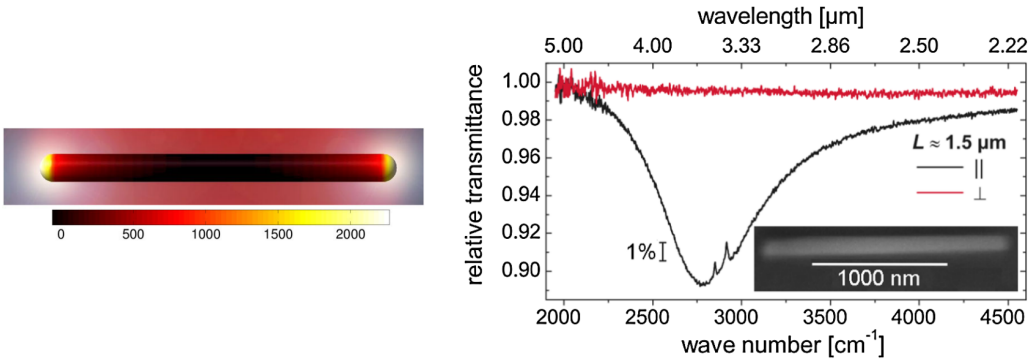

Figure 3.3: On the left, the simulated field enhancement of the antenna at resonance. On the right, the measured reflectance spectra: in red, the spectrum of the bare molecules, while in black the spectrum of the antennas with the molecules. The sharp peaks superimposed on the broad plasmonic dip represent the molecular signal enhanced by the antennas. In the inset, an SEM image of the Au antenna. Adapted from ref. [4].

Dielectric antennas have been exploited in sensing applications, too. However, they are typically used, mainly in the visible and NIR, for refractometric sensing, meaning that they investigate the refractive index of molecules, instead of probing their resonant absorption. One of the reasons behind this choice is the difficult extension of dielectric resonances to the MIR, where molecular absorption lines fall. Indeed, dielectric antennas are more often used in the visible or near infrared range. The causes and a possible

solution to the problem of extending dielectric resonances in the MIR will be investigated thoroughly in the next paragraphs.

Yavas *et al.*, in 2019, reported a refractometric sensor formed by dielectric pillars working in the NIR [5]. In this case, the interest in dielectric resonators is motivated by the possibility to exploit strong magnetic resonances. The sensor is used to detect a certain concentration of glucose solutions in water, while the individual effects of the electric and magnetic dipole resonances are investigated. In fig. the sensing results are reported. The plot represents the extinction of the pillars, covered by glucose solutions with increasing concentration. As the concentration increases, the refractive index of the solution increases. We see two effects: the extinction lowers and the peak redshifts, which are due to the compartecipation of the electric and magnetic dipole resonances of the antennas. This example shows the potential of dielectric antennas in sensing applications, here in the NIR range. In order to extend this approach to probe the resonant absorption of molecules, and not just their refractive index, we have to extend their working range to the MIR.

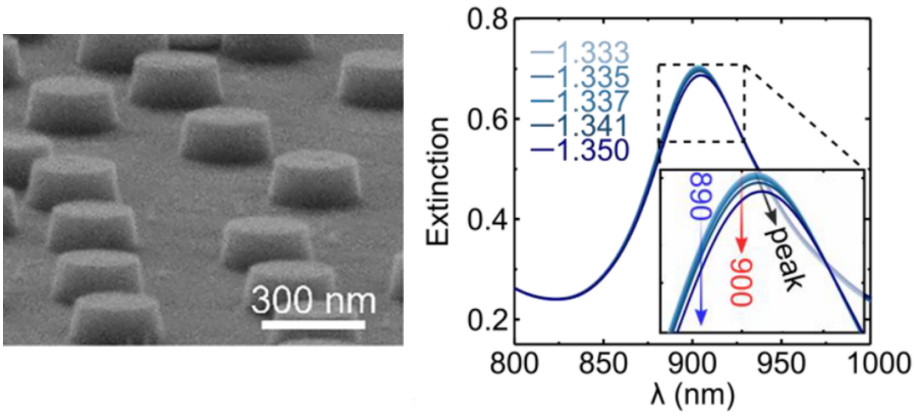

Figure 3.4: On the left, an SEM image of the dielectric resonators. On the right, the extinction spectra of the antennas in glucose solutions: by increasing the concentration, the peak red-shifts and lowers. Adapted from ref. [5].

3.1.3 Lattice resonances

By arranging nanoantennas in an ordered manner, we can make them communicate between each other. The bridge which connects the antennas is the scattered light. In fact, if we consider a matrix of antennas, every single one of them can scatter light in the plane of the matrix, and this diffracted light couples with the local resonance of the other antennas, creating a means of communication between the elements of the lattice [74]. As previously discussed, light scattering from nanoantennas is resonantly enhanced, making it an effective coupling mechanism on distances similar to the illumination wavelength.

The effect of these resonances, known as lattice resonances, is to drastically sharpen the linewidth and improve the field enhancement associated to the local resonances [75, 76].

Platforms exploiting lattice resonances have been already demonstrated for biosensing [77, 78], photocatalysis [79], electrochemistry [80], magneto-optics [81], flourescence [82] and vibrational spectroscopy [83, 84]. In particular, for the latter, the higher field enhancement increases the sensitivity of the platform, while the sharper resonances have a linewidth often comparable with the molecular absorption lines. Let us discuss the physical origin of these resonances. The theoretical basis for this discussion is the coupled dipole (CD) approximation [74, 85, 86]. The analysis focuses on the diffractional behavior of an array of N particles, which are modelled as electric dipoles. We call $\mathbf{r}_i$ the position of the i^{th} element of the array and α_i its polarizability. This is a many-body problem, in which every element is influenced by the other N-1 ones. In order to understand the optical response of the particles, we have to evaluate how they affect each other. In other terms, we need to find the induced dipole of each nanoantenna. Indeed, the induced dipole of the i^{th} element is expressed as the polarization vector $\mathbf{P}_i = \alpha_i \mathbf{E}_{loc,i}$, where $\mathbf{E}_{\mathrm{loc},i}$ is the total field acting on the i^{th}, expressed as the sum of two terms:

$$\mathbf{E}_{\mathrm{loc},i} = \mathbf{E}_{\mathrm{inc},i} + \mathbf{E}_{\mathrm{dipole},i} \tag{3.1}$$

where $\mathbf{E}_{\mathrm{inc},i}$ represents the external incident field, while $\mathbf{E}_{\mathrm{dipole},i}$ is the retarded contribution coming from all the other nanoparticles. For a fixed wavelength λ, we can write:

$$\mathbf{E}_{\mathrm{inc},i} = \mathbf{E}_0 \mathrm{e}^{i\mathbf{k}\cdot\mathbf{r}_i} \tag{3.2}$$

$$\mathbf{E}_{\mathrm{dipole},i} = -\sum_{\substack{j=1 \\ j\neq i}}^{N} A_{ij}\mathbf{P}_j \qquad i = 1, 2, ..., N \tag{3.3}$$

where E_0 is the amplitude of the external field, $k = 2\pi/\lambda$ its wavevector and $\mathbf{A}$ is the matrix weighting the interaction between the dipoles. The scalar product in the $\mathbf{E}_{\mathrm{dipole},i}$ expression becomes:

$$A_{ij}\mathbf{P}_j = k^2 \mathrm{e}^{ikd_{ij}} \frac{(\mathbf{d}_{ij} \times (\mathbf{d}_{ij} \times \mathbf{P}_j)}{d_{ij}^3} + \mathrm{e}^{ikd_{ij}}(1 - kd_{ij}) \frac{(d_{ij}^2 \mathbf{P}_j - 3\mathbf{d}_{ij}(\mathbf{d}_{ij} \cdot \mathbf{P}_j)}{d_{ij}^5} \qquad j \neq i \tag{3.4}$$

where d_{ij} is the vector connecting the i^{th} to the j^{th} element. Now we have all the ingredients to calculate the induced dipole, which will be the solution of:

$$A_{ij} \cdot \mathbf{P}_i = \mathbf{E}_j \tag{3.5}$$

This set of equations can be solved analytically in the case of infinite and identical antennas, each with a polarizability α_{s}. In this case, we can write the polarization P and the extinction cross-section C_{ext} for an element of the array as:

$$P = \frac{E_0}{1/\alpha_{\mathrm{s}} - S}; \qquad C_{\mathrm{ext}} = 4\pi k N \mathrm{Im}(\frac{P}{E_0}) \tag{3.6}$$

where S is the dipole sum. This term weights the presence of the other antennas in the definition of the polarization. Without S, we retrieve the situation of the isolated particle. At normal incidence, with respect to the array plane, S can expressed as:

$$S = \sum_{j \neq i}^{N} \frac{(1 - kd_{ij})(3\cos^2\theta_{ij} - 1)\mathrm{e}^{ikd_{ij}}}{d_{ij}^3} + \frac{k^2 \sin^2\theta_{ij}\mathrm{e}^{ikd_{ij}}}{d_{ij}} \tag{3.7}$$

where θ_{ij} is the angle formed by $\mathbf{d}_{ij}$ and the polarization of the incident light. S is the crucial term in the definition of the lattice resonances. Indeed, in the expression of P reported in 3.6 the real part of the denominator goes to 0 when $\mathrm{Re}(1/\alpha_\mathrm{s})$ (which is related just to the properties of the single antenna) is equal to $\mathrm{Re}(S)$. This condition defines the establishment of a resonance, whose origin resides in the collective behavior of the coupled dipoles. So, the real part of S is associated with the definition and the spectral position of the lattice resonance. The expression of S is valid when the lattice mode travels coupled in air. If the antennas couple through a substrate, we have to consider its refractive index, which shifts the resonance spectral position following the formula: $\lambda_\mathrm{substrate} = \frac{\lambda_\mathrm{air}}{n_\mathrm{substrate}}$ ($\lambda_\mathrm{substrate}$ is the wavelength of the lattice resonance in a substrate of index $n_\mathrm{substrate}$, while λ_air is in air).

The linewidth of the collective resonance is defined by the difference between $\mathrm{Im}(1/\alpha_\mathrm{s})$ and $\mathrm{Im}(S)$. In the end, by properly tuning S we can control the spectral position and the linewidth of the lattice resonance. We can tweak it by acting on the array properties, mainly the periodicity of the antennas. Thus, S represents a further degree of freedom in the characterization of the optical response of the platform.

Adato *et al.*, in 2009, gave one of the first demonstration of a platform exploiting collective nanoantenna resonances to enhance vibrational signals [6]. In fig. 3.5 (on the left), the reflectance spectra of the arrays are plotted as a function of the distance between the antennas. The black curve represents the uncoupled antennas, which is a similar situation to the red curve, where the distance between the antennas is too large and the coupling is lost. However, for the other values of the pitch, tailored to excite the collective resonance, we see a net improvement in the resonance, which becomes sharper and more intense (the yellow curve above all). In the end, the employment of the collective resonance allows to detect a small quantity of molecules (145 per antenna) of a protein, silk fibroin, with a sensitivity an order of magnitude larger than the uncoupled antennas. This can be seen in the right part of fig. 3.5, where the differential reflectance, computed as the difference between signals from the clean sensor and the sensor with molecules, is reported. Here, we can see that the feature around 1660 cm^{-1}, arising from molecular absorption, is much more distinct in the platforms exciting the collective resonance (blue, yellow and green curves) with the respect the uncoupled antennas (black and red curves). This is a clear demonstration of the advantage of employing lattice resonances to improve the detection of molecular vibrations.

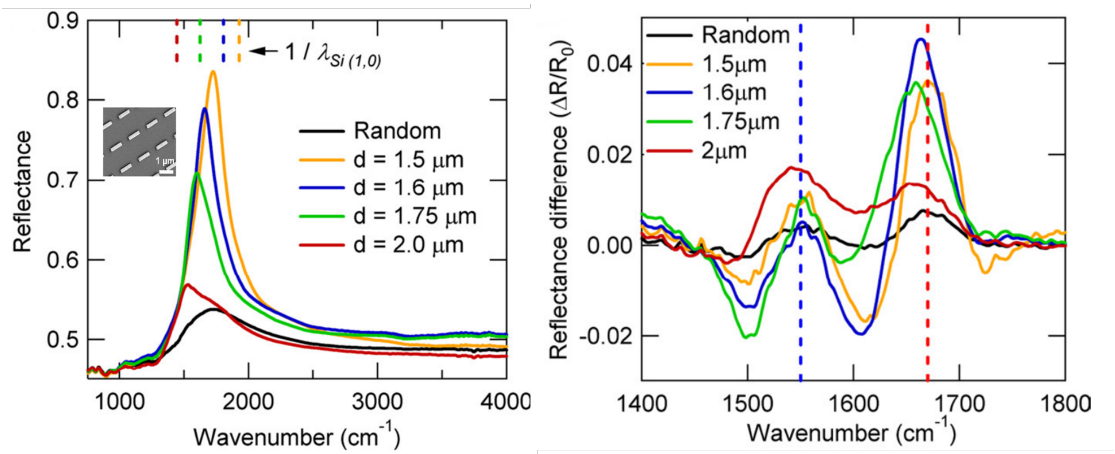

Figure 3.5: On the left, the reflectivity of the periodic array. The resonance is grately enhanced when the pitch of the antennas excites the collective resonance (green, blue and yellow curves). In the inset, the SEM top view of the antenna array. On the right, the differential signal arising from the comparison between the clean and the protein-coated sensor. The differential signal clearly benefits from the excitation of the lattice resonance (green, blue and yellow curves). Adapted from ref. [6].

Since our final goal is to improve the detection of molecular vibrations, it is convenient to exploit lattice resonances in the platform we want to create. This means that a proper design is needed, with the lattice resonance becoming one of the key ingredients in the establishment of a strong field enhancement close to the antennas. In other words, the periodicity of the antennas becomes a free parameter in the optimization of the near field enhancement, which defines the sensing capability of the platform we want to design. This ingredient can also be employed in designing platforms to create strong chiral response, as demonstrated by Mattioli *et al.* in 2020 [87].

3.2 The chioce of the substrate

3.2.1 Dielectric resonances in the MIR: a simple model

In order to understand and model dielectric resonances in the MIR, let us consider a simple model. The following analysis has been performed by employing the commercial software Ansys Lumerical FDTD. First, we can review the scattering properties of the free-standing dielectric antenna discussed in the subsection 1.9.1: a pillar-shaped antenna, with radius (r) and height (h), made of a lossless material, with refractive index $n_{\text{antenna}} = 3.5$, which is a typical value for undoped semiconductors in the MIR. With a proper set of geometrical parameters ($r = 3$ µm, $h = 1.6$ µm) we find a resonance in the scattering spectrum around 15 µm (fig.3.6). This corresponds to the electric dipole resonance, as discussed in section 1.9.1. We can appreciate the field enhancement corresponding to this resonance in fig. 3.7 (panel a).

This simulation was performed for a pillar in vacuum. However, in order to fabricate this antenna, we need a substrate to support it. Thus, we perform an analysis on the effects of the substrate, aiming to understand the best choice we can employ to preserve the field enhancement, meaning that we try to put a material with a given refractive index below the antenna, and study how the resonance is affected. The free-standing situation corresponds to a infinite substrate with a refractive index $n_{\text{substrate}} = 1$. So, first we try to increase this value to $n_{\text{substrate}} = 2$, keeping the substrate expanding indefinetely underneath the antenna. The red curve in fig. 3.6 represents the scattering spectrum in this situation: we see that the resonance redshifts and is less pronounced. The weaker confinement is confirmed by the electric field map in fig. 3.7 (panel b).

If we increase the index of the substrate to $n_{\text{substrate}} = 3$, which represents is closer to the index of the typical substrates (the refractive index of undoped semiconductors, like Si, InAs, GaAs, GaSb is typically around 3.5) used for semiconductor antennas in the MIR, we retrieve the scattering spectrum in fig. 3.6 (in blue). The resonance is not distinguishable in the spectrum in this case. Indeed, the field enhancement is much lower than in the free-standing situation (panel c of fig. 3.7). This analysis confirms that dielectric resonances suffer heavily from the absence of a strong index contrast between the antenna and the substrate. However, a small index contrast represents the typical situation for dielectric nanoantennas in the MIR. In fact, this represents the main limitation gatekeeping the dielectric resonances from extending to the MIR. So, in order to design high-quality dielectric nanoantennas, we have to find a way to integrate a strong index mismatch in an all-semiconductor platform.

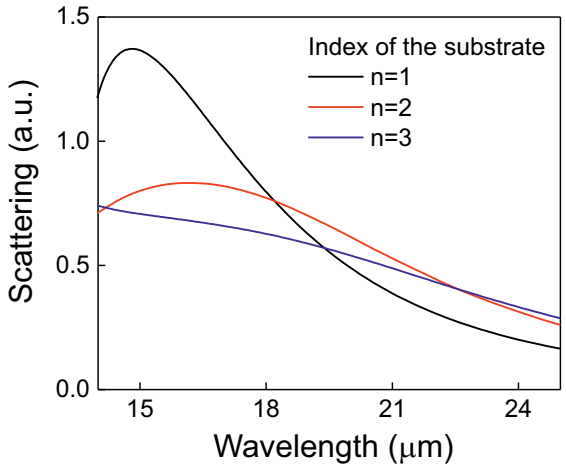

Figure 3.6: Evolution of the electric dipole scattering from a cylindrical dielectric antenna with $r = 3$ µm, $h = 1.6$ µm and $n = 3.5$, while varying the refractive index of the substrate. As the refractive index of the substrate increases the resonance becomes weaker.

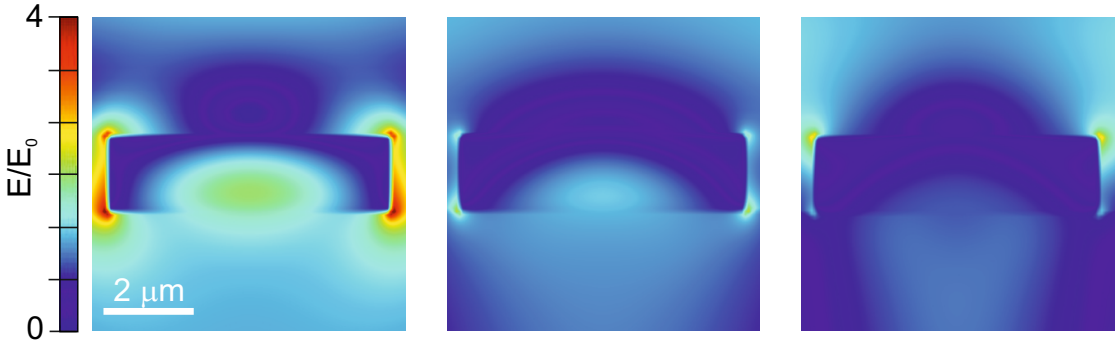

Figure 3.7: Electric field distribution close to the dielectric antenna at resonance, while varying the refractive index of the substrate. The colorbar is the same for the three images.

3.2.2 Substrates for nanoantennas working in the infrared

The choice of a proper substrate is a crucial and delicate point in the design of a platform exploiting nanoantenna resonances. Indeed, the choice of the substrate affects the structural and optical properties of the platform, so, in the end, it defines the quality of the resonances. In general, a good substrate should have these features:

- A strong index contrast with respect to the antennas, to grant field confinement and hence sustain the resonances. Since the metals and semiconductors used for plasmonic and dielectric nanoantennas in the MIR are high-index materials, the substrate should be a low-index material.
- Small absorption in the spectral range of interest, so that reflection or transmission measurements are possible and the quality factor of antenna resonances is not compromised.
- Compatibility with growth and fabrication processes which grant high structural quality of the antennas, i.e., for semiconductors, epitaxial growth.

In this paragraph, by looking into the literature, we will examine the traditional substrates used for nanoantennas working in the MIR, discussing their advantages and disadvantages. The end of this discussion is the choice of the most suitable substrate for the platform we intend to design. First, let us consider plasmonic nanoantennas. The work cited previously by Neubrech *et al.* exploits nanoantennas made of Au, deposited over a substrate of calcium fluoride (CaF_2) [4]. CaF_2 is one of the most common substrates for MIR plasmonic nanoantennas. It is a low-index material, however it suffers from strong absorption in the fingerprint region. In fig. 3.8 the refractive index and the absorption of CaF_2 are reported. Here, we can see that CaF_2 presents an absorption peak aroud 40 µm, originating from the excitation of a transverse optical mode of vibration. This strongly hinders antenna resonances, even at 10 µm. Moreover, the fabrication processes of nanoantennas related to the use of CaF_2 give typically low-quality structures, especially if the nanoantennas are made of semiconductors, since epitaxial growth

of single-crystalline semiconductors cannot be exploited. The use of CaF_2 also fights against foundry compatibility of semiconductors, compromising one of their advantages.

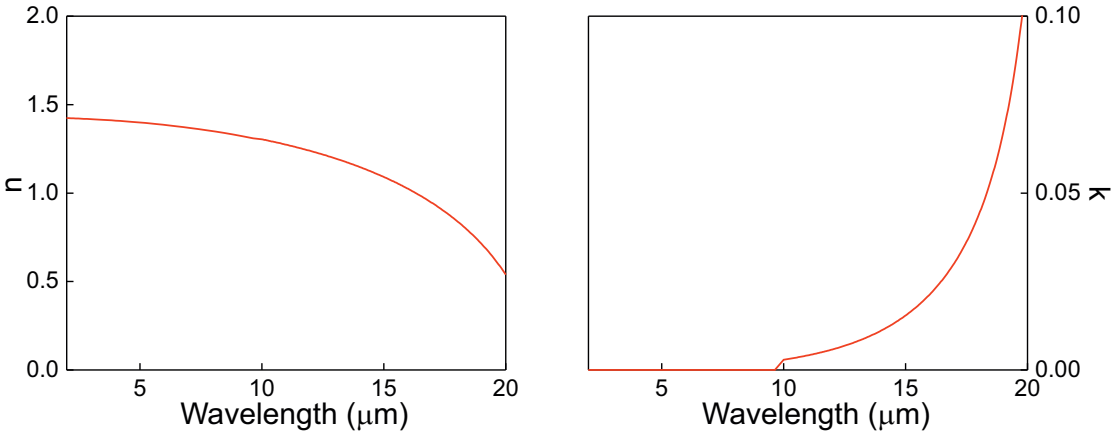

Figure 3.8: The refractive index and extinction coefficient of CaF_2 in the MIR, respectively in panel (a) and (b). CaF_2 shows a strong absorption peak around 40 µm, which has a considerable effect already in the fingerprint region. Taken from ref. [7, 8].

Other substrates have been proposed in semiconductor plasmonics, meaning for antennas made of semiconductors, doped at the point of having a metal-like behavior. The main advantage coming from this type of plasmonic antennas, instead of the more traditional metallic ones, is the possibility to build all-semiconductor platforms, employing an undoped semiconductor as substrate [60]. Indeed, an all-semiconductor platform can be grown via epitaxy, which allows for high-quality structures. Moreover, since the platform is only made of semiconductors, it can be exported on mass-scale production processes. However, employing undoped semiconductors (i.e., Si for group IV, GaAs or GaSb for groups III-V) as substrate, typically high-index materials in the MIR, means that we have to deal with a small index contrast between the antenna and the substrate. As already discussed, a small index contrast weakens field confinement. While this still represents a viable situation for plasmonic resonances, we have seen that dielectric resonances suffer greatly from a small index contrast.

Plasmonic resonances have indeed already been demonstrated in this kind of platform [70, 71]. Barho *et al.* realized arrays of highly-doped InAsSb antennas on a GaSb substrate enhancing the detection of molecular absorption lines in the MIR [9]. In fig. 3.9 we can see the InAsSb antennas enhancing the detection of vanillin (4-hydroxy-3-methoxybenzaldehyde), in a similar fashion of what done with Au antennas by Neubrech *et al.*.

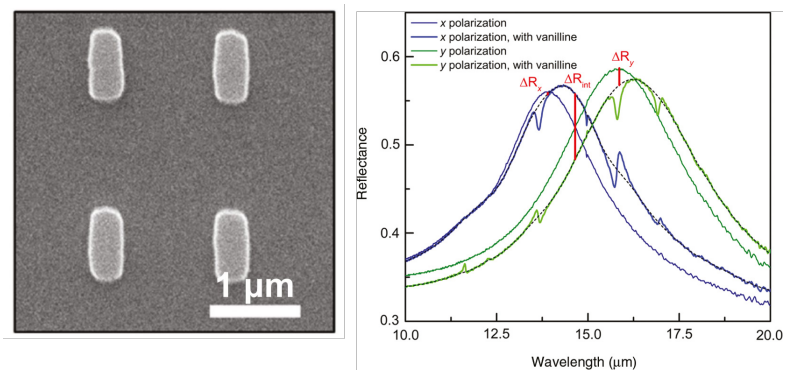

Figure 3.9: On the left, the SEM image of the InAsSb antennas. On the right, the reflectance spectra of the sensor coated by vanillin. The sharp lineshapes superimposed on the broad peak represent the vibrational signals enhanced by the antennas. Adapted from ref. [9].

For dielectric antennas, one common strategy is to employ silicon-on-insulator (SOI) technology, i.e. Si antennas over a silicon dioxide (SiO_2) substrate, especially in the visible and NIR [5, 88]. Moreover, let us look at the applicability of this technology in the MIR. In fig. 3.10 the refractive index and extinction coefficient of SiO_2 are reported (Refractiveindex). From these graphs, we can see that SiO_2 strongly absorbs in the fingerprint region (around 9 µm), where a Si-O-Si vibrational mode is excited. Similarly to CaF_2, this absorption is problematic, since it weakens the antenna resonances. For this reason, dielectric resonators based on SOI technology do not have a widely-employed extention to the MIR.

On the other hand, there are a few examples of resonators working in the MIR, but they typically rely on CaF_2 [89]. We have already discussed CaF_2 as a substrate for nanoantennas, and how its usage defeats the purpose of empoying semiconductor platforms.

Indeed, the scheme of all-crystalline semiconductor platforms is preferable, i.e., semiconductor antennas on top of a semiconductor substrate, in a similar fashion of what done in semiconductor plasmonics. In fact, this approach leads to the advantages cited above, i.e., high structural quality and foundry compatibility. Dielectric resonators exploiting an all-crystalline semiconductor platform have been demonstrated for the visible and near-infrared range [90]. However, their MIR establishment is hindered by the small index contrast between the antennas and the substrate. Indeed, the typical substrates (Si, InAs, GaAs) present high refractive indexes in the MIR, similar to the ones of the antennas. This is the problem we aim to solve. In this thesis, I will propose a possible approach to overcome this limit, keeping the advantages of an all-semiconductor, epitaxial and monolithic platform. This will be the main point of the next sections.

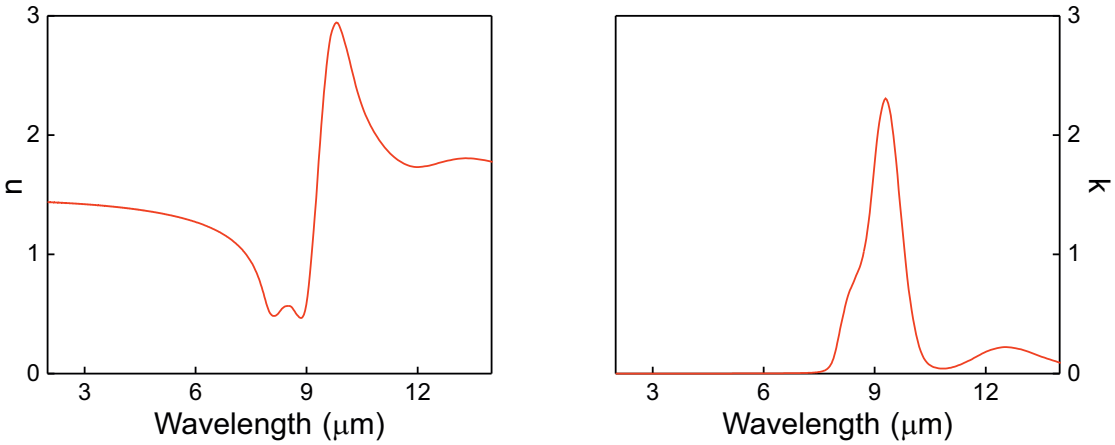

Figure 3.10: The refractive index (left panel) and extinction coefficient (right panel) of SiO_2, showing a high-index and strong absorption in the fingerprint region. Taken from ref. [10].

3.2.3 Epsilon-near-zero materials

The use of semiconductors for every element of the structure (antennas and substrate) carries the advantages of exploiting well-developed techniques for a high-quality growth process, i.e. epitaxial growth, and being compatible with mass-scale production. So, on the one hand an all-semiconductor platform is strongly appealing, on the other a strong index contrast between the antennas and the substrate is needed. This thesis proposes a solution satisfying both needs, by employing an epsilon-near-zero (ENZ) material [91]. The ENZ condition corresponds to a vanishing permittivity at a specified wavelength $\mathrm{Re}(\epsilon) \approx 0$. ENZ materials represent an emergent and promising technology in photonics. They are widely studied, because their defining condition gives rise to interesting effects when interacting with light [92, 93]:

- The refractive index can be written as: $n = \sqrt{\sqrt{\mathrm{Re}(\epsilon)^2 + \mathrm{Im}(\epsilon)^2} + \frac{\mathrm{Re}(\epsilon)}{2}}$ at optical frequencies. If the material presents low losses ($\mathrm{Im}(\epsilon) \approx 0$), the ENZ condition corresponds to a vanishing refractive index. As discussed in the previous section, a low refractive index is crucial for the substrate of the antennas we plan to design. Indeed, an ENZ substrate presents a small refractive index provided that the losses are relatively small.

- Since the effective wavelength of the light, passing through a medium, is expressed as: $\lambda_{\mathrm{eff}} = \lambda/n$, the wavelength diverges inside ENZ materials, leading to an almost flat phase profile in the medium.

- Considering the optical impedance: $Z = \mu/\epsilon$, where μ is the relative permeability of the material (for most media $\mu \approx 1$ at optical frequencies), we see that Z diverges as ϵ approaches 0. The high impedance opposes to light propagation, which does not penetrate in the material and is mainly reflected.

Thanks to these properties, ENZ materials have been proposed for many applications in photonics [94, 95], like enhanced optical nonlinearity [96], ultrafast optical switching [97], radiation control [98] and perfect absorbers [99]. In relation to nanoantennas, ENZ materials have been employed to control the wavelength of the resonances and to tailor their emission pattern [93]. Notably, the ENZ condition has a "pinning" effect on the local resonance of the antenna, meaning that it fixes its spectral position. This effect has been already discussed in the case of plasmonic antennas [100–102].

Now, let us take a look at the typical approaches which have been employed to realize materials showing an ENZ condition in the infrared. Transparent conducting oxides (TCOs), such as Ga or Al doped zinc oxide (Ga:ZnO, Al:ZnO or indium tin oxide, known as ITO), are natural ENZ materials in the NIR, however they suffer from optical phonon absorption in the MIR which compromises a possible antenna resonance. These substrates have been demonstrated for controlling the spectral position of LSPRs, their radiation patterns and phase profiles, mainly in the NIR [93].

Alternatively, this condition can be engineered to be brought in a desired spectral range in specific materials, as it has been already done with hyperbolic metamaterials (HMMs) and heavily doped semiconductors. HMMs are typically realized by alternating layers of metals and oxides. By properly tuning the thickness of the layers, one can bring the epsilon-near-zero condition to the visible range. A successful example of this approach has been given by Habib *et al.* in 2020 [100]. Here the ENZ substrate is realized with an Au and TiO_2 HMM, and its main contribution is the spectral pinning of the local resonance of the Au antennas on top of it. This means that even when changing the aspect ratio of the antennas, their resonance remains roughly at the same wavelength, because it is forced to stay there by the ENZ condition. However, the use of metals in HMMs is not compatible with the idea of an all-semiconductor platform.

Another approach is represented by injecting crystalline semiconductors with a proper carrier density and bring their epsilon-near-zero condition in the MIR. Indeed, undoped or slightly doped semiconductors typically show a zero-crossing in the permittivity in the far-infrared, however with heavy doping (10^{19} cm^{-3}) it can be brought in the fingerprint region (around 6 to 15 µm). In fig.3.11 we find the Drude model of the permittivity of InAs: the dependence of the epsilon-near-zero position on the doping is also shown. So, this solution gives a further degree of freedom, controlling the index contrast between the antennas and the substrates, and being also compatible with epitaxial growth, as desirable.

In the end, the general sketch of our platform will be as follows: dielectric antennas, made of an undoped semiconductor, on top of an ENZ layer upholding the resonances, made of a heavily doped semiconductor, which is deposited onto a substrate made of an undoped semiconductor. This model is also compatible with a monolithic realization, meaning that it can be realized keeping the same material for every layer, the only change would be in the doping of the single layers. In our case, the material of choice is InAs, since it is a standard and well-known material for ENZ technologies, with already many demonstrations in the field [103–105].

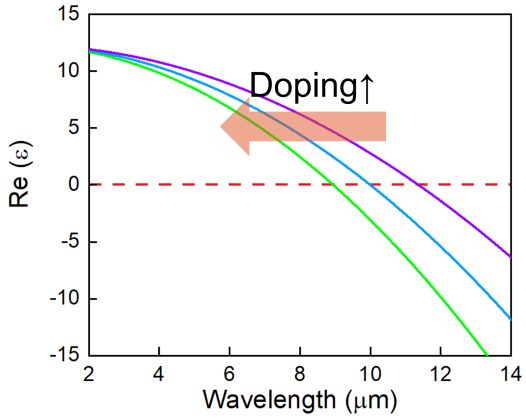

Figure 3.11: Drude model representing the real part of the permittivity of a heavily doped semiconductor. As the doping increases, the plasma frequency is brought at higher energies. With proper doping (10^{19} cm^{-3}) it reaches the MIR. The figure has been obtained with a value of $\epsilon_\infty = 12.3$ (typical value for doped InAs), and plasma frequencies increasing with the doping: 6.1×10^{14} rad s^{-1} (in purple), 6.6×10^{14} rad s^{-1} (in blue) and 7.3×10^{14} rad s^{-1} (in green).

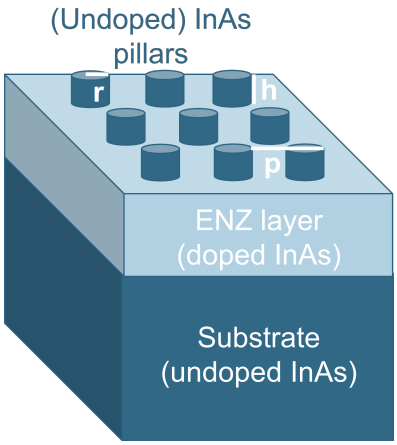

Figure 3.12: The sketch of the platform that we want to design: an array of undoped InAs antennas on top of a doped InAs layer. The permittivity of this layer is controlled by the doping, aiming to have a strong index contrast with the antennas and preserve their resonances. The platform is supported by a substrate made of undoped InAs. r, h and p are the radius, height and periodicity of the antennas.

3.3 Design of the platform

3.3.1 Modelling the ENZ layer

In order to implement the ENZ layer, we need a model linking the growth parameters to its optical properties. In order to do this, we employ an empirical formula relating the carrier density in the doped InAs layer with the ENZ wavelength: $N_c = 4.88 \times 10^{21} \lambda_p^{-2.7}$, where N_c is the carrier density in cm^{-3}, λ_p is the ENZ wavelength in µm. This formula was proposed by Taliercio *et al.* in 2014 (fig. 3.13) based on the observation of the so-called Brewster mode, explained in detail in section 3.4.2 [11]. So, upon deciding the proper ENZ wavelength for our platform, we can translate this parameter in growth requirement: the doping of the ENZ layer. Another important point is the thickness of the layers. The best solution is to have the thickest ENZ layer possible, which corresponds to the best field confinement in the antennas. However, we also have to consider the time and cost of the growth process. A good compromise would be an ENZ layer thicker than 2 µm.

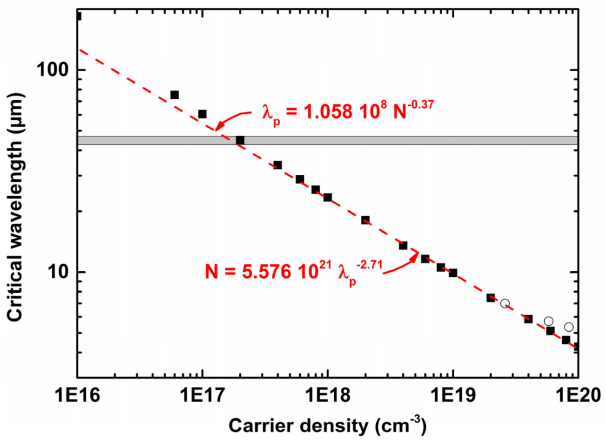

Figure 3.13: Dependence of the plasma wavelength of InAs on the doping. The scales are logarithmic. Adapted from ref. [11].

3.3.2 FDTD optimization

With the general sketch in mind, we optimize the structure. The optimization is performed with the FDTD method [23]. The aim of the optimization is to maximize the electric field enhancement close to the antennas in the vibrational range: we choose 10 µm of wavelength, which falls in the middle of the fingerprint region. We can easily find test molecules showing absorption lines around 10 µm, one of them being Perfluorooctyltrimethoxysilane (PFTMS), a silane extensively used in enhanced vibrational sensing test experiments [106]. The key ingredients of our modelling are the following:

- The local resonance of the antenna, in our case the electric dipole, the resonance showing the highest local field enhancement, which is tuned by changing the radius and height of the cylinders.
- The lattice resonance, so the coupling between antennas, which depends on the periodicity.
- The ENZ condition of the layer below the antennas, controlled by its doping.

These are free parameters fed to an the standard optimization procedure of the commercial software we use, which is based on the Particle Swarm Optimiazation (PSO). This kind of optimization has proven effective for electromagnetic problems, in particular nanophotonics. It is based on replicating the behavior of a swarm in exploring and finding the best solution: every particle explores independently but the information is shared. The range of the parameters is covered by the individual particles and at the end the swarm converges to the optimal solution.

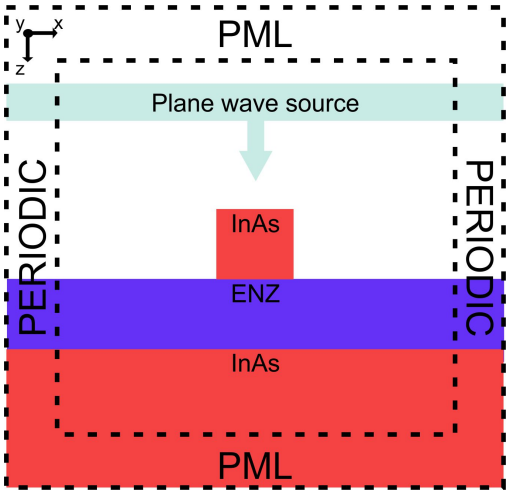

Figure 3.14: XZ section of the simulation environment. In x and y we impose periodic boundary conditions, to simulate an array of antennas. In z we impose Perfectly Matched Layer boundary conditions, extending indefinetely the air above and the InAs substrate below the antenna.

I report a depiction of the simulation environment in fig. 3.14. In the xy plane, in order to model the periodicity of the antennas we impose periodic boundary conditions in the xy plane, replicating a periodic matrix of infinite antennas, while in the z direction we impose the Perfectly Matched Layer (PML) boundary conditions, extending indefinitely the substrate below the platform and air above the platform. As for the optical properties, we have to model the permittivity of undoped InAs (antennas, substrate) and of heavily doped InAs (ENZ layer). We model InAs by fitting the data given by Adachi *et al.* (fig. 3.15) in the spectral range of interest, while the ENZ layer is described

with a Plasma model (in the commercial software we employ), so the permittivity will be defined as: $\epsilon(f) = \epsilon_\infty - \frac{\omega_p^2}{2\pi f(i\nu_c + 2\pi f)}$, where ϵ_∞ is the permittivity of InAs at high frequencies, the so-called epsilon infinity, ω_p is the plasma frequency of the ENZ layer, ν_c represents the losses and f is the frequency [12]. The pillars are illuminated from the air, by a plane wave propagating in the z-direction, linearly polarized along x, normal to the plane of the antennas. The spectral range of the simulation covers from 8 to 25 µm. We collect the reflectance spectrum in a plane monitor positioned above the platform. As previously discussed, we want to optimize the near field enhancement, so that the antenna is most sensitive to changes in the close environment, for example to the presence of a small number of molecules. To do this, we record the electric field at a point 200 nm distant from the cylinder, at its mid-height. This represents our figure of merit.

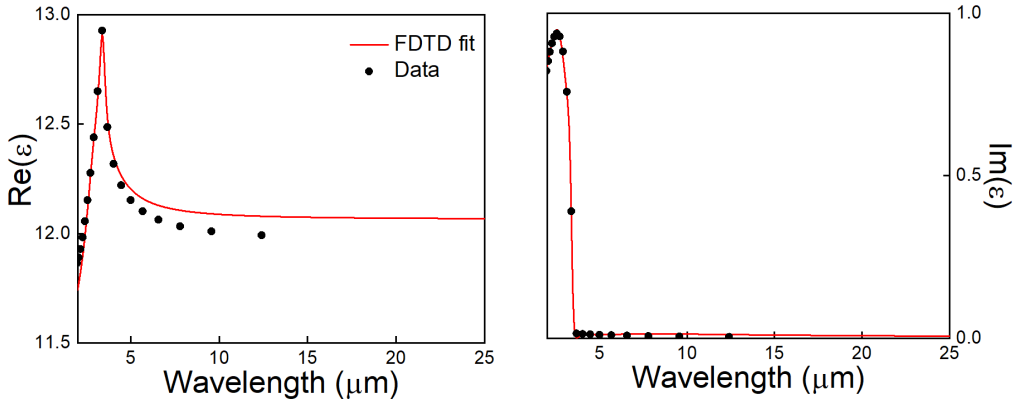

Figure 3.15: The real (left panel) and imaginary part (right panel) of the modelled InAs permittivity. Data from ref. [12]

The optimized structure has antennas with radius $r = 1.6$ µm, height $h = 1.6$ µm, periodicity $p = 10$ µm and ENZ wavelength $\lambda_{ENZ} = 10$ µm. The results of the optimization show that the antenna sustain the highest field enhancement when all three resonances are coincident. So, in our best solution, we have the electric dipole, the periodicity and the ENZ condition at 10 µm, which is the targeted wavelength.

In fig. 3.16, the reflectance spectrum of the pillars is reported on the left, in which we can see a sharp dip around 10 µm, which corresponds to the highest field enhancement in the spectrum, on the right. We notice other resonances at longer wavelengths, where the ENZ layer behaves like a metal. These resonances are plasmonic oscillations propagating along the surface of the ENZ layer, which are localized by the dielectric particles on top. For wavelengths shorter than 10 µm, the ENZ layer behaves like a dielectric material and we mainly see interference fringes. In fig. 3.17 the electric field distribution at 10 µm is reported. It is slightly different from the one of the isolated particles (section 1.9.1), showing stronger fields outside of the particle, but it still follows the typical dipolar

distribution. Moreover, the enhancement is much higher than in the single antenna, being higher than 200 for the optimized nanoantenna array, while it was around 16 for the isolatedd antenna. Both effects are due to the presence of the lattice resonance.

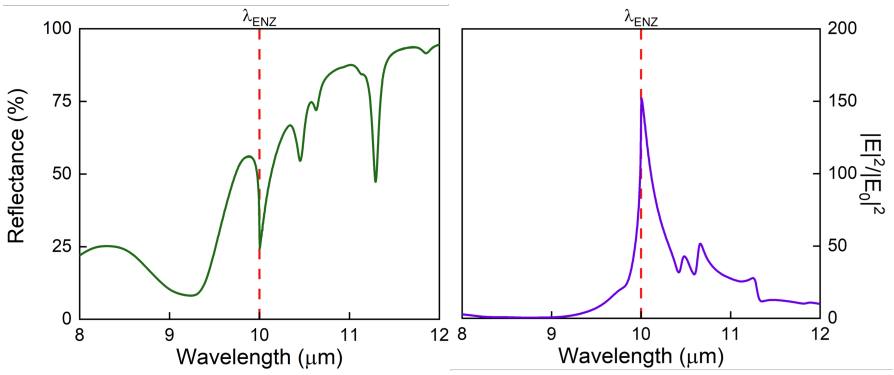

Figure 3.16: The reflectivity (left panel) and the near-field enhancement (right panel) spectra of the optimized platform. We see a dip in the reflectance at 10 µm, corresponding to the resonance we designed. At this wavelength, the platform shows the highest field-enhancement at mid-height.

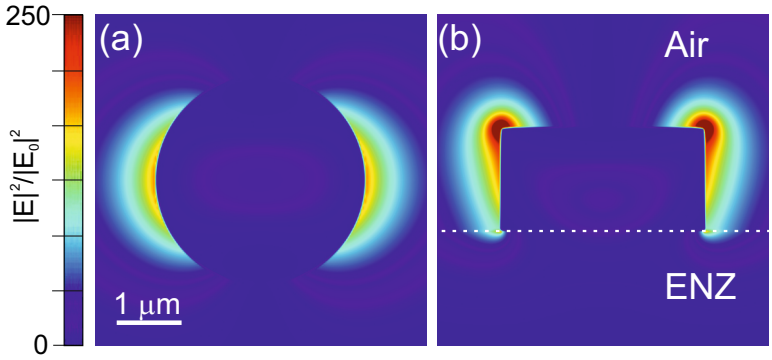

Figure 3.17: XY (panel a) and XZ (panel b) sections showing the field distribution close to the particle at 10 µm. The field is mainly confined outside the antenna, with the maximum at its upper veritices.

3.4 Realization of the platform

3.4.1 Brewster characterization

The growth of the platform was performed at the Institut d'Électronique et des Systèmes in Montpellier, by molecular-beam epitaxy (MBE), one of the most employed techniques for the epitaxial growth of semiconductors [107]. It employs thermally excited atomic

beams, which are launched on the substrate and when deposited, react to develop thin crystalline films. In this process, the doping of a material is precisely controlled by operating on the temperature of the atomic sources. Indeed, MBE benefits from high accuracy in the doping of the materials and precise control of the growing conditions, resulting in high quality structure of the grown layers. In order to check the quality of the growth process, a Brewster characterization is performed. The Brewster characterization investigates the plasma frequency of a heavily doped semiconductor layer, in our case, the ENZ layer. This analysis is done as an intermediate step to check that the growth settings are correct, regarding especially the doping, and at the end, to check the final result of the growth. Its validity has been discussed by Taliercio *et al.* in 2014, both on a theoretical and experimental level [11].

In a Brewster characterization, the layered wafer is illuminated by a light with oblique incidence. With a transverse electric polarization (p-polarization), the light excites a leaky longitudinal mode propagating along the surface of the doped layer. This is the Brewster mode. The presence of this leaky mode can be probed with a reflectance measurement. Indeed, the excitation of this mode creates a dip in the reflectance spectrum of the wafer, and this dip can be related to the plasma frequency of the heavily doped layer. Moreover, the experiment can be simulated by means of Fresnel coefficient and transfer matrix method. The free parameters of the model are the permittivity and the thickness of each layer. The permittivity of each layer is described with a Drude model: for the undoped layer the epsilon infinity, the plasma frequency and the losses can be found in the literature. Even if there are small deviations from the literature values, these parameters do not strongly affect the simulated spectrum. On the other hand, a correct model of the doped layer is crucial to reproduce the experimental spectrum. Indeed, the spectral position of the Brewster mode is mainly determined by the plasma frequency of the heavily doped layer, while its linewidth is related to the losses of the same layer.

Moreover, in a Brewster characterization, interference fringes are typically observed at high energies. These fringes are the consequence of the light reflected at every interface between the layers in the wafer, interfering with the light propagating in the wafer. The periodicity of these fringes is mainly related to the thickness of the layers.

Thus, we can perform a fine tuning of these parameters to fit with the experimental spectrum. When we find a good agreement, we can extract parameters of the fitting (the plasma frequency and the losses of the doped film, the thickness of each layer) and compare them with the goal of the growth process.

In fig. 3.18 I report the Brewster measurement of our wafer (in blue), in good agreement with the simulated fitting (in red). The parameters we extract from the fitting are the plasma frequency of the ENZ layer (in wavelength $\lambda_{\mathrm{ENZ}} \approx 10.0$ µm), the losses of the ENZ layer ($\nu_{\mathrm{c}} \approx 1.3 \times 10^{12}$ rad s^{-1}), the thickness of the undoped InAs on top ($t_{\mathrm{a}} = 1.6$ µm) and the thickness of the ENZ layer ($t_{\mathrm{ENZ}} = 2.2$ µm). The only noticeable difference from the initial goal is in the thickness of the ENZ layer, for which the target was 2.4 µm. However, this difference should not affect the antenna resonances.

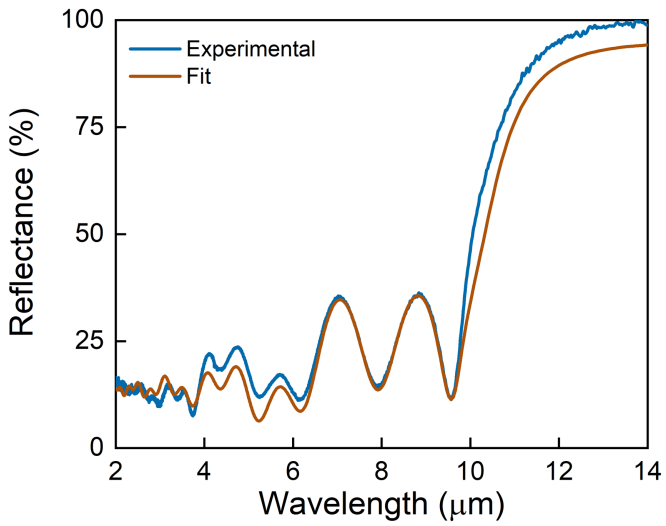

Figure 3.18: The results of the Brewster characterization of the wafer. In blue, the experimental Brewster measurement, in brown its fit obtained with the trasnfer matrix method. From the fit, we extract the final parameters of the wafer.

3.4.2 Fabrication

The antennas were fabricated via electron-beam-lithography (EBL). In EBL, an electron beam is focused on the sample, which is covered by a layer sensitive to the flow of electrons. The beam can reach spot sizes of less than 10 nm, and it is scanned on the sample following a designated pattern [108]. The electron beam leaves a mark on the layer covering the sample, called photoresist. The marked areas in the photoresist show a different robustness and solubility than the unmarked ones. Thus, it is possible to selectively remove the marked or the unmarked areas in the photoresist. This leaves a pattern on top of the sample, showing the design that has to be fabricated. In the end, another etching process (wet or dry etching), filtered by the photoresist, transfers the pattern in the layers of the sample. EBL is a powerful and vastly used technique in the manufacture of nanotechnologies. The main advantages of EBL are its high resolution (lower than 10 nm), reproducibility and versatility. For instance, let us compare EBL with a similar technique, photolithography, which employs light instead of electrons. While photolithography needs a non-modifiable physical mask to produce the desired pattern in the structure, in EBL the design is produced by scanning the electron beam on the structure. This scanning is completely controllable, therefore EBL can be used to design highly customizable structures. Moreover, a maskless fabrication process guarantees more versatility in the development phase. To summarize, EBL is an accurate and flexible technique, exploited to realize a diverse range of nanotechnological structures, e.g. nanophotonic metamaterials [109], integrated waveguides [48], specifically tailored

probes (i.e., the silicon nitride AFM probe studied in chapter 2), high-quality plasmonic and dielectric resonators [87, 110].

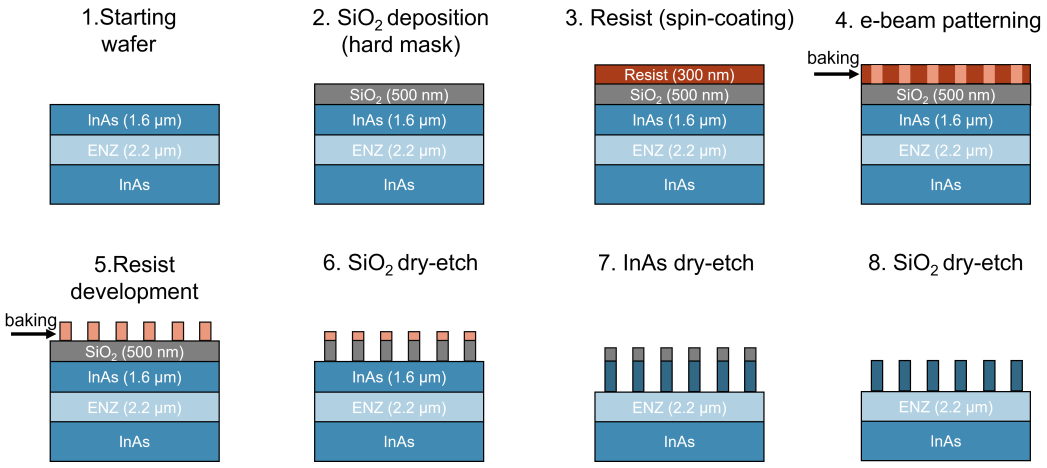

Figure 3.19: The workflow followed to fabricate the nanoantennas through electron-beam-litography.

We fabricated the platform in the clean room at the Institut d'Électronique et des Systèmes in Montpellier. The steps followed to fabricate the nanoantennas are pictured in fig. 3.19. We start from the multilayer described in the previous section. From the Brewster characterization, we have an estimate of the thickness of the layers. Since the InAs top layer is 1.6 µm thick (corresponding to the height of the antennas), the etching of this layer is a delicate step. Indeed, the standard recipes for selective etching of III-V semiconductors typically work for hundreds of nanometers, so we need to modify them for the etching of a 1.6-µm-thick layer. The main problem is the strength of the photoresist pattern on top, which could vanish when etching the 1.6 µm layer. If this happens, we do not have the mask of the photoresist anymore and the pattern is not reproduced in the InAs layer. So, in order to harden the lithography mask, we deposit a SiO_2 layer on top of the sample. This is a procedure typically adopted to etch thick semiconductors layers. In the end, on top of the InAs layer we will have pillars of SiO_2 and photoresist. These pillars provide the pattern which defines the nanoantennas in the InAs layer after etching.

So, first, we need to determine the optimal thickness of the SiO_2 layer. We perform several tests, with the standard recipes for InAs dry etching. Among the different recipes, we choose the most selective one, meaning the one that etches the largest quantity of InAs for the same amount of SiO_2. Finally, the recipe we chose is an argon-based plasma dry etching, showing a selectivity between 4 and 5 (meaning that for 100 nm of SiO_2 a thickness between 400 and 500 nm of InAs is etched). Following this result, we deposit a 500 nm SiO_2 layer on the sample, enough to preserve the SiO_2 mask during the 1.6-µm-thick InAs layer etching. The successive step is deposition of the resist layer. We

use the AZ®2020 diluted in a AZ®EBR solvent, with a 100:80 dilution, which is a negative resist, meaning that after the electron beam deposition, the unmarked areas are removed to obtain the resist mask. The layer is deposited by spin coating, with 6000 rotations-per-minute for a duration of 30 s associated to a thickness of roughly 300 nm. The resist is then hardened by baking at 110 °C for 60 s. At this stage, we have the resist layer on top of the SiO_2 mask and we can proceed with the EBL patterning.

The EBL is performed on a custom built machine, composed by electron gun from Raith GbmH nanofabricator coupled with a SEM machine JEOL. The initial current of the electron gun is 10 pA in order to electrically charge the resist with a charge density of about 14.67 $\mu C\,cm^{-2}$. The value of the current is then multiplied by a factor going from 0.1 to 1.6 with a step of 0.1, obtaining 16 different areas patterned with different currents. A change in current affects the radius of the antennas especially, so every area is associated to a different radius of the pillars. We target samples of 500×500 μm^2, which means we will have $50 \times 50 = 2500$ antennas (since the periodicity of the antennas is fixed at 10 µm) for each area.

After the EBL patterning, the resist is hardened by a second baking at 100 °C for 60 s and then developed for 40 s by using AZ®726 MIF developer. Then, the etching process is performed. We etch the 1.6 µm layer of InAs using an Ar-based plasma using an inductively coupled plasma-reactive ion etching (ICP-RIE) machine from Oxford Instruments. The Ar flow is 25 sccm with a pressure of 5 Torr, generated with a radio-frequency power of 50 W. The etching process lasts around 20 minutes. The residual thickness of the SiO_2 mask (200-300 nm) is then etched by a selective flourine-based plasma for 3 minutes. The fabrication process is completed and we are left with pillars of InAs on top of the ENZ substrate.

3.5 Characterization of the antennas

3.5.1 SEM images

The antennas are first characterized with scanning electron microscopy. In fig. 3.20 the SEM images of the sample are reported. We see that the antennas are arranged in an ordered pattern, with the desired periodicity. Also, from the side view we evaluate the height of the pillars, which is roughly 1.6 µm. However, the antennas present tilted lateral walls. By looking at the SEM images, we can evaluate the angle of the walls with the substrate, which is around 60°. The tilt is due to the etching process, since it is the most delicate step in the fabrication process, especially for such a thick layer. Obviously, the tilted walls create a discrepancy with respect to the model we used for the optimization, which simulated perfectly straight cylinders. Thus, it is important to propose a more complete model, discussing the differences caused by the tilted walls, both in the field distribution and the lineshape of the resonance.

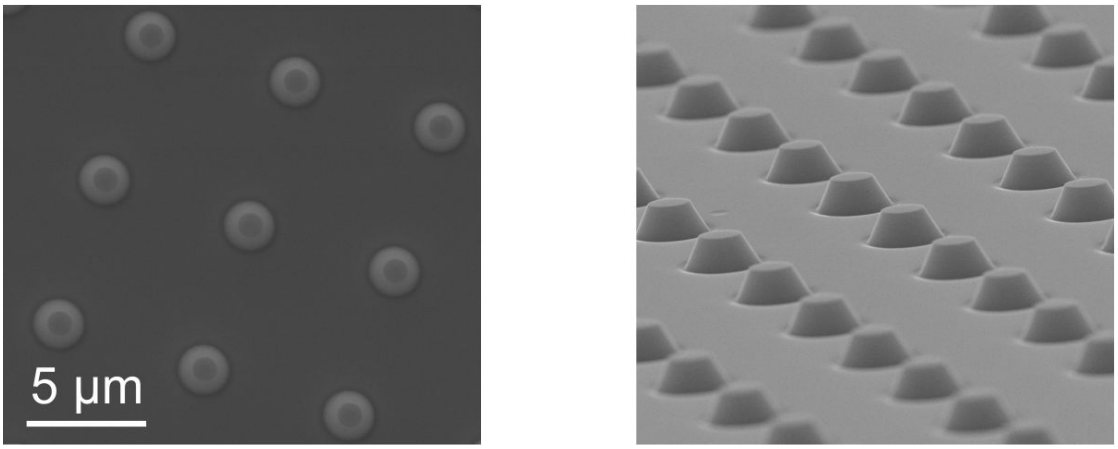

Figure 3.20: Top view (left panel) and tilted view (right panel) of the nanoantennas, produced by SEM imaging. From the image on the left, we can appreciate the tilt of the antenna walls.

3.5.2 AFM images

The next step of the characterization is to perform an AFM set of images of the patterned area. In this measurement, an AFM tip scans the sample, assessing the morphological properties of the pillars. The raw data are then fed to the software Gwyddion, analysed and then plotted. In fig. 3.21 the AFM scanning of a patterned area is shown. First, we extract the 3D reconstruction of the antenna array (panel a). This confirms what was observed in the SEM images. However, looking at more dedicated data, we see some more details. Thus we extract the profile of the surface along the two in-plane dimensions of the array (panel b). From this view we can estimate the tilt in the antenna walls. Also, we can see that there is a small and sharp dip in the ENZ materials close to the basis of the antennas. Again, this is most likely due to the etching of the top InAs layer. In panel c, the top AFM view is reported. Here, the top of the pillar (bright white) is surrounded by a broader area (opaque white), representing its basis. This can be seen by zooming on a single pillar (panel d). Lastly, we can extract a numerical estimate of the pillar geometry. From the AFM map, we can gather information about the top radius ($r_{\text{top}} \approx 3.2$ µm), the lower radius ($r_{\text{bottom}} \approx 4.7$ µm), the height ($h \approx 1.6$ µm) and the periodicity ($p \approx 10.0$ µm) of the pillars. The tilt of the pillars can be estimated from this data, resulting around 60°, in agreement with the previously reported measurement on the SEM images.

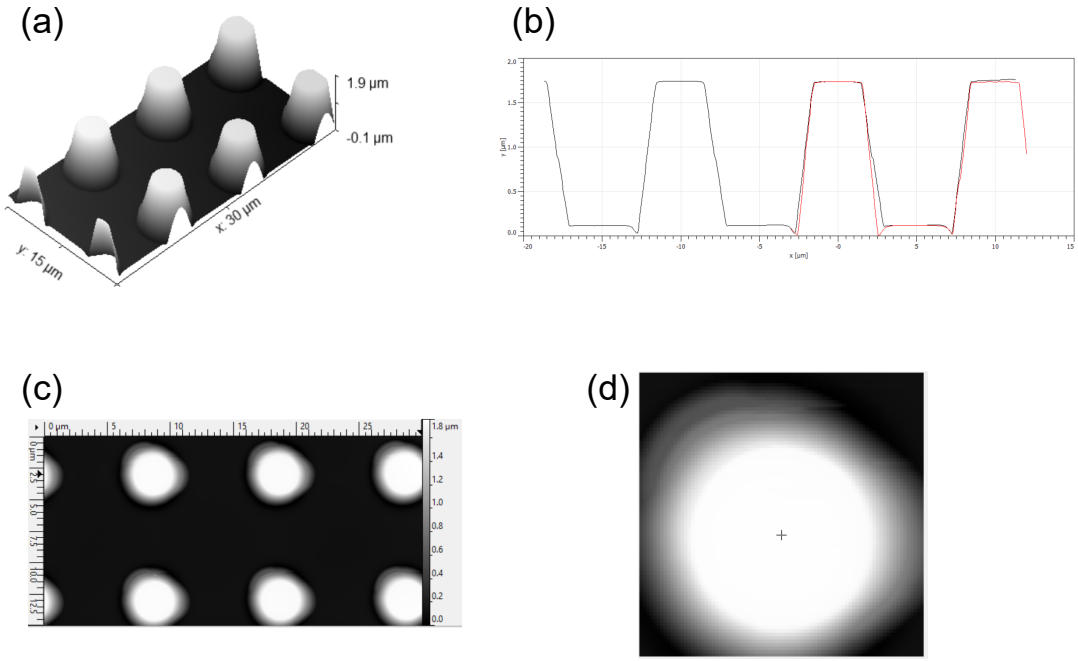

Figure 3.21: In a, the 3D AFM reconstruction of the sample. In b, the profile of the patterned area along the two directions of the array (black and red curves). We can estimate the tilt of the antenna walls. In c, the top view of the AFM scanning. Panel d shows the zoom on a single antenna, where we can see the beak at the bottom due to the EBL writing.

3.5.3 Reflectance spectra

The antennas are then characterized by collecting their reflectance spectrum with a FTIR coupled with an optical microscope. The optical microscope allows to focus on and collect the light from the 500×500 µm^2 patterned areas. We take the reflectance spectra of every single patterned area, which differ only in the radius of the antennas. In the end, by looking at the different spectra we are able to evaluate the effect of the radius. Both illumination of the sample and collection of the reflected light are performed through an objective of numerical aperture NA=0.5. This parameter defines the portion of light which is accepted in the objective. Since the objective is in air, it accepts the light with an incidence up until 30°. This is an important parameter, since it defines the range of wavevectors coupling with the antennas in illumination and the wavevectors of the reflected light in collection. Indeed, in this case, the illumination cannot be modelled by a plane wave, as we did in our first simulations. The focusing of the light has a major effect in broadening the resonances of the antennas, as it will be discussed in the next paragraphs.

Representative reflectance spectra are reported in fig. 3.22. We can divide the spectra in three regions. At short wavelengths, in the blue zone, we mainly see interference fringes, as the ENZ layer behaves like a dielectric substrate. The dip around 10 µm

corresponds to the resonance that we designed. This dip does not shift as we change the radius, which could be surprising, because the spectral position of local resonances depends on the dimensions of the antenna. So, upon changing the aspect ratio of the antenna, we should be able to notice a shift in the resonance. Still, we can see that in the red, blue and yellow curve (small values of the radius) the dip is at a fixed position. This can be explained by considering the pinning effect of the lattice resonance and of the ENZ condition. These two resonances are strong and spectrally fixed, once we define the periodicity of the resonators and the doping of the substrate layer. For this reason, they "attract" the spectrally close features of the antennas (in our case, the electric dipole resonance was designed to occour close to 10 µm) to their wavelength. In the end, for small radii, the three resonances collapse in a single dip around 10 µm. However, when the radius becomes too large (2.1-2.3 µm, light blue and purple lines), the local resonance gets too far from 10 µm, and the dip is split into two less deep features. The main one, around 10 µm, is still due to the spectrally fixed resonances, the lattice coupling and the ENZ condition, while the depression at higher wavelength represents the electric dipole of the antennas. So, in the case of high radii, the resonances are not coupled anymore, leading to a weaker field enhancement. Indeed, as we saw in the optimization process, the best field enhancement is obtained when all the resonances are coincident. Above the ENZ condition, the substrate behaves like a metal. Indeed, we see the reflectance going close to 100%. However, we also see the presence of several resonances which depend on the radius of the antennas. These resonances will be thoroughly discussed in the next section.

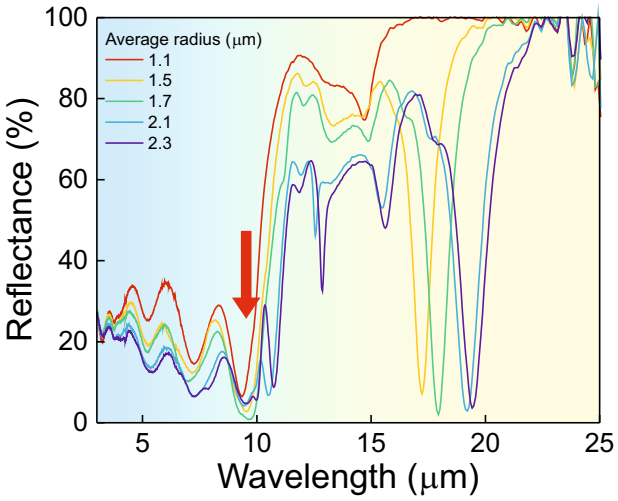

Figure 3.22: Reflectance spectra of antennas with different average radii (as reported in the legend). The blue-colored area corresponds to a dielectric behavior of the substrate, the red arrow points to the ENZ condition and in the yellow part the substrate behaves like a metal.

3.5.4 Simulation of the truncated cone

In order to explain the features seen in fig. 3.22, we performed a new set of numerical simulations. Indeed, it is interesting for both exploring how the deviation from the ideal geometry influences the resonance we design, and extending the spectral range to explain the features we observe at long wavelengths. First, we analyze the effect of the geometry. We perform two simulations, one studying the optimized cylinder (r, h) and the other studying a truncated cone with an average radius equal to the radius of the cylinder (the walls are tilted by 60°, as observed in the SEM images of the sample). The height is fixed for both structures at $h = 1.6$ µm. In these simulations, we kept a plane wave illumination, even if it does not well represent the experimental situation, where a focused gaussian beam is employed. Indeed, the overlap of several sharp resonances (ENZ condition, periodicity and antenna resonance) strongly raises the computational cost of these simulations, which are even more complex with a properly modelled gaussian beam. The simulated reflectance spectra are reported in fig. 3.23 (panel a). In the figure, we can see the sharp resonance at 10 µm presents the same lineshape and intensity in both cases. By looking at the xz section of the pillar, we can see that the field distribution slightly changes (panels b and c). The enhancement is still mainly outside the particle, but for the truncated cone it is evenly distributed along the walls (panel b), whereas the cylinder presents more localized hotspots at the top (panel c). The more uniform field distribution along the walls of the pillar could benefit the enhancement of molecular signals, when the molecule randomly cover the whole sample.

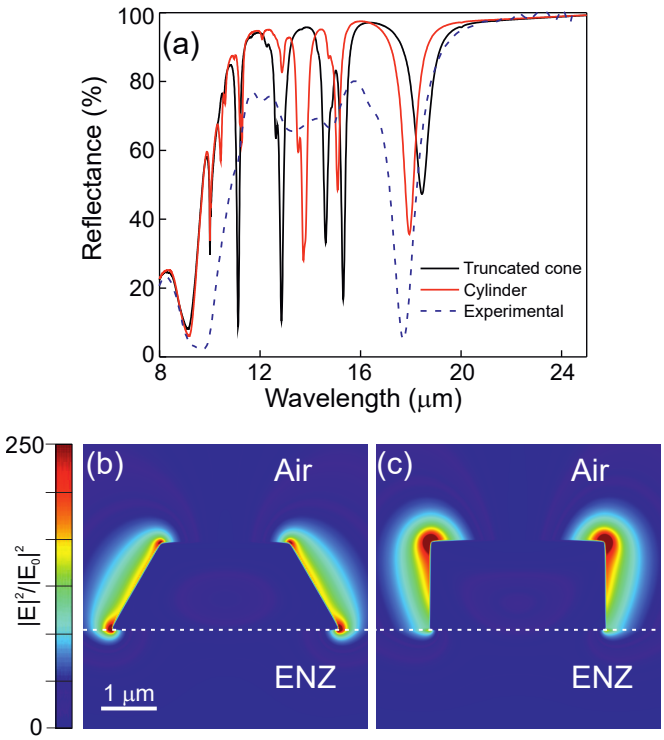

Figure 3.23: In panel a, the reflectance spectrum of the simulated truncated cone (with an average radius $r = 1.6$ µm and height $h = 1.6$ µm) in black, of the cylinder ($r = 1.6$ µm and $h = 1.6$ µm) in red, and the experimental spectrum of the correspondent antenna array in dashed blue. In panels b and c, a comparison of the near-field distribution obained with the truncated cone and the cylinder, respectively.

Another difference between the ideal cylinder and the real geometry is seen in the right part of the spectrum. Indeed, the resonances at longer wavelengths present different position, lineshape and intensity according to the geometry employed. Let us discuss the physical nature of these resonances. Fig. 3.24 plots the simulated real part of the z-component of the electric field in the xz section of the pillar (modelled as a truncated cone) at the reflectance dips. From these graphs, we can appreciate localized hotspots forming at the interface between the substrate and the antennas. This spectral region, beyond 10 µm, is above the ENZ condition, meaning that the substrate behaves like a metal, as we see the reflectance going to 100%. Indeed, the physical nature of these resonances is linked to the substrate behavior, which sustains plasmonic oscillations on its surface. These oscillations are confined by the high-index pillars on top, creating standing waves at the basis of the resonators. So, in this spectral region, the system acts like a dielectric-loaded plasmonic substrate. Changing the radius of the antennas means changing the distance between them, and thus the confinement of the plasmonic oscillations: this is the reason for their dependence on the radius. These resonances are difficult to employ for sensing applications. Indeed, their very nature confines the field

enhancement mostly at the interface between the substrate and the antennas, with the highest enhancement inside the pillars, which is not practical for sensing applications, because the molecules would be outside the particle. On the other hand, the resonance at 10 µm shows an enhancement well distributed along the outer part of the antenna walls (fig. 3.23), which is a more favorable situation for sensing. Nevertheless, all features are really interesting, specifically for their high field enhancement, indeed the main resonance at longer wavelengths almost cancels out the reflected light, even more in the experimental spectra (fig. 3.22). Moreover, they present sharp linewidths, which reflects high Q-factors.

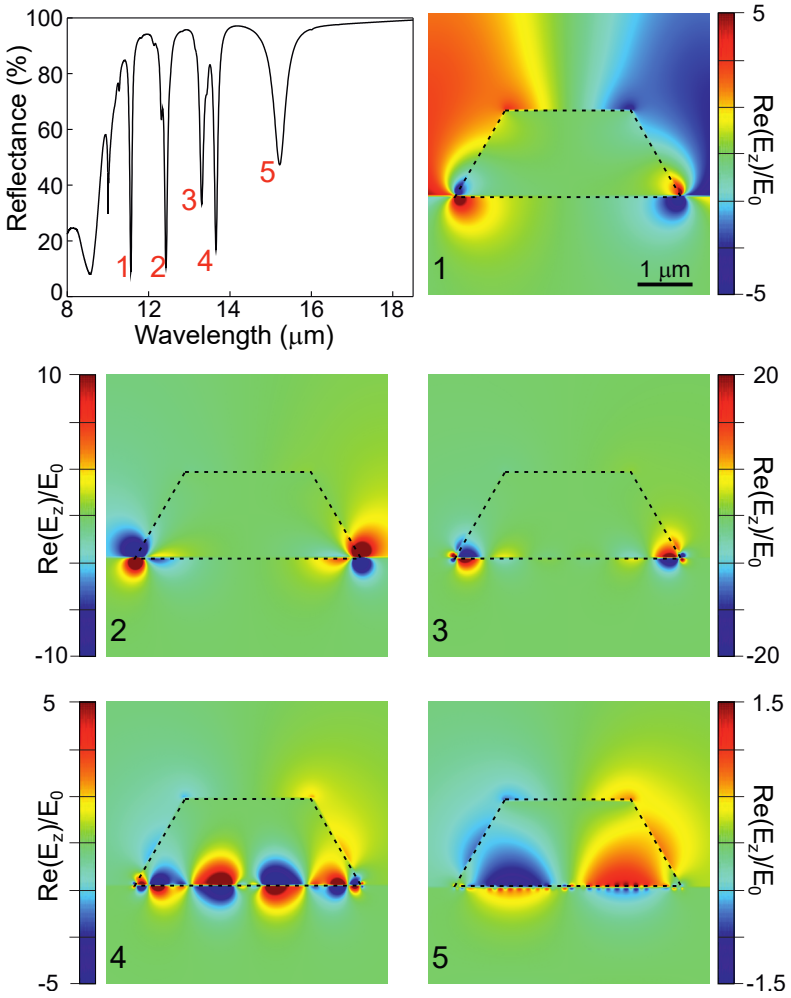

Figure 3.24: In a, the reflectance spectrum of the truncated cone with an average radius $r = 1.6$ µm and height $h = 1.6$ µm. In the panels from 1 to 5, the z-component of the electric field at the correspondent reflectance dip.

By comparing the simulated spectra (fig. 3.23) with the correspondent experimental one (dashed blue line), we can see that the truncated cone is a more precise model of the pillar. The simulated data reports all the peaks observed in the experiment, even if wavelength-shifted and with sharper linewidth. The wavelength shift is probably caused by small error in the geometrical or optical parameters modelling the antenna. The sharper resonances in the simulations, instead, are mainly due to the ideal modelling of the illumination. A non-collimated beam, like the one in the experiment, would have a worse coupling with the resonances of the platform, in particular the lattice resonance, leading to a broadening of the associated spectral features. Moreover, a wrong estimate of the material losses, or the non-ideal geometry of the pillars, could be a factor in the discrepancy between modelled and experimental linewidth. In fig. 3.25 I report the simulated spectrum of the optimized truncated cone, in which the features are artificially broadened by a convolution with a gaussian function (orange line). Here, we can appreciate the fair agreement with the experimental one (blue line).

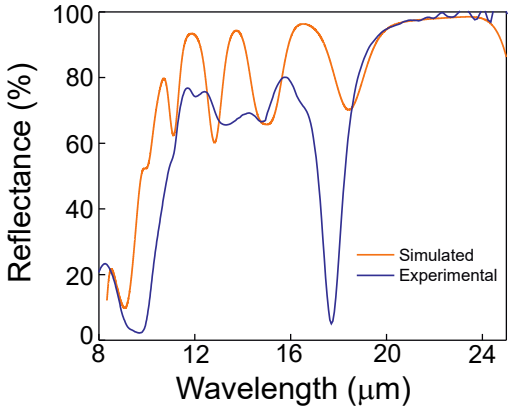

Figure 3.25: In orange, the simulated reflectance spectrum of the truncated cone (average radius $r = 1.6$ µm and height $h = 1.6$ µm) is artificially enlarged b a convolution with a gaussian function. It is compared with the associated experimental spectrum (in blue).

3.6 Sensing experiment

3.6.1 Functionalization of the platform

To perform a sensing experiment, the first step is the choice of the molecule to probe. Since the antenna resonance we designed is at 10 µm, we choose a molecule showing an absorption line close to that wavelength. Moreover, to test the sensitivity of our platform, it is preferable to deposit a small quantity of molecules on the platform, tentatively a monolayer. This can be done through the process of functionalization. Keeping this aim in mind, we choose perfluorooctyltrimethoxysilane (PFTMS) as the molecule to probe. This molecule is a silane, a group often studied in IR sensing, especially for the detection

of toxic gases [106]. It presents several absorption peaks in the MIR, as reported in fig. 3.26 (panel b), especially one close to 10 µm.

PFTMS, as other silanes, benefits also from a strong practical knowledge, being widely studied in the field. The first step of the functionalization process is to prepare the solution to deposit over the platform. For silane composites, chloroform represents the best solvent. The mass of the functionalizing agent is defined by $m = C \times V \times M$, where C is the excess concentration, aimed to be 10^-3 mol L^{-1}, M is the molecular weight and V is the volume of the solution (around 50 mL). The mass of the agent is around hundreds of mg. The solvent and the functionalizing agent are mixed together with a magnetic plate for 5 minutes. At this point, the sample is cleaned with acetone, then left in the solution for 24 hours. After this, the sample is washed in chloroform to eliminate the weakly-bonded molecules (physically adsorbed), remaining with only the chemically adsorbed ones. Lastly, the sample is baked in an oven for 12 hours to form a uniform film of functionalized molecules.

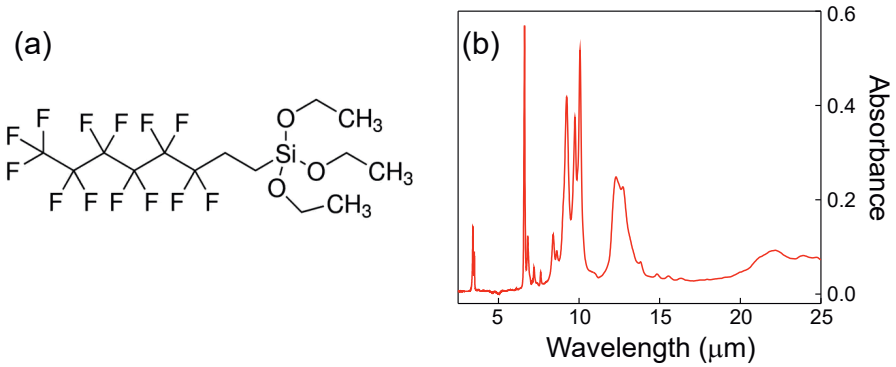

Figure 3.26: In a, the chemical representation of PFTMS. In b, its absorption spectrum (given by the molecule supplier SiKÉMIA), showing several peaks in the fingerprint.

3.6.2 Sensing experiment

The functionalized platform is measured with the same experimental conditions of section 3.5.3. In this way, a direct comparison between the spectra of clean and functionalized platform is possible. From this comparison, we compute the differential reflectance: $\Delta R = \frac{R_{\text{func}} - R_{\text{clean}}}{R_{\text{clean}}}$. The spectrum of ΔR is reported in fig. 3.27 for the same antenna radii considered in fig. 3.22. For short wavelengths, until around 3 µm, the spectrum is flat for every value of the radius. Here the substrate behaves like a dielectric and the antennas are not in resonance, so there is no field enhancement (from both the antennas and the ENZ layer) probing the presence of the molecules. In the rest of the spectrum, we have to consider two optical effects associated to the molecular film: a change in the refractive index of the environment and the absorption of PFTMS. Both effects contribute in determining the spectrum of ΔR. Since the interconnection of these two effects produces a signal of difficult interpretation, let us first single out the contribution

of the refractive index change. At long wavelengths (above 15 µm), PFTMS does not present any absorption peaks, so ΔR is due to the refractive index of the molecules. In this region, ΔR presents the up-down lineshape characteristic of a resonance red-shift (around 14, 16 and 20 µm). The shifting resonances are the plasmonic resonances of the substrate, which behaves like a metal in this spectral region. The differential reflectance reaches values of 100% in this region, proof that these resonances are very sensitive. This is a demonstration of refractometric sensing, where the resonance shift is a measure of the molecular refractive index. Now let us focus on the situation around 10 µm, where we designed the resonance of the antennas. Here, we have both contributions, from the refractive index and the absorption of the molecules, so the situation is more complex. By looking at the zoom in fig.3.27, we see spectral features different from the typical refractometric ones, as seen at longer wavelengths. Indeed, here the ENZ condition pins the spectral position of the resonances, so a change in the refractive index has a small effect. The lineshape of ΔR for different radii suggests that we are indeed probing the absorption peaks of PFTMS. The largest values of ΔR corresponds to 30%, for the smallest radius (red line). Still, the green and yellow lines show similar trends and values. As we further increase the radius (light blue and purple lines), we see that the enhancement red-shifts, and the resonances of the platform have a weaker coupling, leading to a smaller field enhancement. Given the complexity of these data, it is difficult to separate all the contributions, and thus to find an estimate of the platform's sensitive power. One way to do this would be to accurately simulate the experiment, modelling properly the optical properties and the thickness of the molecular layer. However, as already discussed, the presence of several sharp resonances already raises the computational complexity of the clean platform, so reproducing these spectra is extremely challenging. This remains an open point, which will be further developed in the near future.

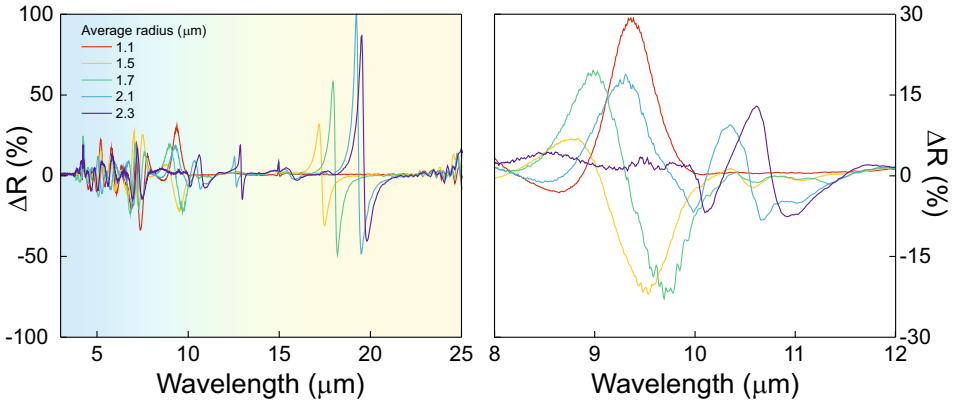

Figure 3.27: On the left, the differential reflectance spectrum for several values of the antenna radius. The features at high wavelengths correspond to a wavelength shift due to the refractive index of the molecues. On the right, a zoom around 10 µm. Here we have the contribution of the vibrational absorption lines, which spectrally overlap with the main resonance of the platform.

3.7 Conclusions

3.7.1 Summary

The aim of this work was to extend the working range of dielectric antennas to the MIR. We realized this objective, with a platform exploiting an ENZ material as the substrate. The choice of the substrate is the key part of our work: the optical properties of an ENZ material can be tailored to guarantee the best field confinement of the antennas. From a manufacturing point of view, we can realize the ENZ substrate by properly doping a semiconductor. This enables the realization of an all-semiconductor platform, which carries the benefits of semiconductor technology. Indeed, being extremely developed, both in laboratory and industrial applications, the use of semiconductors employs mature, high-quality and foundry-compatible growth and fabrication techniques, which is an extremely important technological advantage in the realization of an antenna-based platform. In summary, these are the main points of this work:

- First, I discuss the context of nanoantennas working in the MIR, focusing on dielectric resonators and their extension to the MIR. On the one hand, their resonances suffer from the use of high-index substrates, which is the case of semiconductors in the MIR, typically used in epitaxial growth. On the other hand, by using other substrates, already employed especially for plasmonic antennas (e.g. CaF_2), we obtain low-quality structures and larger losses in the fingerprint region.

- We propose a solution to these limits, by employing an ENZ substrate made of a heavily-doped semiconductor. In this way, we can control the optical properties by changing its doping and at the same time exploit an epitaxially grown platform.

- By performing optical simulations, we optimize the structure to have the highest near-field, in order to exploit it for vibrational sensing. We combine the electric dipole of the antennas, their periodicity and the ENZ condition of the substrate. We give an estimate of the expected near-field enhancement at resonance.

- We realize the platform by exploiting epitaxial growth of the semiconductor layers and electron beam lithography to fabricate the nanoantennas. The antennas are then characterized by means of SEM and AFM images, and FTIR reflectance spectra. The reflectance spectra show the resonance we design, demonstrating the extension of dielectric antennas to the MIR.

- Lastly, I report the results of a sensing experiment, in which we probe a functionalized monolayer on top of the antennas. We detect a molecular signal enhanced by the main resonance of the platform. However, the differential reflectance spectrum is influenced by both the change in the refractive index and the absorption of the molecules. Singling out each contribution is challenging: this remains an open point.

To conclude, this is a proof of concept demonstrating a high-quality sensor which can be mass-produced and easily employed in IR spectroscopic detection. The use of dielectric

resonances paves the way for new interesting applications. Indeed, one of the main advantages of using dielectric antennas over plasmonic ones is the possibility to exploit magnetic resonances. In some applications, e.g. chiroptical sensing, magnetic resonances are crucial. In the next and final section, I will discuss how we can exploit the same concept to realize a chiroptical sensor.

3.7.2 Perspective: chiroptical sensing

In this thesis, I focused on designing, building and characterizing nanostructured system which improve the detection and recognition of small amounts of molecules. The successive step is to use the same concepts to improve chiral detection. Indeed, since the chiral nature of biomolecules affects the majority of bioprocesses, being able to easily discriminate the handeness of a molecule would be extremely important, more so, to do it optically, in a non-invasive way. Also, by doing this in the MIR, we keep all the benefits of MIR spectroscopy, especially the chemical labelling coming from the vibrational absorption lines. However, chiroptical signals are typically weak, especially in the MIR. We need to find a way to enhance them. This chapter is focused on enhancing the absorption of molecules, by optimizing the electric field intensity close to properly tailored nanoantennas. For chiral sensing, we follow the same process, but with a different figure of merit: the so-called optical chirality C. C can be written as [30]:

$$C = -\frac{\epsilon_0 \omega}{2} \mathrm{Im}(\mathbf{E}^* \cdot \mathbf{B}), \tag{3.8}$$

where the symbol * stands for complex conjugate. Optical chirality is a measure of the differential absorption between left and right circularly polarized light in the dipolar approximation for a given molecule. We can optimize C by properly tailoring the electromagnetic fields: the best condition corresponds to E and B spatially and spectrally overlapping, and a phase shift between the two of $\frac{\pi}{2}$. These requirements can be met locally by employing antenna resonances. In particular, the optimal condition is reached when the electric and magnetic dipole are spectrally coincident. This was discussed e.g. by Solomon *et al.* in 2018, with a numerical study on the dipolar resonances of an ordered array of dielectric pillars (refractive index $n = 3.5$), working in the NIR [13]. In fig. 3.28 (panel a), the dashed lines mark the spectral position of the electric ($\mathbf{p_e}$ in the figure) and magnetic ($\mathbf{p_m}$) dipolar resonances, with respect to the radius of the pillar (the height is fixed, $h = 200$ nm). The presence of the resonances is marked by a minium in the transmission of the platform (represented by the colormap). The two resonances have a different dependence on the radius of the antennas, meaning that by properly tuning this parameter we can find the spectral coincidence of the two dipolar resonances. In panel b, the highest absolute value of optical chirality around the particle is computed for the same geometries of panel a. In this case, the best situation is reached when the two resonances are coincident.

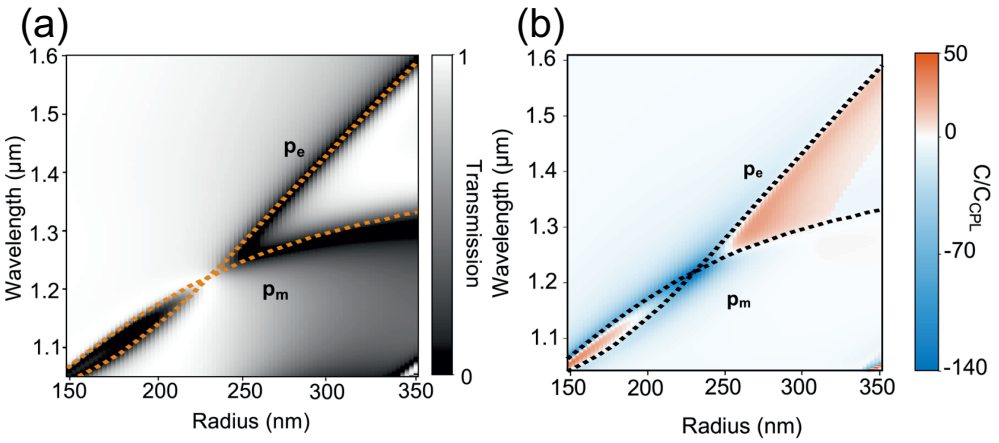

Figure 3.28: On the left (panel a), the transmission of the platform, with the electric and magnetic dipoles spectrally moving when changing the radius of the pillars. On the right (panel b), the correspondent highest absolute value of C outside the pillars. Adapted from ref. [13].

With these concepts in mind, we design a new platform optimizing C. Since we use the same wafer as before, the maximum height of the antennas and the ENZ wavelength are fixed. Thus, we perform an optimization of C by keeping the radius, the height and the periodicity of the pillars as free parameters. The figure of merit here is the integral of C on a surface surrounding the pillar at 200 nm distance. The pillar is modelled as a truncated cone, with 60°-tilted walls. We do not fix a wavelength in the optimization, just a spectral region, between 8 and 12 μm. In fig.3.29 I report the xy and xz maps of the enhancement of ΔC, which is the difference between the C obtained with circular left illumination and the one obtained with circular right illumination. This maps are computed at optimal condition, represented by the overlap between the electric and magnetic dipole resonance, which occours at $\lambda_C \approx 10.5$ μm. The platform shows enhancement even higher to the ones already exploited for chiral sensing with dielectric resonators in the visible and near-infrared range [14], while also extending the range of application to the MIR. Moreover, in the xz map we can appreciate the presence of strong C hotspots at the basis of the pillar, probably due to the ENZ substrate. The nature and the optimization of these hotspots will be studied in the near future, since they are promising for chiral sensing.

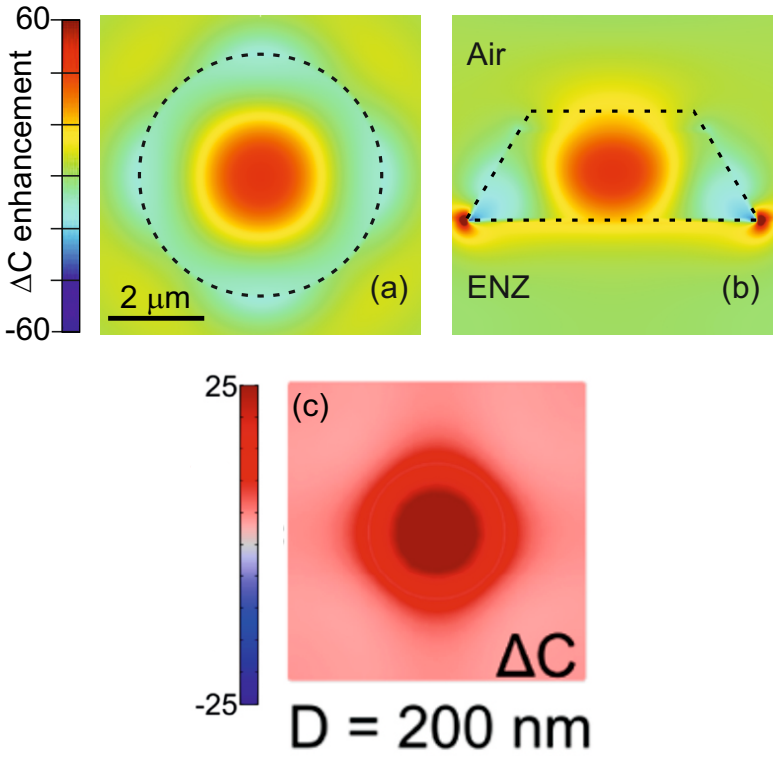

Figure 3.29: Differential chirality enhancement distribution in the xy (a) and xz (b) section of the pillar at resonance ($\lambda_C \approx 10.5$ µm). The ΔC hotspots are inside the pillar, where the electric and magnetic dipole resonances overlap, and at its basis, due to the presence of the ENZ substrate. The pillar has an average radius $r = 2.2$ µm, height $h = 1.6$ µm and periodicity $p = 10.2$ µm. Panel c reports the xy ΔC map of a similar platform working in the near-infrared taken from ref. [14], for comparison.

Bibliography

[1] P. Larkin. *Infrared and Raman spectroscopy: principles and spectral interpretation.* Elsevier (2017).

[2] J. Chae, S. An, G. Ramer, V. Stavila, G. Holland, Y. Yoon, A. A. Talin, M. Allendorf, V. A. Aksyuk, and A. Centrone. Nanophotonic Atomic Force Microscope Transducers Enable Chemical Composition and Thermal Conductivity Measurements at the Nanoscale. *Nano Letters* **17**, 5587 (2017). PMID: 28770607.

[3] V. Giliberti, R. Polito, E. Ritter, M. Broser, P. Hegemann, L. Puskar, U. Schade, L. Zanetti-Polzi, I. Daidone, S. Corni, F. Rusconi, P. Biagioni, L. Baldassarre, and M. Ortolani. Tip-Enhanced Infrared Difference-Nanospectroscopy of the Proton Pump Activity of Bacteriorhodopsin in Single Purple Membrane Patches. *Nano Letters* **19**, 3104 (2019). PMID: 30950626.

[4] F. Neubrech, A. Pucci, T. W. Cornelius, S. Karim, A. García-Etxarri, and J. Aizpurua. Resonant Plasmonic and Vibrational Coupling in a Tailored Nanoantenna for Infrared Detection. *Phys. Rev. Lett.* **101**, 157403 (2008).

[5] O. Yavas, M. Svedendahl, P. Dobosz, V. Sanz, and R. Quidant. On-a-chip Biosensing Based on All-Dielectric Nanoresonators. *Nano Letters* **17**, 4421 (2017).

[6] R. Adato, A. A. Yanik, J. J. Amsden, D. L. Kaplan, F. G. Omenetto, M. K. Hong, S. Erramilli, and H. Altug. Ultra-sensitive vibrational spectroscopy of protein monolayers with plasmonic nanoantenna arrays. *Proceedings of the National Academy of Sciences* **106**, 19227 (2009).

[7] W. Kaiser, W. Spitzer, R. Kaiser, and L. Howarth. Infrared Properties of CaF_2, SrF_2, and BaF_2. *Physical Review* **127**, 1950 (1962).

[8] H. Li. Refractive index of alkaline earth halides and its wavelength and temperature derivatives. *Journal of Physical and Chemical Reference Data* **9**, 161 (1980).

[9] F. B. Barho, F. Gonzalez-Posada, M.-J. Milla, M. Bomers, L. Cerutti, E. Tournié, and T. Taliercio. Highly doped semiconductor plasmonic nanoantenna arrays for polarization selective broadband surface-enhanced infrared absorption spectroscopy of vanillin. *Nanophotonics* **7**, 507 (2018).

[10] J. Kischkat, S. Peters, B. Gruska, M. Semtsiv, M. Chashnikova, M. Klinkmüller, O. Fedosenko, S. Machulik, A. Aleksandrova, G. Monastyrskyi, et al. Mid-infrared optical properties of thin films of aluminum oxide, titanium dioxide, silicon dioxide, aluminum nitride, and silicon nitride. *Applied optics* **51**, 6789 (2012).

[11] T. Taliercio, V. N. Guilengui, L. Cerutti, E. Tournié, and J.-J. Greffet. Brewster "mode" in highly doped semiconductor layers: an all-optical technique to monitor doping concentration. *Opt. Express* **22**, 24294 (2014).

[12] S. Adachi. Optical dispersion relations for GaP, GaAs, GaSb, InP, InAs, InSb, Al x Ga1- x As, and In1- x Ga x As y P1- y. *Journal of Applied Physics* **66**, 6030 (1989).

[13] M. L. Solomon, J. Hu, M. Lawrence, A. García-Etxarri, and J. A. Dionne. Enantiospecific optical enhancement of chiral sensing and separation with dielectric metasurfaces. *ACS Photonics* **6**, 43 (2018).

[14] J. Garcia-Guirado, M. Svedendahl, J. Puigdollers, and R. Quidant. Enhanced chiral sensing with dielectric nanoresonators. *Nano letters* **20**, 585 (2019).

[15] B. Schrader. *Infrared and Raman spectroscopy: methods and applications*. John Wiley & Sons (2008).

[16] G. M. Barrow. *Introduction to Molecular Spectroscopy*. McGraw-Hill (1962).

[17] W. Suetaka and J. T. Yates Jr. *Surface infrared and Raman spectroscopy: methods and applications*, volume 3. Springer Science & Business Media (1995).

[18] B. C. Smith. *Fundamentals of Fourier transform infrared spectroscopy*. CRC press (2011).

[19] S. Schlücker. Surface-Enhanced raman spectroscopy: Concepts and chemical applications. *Angewandte Chemie International Edition* **53**, 4756 (2014).

[20] K. Ataka and J. Heberle. Biochemical applications of surface-enhanced infrared absorption spectroscopy. *Analytical and bioanalytical chemistry* **388**, 47 (2007).

[21] F. Neubrech, C. Huck, K. Weber, A. Pucci, and H. Giessen. Surface-enhanced infrared spectroscopy using resonant nanoantennas. *Chemical reviews* **117**, 5110 (2017).

[22] M. Mismar. Numerical Simulation of Maxwell's Equations. *IOSR Journal of Engineering* **7**, 01 (2017).

[23] Finite Difference IDE, ANSYS Lumerical Software ULC, Ansys, Inc., Vancouver, BC, Canada (2021).

[24] Finite Element IDE, ANSYS Lumerical Software ULC, Ansys, Inc., Vancouver, BC, Canada (2021).

[25] C. Bohren and D. Huffman. *Absorption and Scattering of Light by Small Particles.* Wiley Science Series. Wiley (2008).

[26] M. Mishchenko, L. Travis, and A. Lacis. *Scattering, Absorption, and Emission of Light by Small Particles.* Cambridge University Press (2002).

[27] M. Kerker and E. Loebl. *The Scattering of Light and Other Electromagnetic Radiation.* Elsevier Science (2016).

[28] G. Mie. Beiträge zur Optik trüber Medien, speziell kolloidaler Metallösungen. *Annalen der Physik* **330**, 377 (1908).

[29] M. Finazzi, P. Biagioni, M. Celebrano, and L. Duò. Quasistatic limit for plasmon-enhanced optical chirality. *Physical Review B* **91**, 195427 (2015).

[30] Y. Tang and A. E. Cohen. Optical chirality and its interaction with matter. *Physical review letters* **104**, 163901 (2010).

[31] L. Ghirardini. *Second Harmonic Generation Enhancement at the Nanoscale Using Plasmonic and Photonic Antennas.* Ph.D. thesis, Politecnico di Milano (2018).

[32] L. Novotny and B. Hecht. *Principles of nano-optics.* Cambridge university press (2012).

[33] Z. Sun and H. K. Kim. Refractive transmission of light and beam shapingwith metallic nano-optic lenses. *Applied Physics Letters* **85**, 642 (2004).

[34] J. M. McMahon, J. Henzie, T. W. Odom, G. C. Schatz, and S. K. Gray. Tailoring the sensing capabilities of nanohole arrays in gold films with Rayleigh anomaly-surface plasmon polaritons. *Optics express* **15**, 18119 (2007).

[35] X.-S. Lin and X.-G. Huang. Tooth-shaped plasmonic waveguide filters with nanometeric sizes. *Optics letters* **33**, 2874 (2008).

[36] R. F. Oulton, V. J. Sorger, D. Genov, D. Pile, and X. Zhang. A hybrid plasmonic waveguide for subwavelength confinement and long-range propagation. *nature photonics* **2**, 496 (2008).

[37] P. Biagioni, J.-S. Huang, and B. Hecht. Nanoantennas for visible and infrared radiation. *Reports on Progress in Physics* **75**, 024402 (2012).

[38] A. Boltasseva and H. A. Atwater. Low-loss plasmonic metamaterials. *Science* **331**, 290 (2011).

[39] A. Dazzi, F. Glotin, and R. Carminati. Theory of infrared nanospectroscopy by photothermal induced resonance. *Journal of Applied Physics* **107**, 124519 (2010).

[40] A. Dazzi and C. B. Prater. AFM-IR: Technology and applications in nanoscale infrared spectroscopy and chemical imaging. *Chemical reviews* **117**, 5146 (2017).

[41] N. Li and L. S. Taylor. Nanoscale infrared, thermal, and mechanical characterization of telaprevir–polymer miscibility in amorphous solid dispersions prepared by solvent evaporation. *Molecular pharmaceutics* **13**, 1123 (2016).

[42] F. Tang, P. Bao, and Z. Su. Analysis of nanodomain composition in high-impact polypropylene by atomic force microscopy-infrared. *Analytical chemistry* **88**, 4926 (2016).

[43] L. Baldassarre, V. Giliberti, A. Rosa, M. Ortolani, A. Bonamore, P. Baiocco, K. Kjoller, P. Calvani, and A. Nucara. Mapping the Amide I Absorption in Single Bacteria and Mammalian Cells with Resonant Infrared Nanospectroscopy. *Nanotechnology* **27**, 075101 (2016).

[44] C. Policar, J. B. Waern, M.-A. Plamont, S. ClÃšde, C. Mayet, R. Prazeres, J.-M. Ortega, A. VessiÃšres, and A. Dazzi. Subcellular IR Imaging of a Metal-Carbonyl Moiety Using Photothermally Induced Resonance. *Angewandte Chemie International Edition* **50**, 860 (2011).

[45] B. Lahiri, G. Holland, V. Aksyuk, and A. Centrone. Nanoscale Imaging of Plasmonic Hot Spots and Dark Modes with the Photothermal-Induced Resonance Technique. *Nano Letters* **13**, 3218 (2013). PMID: 23777547.

[46] J. Chae, B. Lahiri, and A. Centrone. Engineering near-field SEIRA enhancements in plasmonic resonators. *Acs Photonics* **3**, 87 (2016).

[47] R. Dong, Y. Fang, J. Chae, J. Dai, Z. Xiao, Q. Dong, Y. Yuan, A. Centrone, X. C. Zeng, and J. Huang. High-gain and low-driving-voltage photodetectors based on organolead triiodide perovskites. *Advanced materials* **27**, 1912 (2015).

[48] K. Gallacher, R. W. Millar, D. J. Paul, J. Frigerio, A. Ballabio, G. Isella, F. Rusconi, P. Biagioni, V. Giliberti, A. Sorgi, L. Baldassarre, and M. Ortolani. Characterization of integrated waveguides by atomic-force-microscopy-assisted mid-infrared imaging and spectroscopy. *Opt. Express* **28**, 22186 (2020).

[49] X. Chen, D. Hu, R. Mescall, G. You, D. Basov, Q. Dai, and M. Liu. Modern scattering-type scanning near-field optical microscopy for advanced material research. *Advanced Materials* **31**, 1804774 (2019).

[50] T. Schmid, L. Opilik, C. Blum, and R. Zenobi. Nanoscale chemical imaging using tip-enhanced Raman spectroscopy: a critical review. *Angewandte Chemie International Edition* **52**, 5940 (2013).

[51] D. Hu, M. Micic, N. Klymyshyn, Y. D. Suh, and H. P. Lu. Correlated topographic and spectroscopic imaging beyond diffraction limit by atomic force microscopy metallic tip-enhanced near-field fluorescence lifetime microscopy. *Review of scientific instruments* **74**, 3347 (2003).

[52] T. Takahashi and T. Kawamukai. Phase detection of electrostatic force by AFM with a conductive tip. *Ultramicroscopy* **82**, 63 (2000).

[53] T.-X. Huang, S.-C. Huang, M.-H. Li, Z.-C. Zeng, X. Wang, and B. Ren. Tip-enhanced Raman spectroscopy: tip-related issues. *Analytical and bioanalytical chemistry* **407**, 8177 (2015).

[54] F. Lu and M. A. Belkin. Infrared Absorption Nano-Spectroscopy Using Sample Photoexpansion Induced by Tunable Quantum Cascade Lasers. *Opt. Express* **19**, 19942 (2011).

[55] F. Lu, M. Jin, and M. A. Belkin. Tip-Enhanced Infrared Nanospectroscopy via Molecular Expansion Force Detection. *Nat. Photonics* **8**, 307 (2014).

[56] M. Jin and M. A. Belkin. Infrared vibrational spectroscopy of functionalized atomic force microscope probes using resonantly enhanced infrared photoexpansion nanospectroscopy. *Small Methods* **3**, 1900018 (2019).

[57] B. T. O'Callahan, J. Yan, F. Menges, E. A. Muller, and M. B. Raschke. Photoinduced Tip-Sample Forces for Chemical Nanoimaging and Spectroscopy. *Nano Lett.* **18**, 5499 (2018).

[58] Wolfram Mathematica 13.0, Wolfram Research, Inc., Champaign, Illinois, United States (2022).

[59] J. Chen, X. Xu, J. Zhou, and B. Li. Interfacial thermal resistance: Past, present, and future. *Reviews of Modern Physics* **94**, 025002 (2022).

[60] T. Taliercio and P. Biagioni. Semiconductor infrared plasmonics. *Nanophotonics* **8**, 949 (2019).

[61] A. I. Kuznetsov, A. E. Miroshnichenko, M. L. Brongersma, Y. S. Kivshar, and B. Luk'yanchuk. Optically resonant dielectric nanostructures. *Science* **354**, 2472 (2016).

[62] M. R. Hasan and O. G. Hellesø. Dielectric optical nanoantennas. *Nanotechnology* **32**, 202001 (2021).

[63] N. C. Panoiu, W. E. I. Sha, D. Y. Lei, and G.-C. Li. Nonlinear optics in plasmonic nanostructures. *Journal of Optics* **20**, 083001 (2018).

[64] M. Celebrano, X. Wu, M. Baselli, S. Großmann, P. Biagioni, A. Locatelli, C. De Angelis, G. Cerullo, R. Osellame, B. Hecht, L. Duó, F. Ciccacci, and M. Finazzi. Mode matching in multiresonant plasmonic nanoantennas for enhanced second harmonic generation. *Nature nanotechnology* **10**, 412 (2015).

[65] M. Celebrano, D. Rocco, M. Gandolfi, A. Zilli, F. Rusconi, A. Tognazzi, A. Mazzanti, L. Ghirardini, E. A. A. Pogna, L. Carletti, C. Baratto, G. Marino, C. Gigli, P. Biagioni, L. Duò, G. Cerullo, G. Leo, G. D. Valle, M. Finazzi, and C. D. Angelis. Optical tuning of dielectric nanoantennas for thermo-optically reconfigurable nonlinear metasurfaces. *Opt. Lett.* **46**, 2453 (2021).

[66] S. V. Li, D. G. Baranov, A. E. Krasnok, and P. A. Belov. All-dielectric nanoantennas for unidirectional excitation of electromagnetic guided modes. *Applied Physics Letters* **107**, 171101 (2015).

[67] G. Raschke, S. Kowarik, T. Franzl, C. Sönnichsen, T. A. Klar, J. Feldmann, A. Nichtl, and K. Kürzinger. Biomolecular Recognition Based on Single Gold Nanoparticle Light Scattering. *Nano Letters* **3**, 935 (2003).

[68] E. J. Smythe, M. D. Dickey, J. Bao, G. M. Whitesides, and F. Capasso. Optical Antenna Arrays on a Fiber Facet for in Situ Surface-Enhanced Raman Scattering Detection. *Nano Letters* **9**, 1132 (2009).

[69] M. Najem, F. Carcenac, T. Taliercio, and F. Gonzalez-Posada. Aluminum Bowties for Plasmonic-Enhanced Infrared Sensing. *Advanced Optical Materials* **10**, 2201025 (2022).

[70] L. Baldassarre, E. Sakat, J. Frigerio, A. Samarelli, K. Gallacher, E. Calandrini, G. Isella, D. J. Paul, M. Ortolani, and P. Biagioni. Midinfrared Plasmon-Enhanced Spectroscopy with Germanium Antennas on Silicon Substrates. *Nano Letters* **15**, 7225 (2015).

[71] S. Law, L. Yu, A. Rosenberg, and D. Wasserman. All-Semiconductor Plasmonic Nanoantennas for Infrared Sensing. *Nano Letters* **13**, 4569 (2013).

[72] V. N'Tsame Guilengui, L. Cerutti, J.-B. Rodriguez, E. Tournié, and T. Taliercio. Localized surface plasmon resonances in highly doped semiconductors nanostructures. *Applied Physics Letters* **101**, 161113 (2012).

[73] M. I. Stockman, K. Kneipp, S. I. Bozhevolnyi, S. Saha, A. Dutta, J. Ndukaife, N. Kinsey, H. Reddy, U. Guler, V. M. Shalaev, A. Boltasseva, B. Gholipour, H. N. S. Krishnamoorthy, K. F. MacDonald, C. Soci, N. I. Zheludev, V. Savinov, R. Singh, P. Groß, C. Lienau, M. Vadai, M. L. Solomon, D. R. Barton, M. Lawrence, J. A. Dionne, S. V. Boriskina, R. Esteban, J. Aizpurua, X. Zhang, S. Yang, D. Wang, W. Wang, T. W. Odom, N. Accanto, P. M. de Roque, I. M. Hancu, L. Piatkowski, N. F. van Hulst, and M. F. Kling. Roadmap on plasmonics. *Journal of Optics* **20**, 043001 (2018).

[74] V. G. Kravets, A. V. Kabashin, W. L. Barnes, and A. N. Grigorenko. Plasmonic Surface Lattice Resonances: A Review of Properties and Applications. *Chemical Reviews* **118**, 5912 (2018).

[75] V. Giannini, G. Vecchi, and J. Gómez Rivas. Lighting Up Multipolar Surface Plasmon Polaritons by Collective Resonances in Arrays of Nanoantennas. *Phys. Rev. Lett.* **105**, 266801 (2010).

[76] A. Abass, S. R.-K. Rodriguez, J. Gómez Rivas, and B. Maes. Tailoring Dispersion and Eigenfield Profiles of Plasmonic Surface Lattice Resonances. *ACS Photonics* **1**, 61 (2014).

[77] B. D. Thackray, V. G. Kravets, F. Schedin, G. Auton, P. A. Thomas, and A. N. Grigorenko. Narrow collective plasmon resonances in nanostructure arrays observed at normal light incidence for simplified sensing in asymmetric air and water environments. *Acs Photonics* **1**, 1116 (2014).

[78] A. I. Aristov, U. Zywietz, A. B. Evlyukhin, C. Reinhardt, B. N. Chichkov, and A. V. Kabashin. Laser-ablative engineering of phase singularities in plasmonic metamaterial arrays for biosensing applications. *Applied Physics Letters* **104**, 071101 (2014).

[79] C. Clavero. Plasmon-induced hot-electron generation at nanoparticle/metal-oxide interfaces for photovoltaic and photocatalytic devices. *Nature Photonics* **8**, 95 (2014).

[80] P. Frank, J. Srajer, A. Schwaighofer, A. Kibrom, and C. Nowak. Double-layered nanoparticle stacks for spectro-electrochemical applications. *Opt. Lett.* **37**, 3603 (2012).

[81] R. Sachan, A. Malasi, J. Ge, S. Yadavali, H. Krishna, A. Gangopadhyay, H. Garcia, G. Duscher, and R. Kalyanaraman. Ferroplasmons: Intense Localized Surface Plasmons in Metal-Ferromagnetic Nanoparticles. *ACS Nano* **8**, 9790 (2014).

[82] G. Vecchi, V. Giannini, and J. Gómez Rivas. Shaping the Fluorescent Emission by Lattice Resonances in Plasmonic Crystals of Nanoantennas. *Phys. Rev. Lett.* **102**, 146807 (2009).

[83] A. A. Yanik, A. E. Cetin, M. Huang, A. Artar, S. H. Mousavi, A. Khanikaev, J. H. Connor, G. Shvets, and H. Altug. Seeing protein monolayers with naked eye through plasmonic Fano resonances. *Proceedings of the National Academy of Sciences* **108**, 11784 (2011).

[84] L. Lin and Y. Zheng. Optimizing plasmonic nanoantennas via coordinated multiple coupling. *Scientific reports* **5**, 1 (2015).

[85] M. Yurkin and A. Hoekstra. The discrete dipole approximation: An overview and recent developments. *Journal of Quantitative Spectroscopy and Radiative Transfer* **106**, 558 (2007). IX Conference on Electromagnetic and Light Scattering by Non-Spherical Particles.

[86] S. Zou and G. C. Schatz. Narrow plasmonic/photonic extinction and scattering line shapes for one and two dimensional silver nanoparticle arrays. *The Journal of Chemical Physics* **121**, 12606 (2004).

[87] F. Mattioli, G. Mazzeo, G. Longhi, S. Abbate, G. Pellegrini, E. Mogni, M. Celebrano, M. Finazzi, L. Duó, C. G. Zanchi, M. Tommasini, M. Pea, S. Cibella, R. Polito, F. Sciortino, L. Baldassarre, A. Nucara, M. Ortolani, and P. Biagioni. Plasmonic Superchiral Lattice Resonances in the Mid-Infrared. *ACS Photonics* **7**, 2676 (2020).

[88] Y. Yang, I. I. Kravchenko, D. P. Briggs, and J. Valentine. All-dielectric metasurface analogue of electromagnetically induced transparency. *Nature communications* **5**, 1 (2014).

[89] A. Leitis, A. Tittl, M. Liu, B. H. Lee, M. B. Gu, Y. S. Kivshar, and H. Altug. Angle-multiplexed all-dielectric metasurfaces for broadband molecular fingerprint retrieval. *Science Advances* **5**, 2871 (2019).

[90] L. Carletti, D. Rocco, A. Locatelli, C. D. Angelis, V. F. Gili, M. Ravaro, I. Favero, G. Leo, M. Finazzi, L. Ghirardini, M. Celebrano, G. Marino, and A. V. Zayats. Controlling second-harmonic generation at the nanoscale with monolithic AlGaAs-on-AlOx antennas. *Nanotechnology* **28**, 114005 (2017).

[91] A. Alù, M. G. Silveirinha, A. Salandrino, and N. Engheta. Epsilon-near-zero metamaterials and electromagnetic sources: Tailoring the radiation phase pattern. *Phys. Rev. B* **75**, 155410 (2007).

[92] A. R. Davoyan, A. M. Mahmoud, and N. Engheta. Optical isolation with epsilon-near-zero metamaterials. *Opt. Express* **21**, 3279 (2013).

[93] J. Kim, A. Dutta, G. V. Naik, A. J. Giles, F. J. Bezares, C. T. Ellis, J. G. Tischler, A. M. Mahmoud, H. Caglayan, O. J. Glembocki, A. V. Kildishev, J. D. Caldwell, A. Boltasseva, and N. Engheta. Role of epsilon-near-zero substrates in the optical response of plasmonic antennas. *Optica* **3**, 339 (2016).

[94] I. Liberal and N. Engheta. Near-zero refractive index photonics. *Nature Photonics* **11**, 149 (2017).

[95] X. Niu, X. Hu, S. Chu, and Q. Gong. Epsilon-Near-Zero Photonics: A New Platform for Integrated Devices. *Advanced Optical Materials* **6**, 1701292 (2018).

[96] D. Rocco, C. De Angelis, D. De Ceglia, L. Carletti, M. Scalora, and M. Vincenti. Dielectric nanoantennas on epsilon-near-zero substrates: Impact of losses on second order nonlinear processes. *Optics Communications* **456**, 124570 (2020).

[97] N. Kinsey, C. DeVault, J. Kim, M. Ferrera, V. M. Shalaev, and A. Boltasseva. Epsilon-near-zero Al-doped ZnO for ultrafast switching at telecom wavelengths. *Optica* **2**, 616 (2015).

[98] H. Hajian, E. Ozbay, and H. Caglayan. Beaming and enhanced transmission through a subwavelength aperture via epsilon-near-zero media. *Scientific reports* **7**, 1 (2017).

[99] J. Yoon, M. Zhou, M. Badsha, T. Y. Kim, Y. C. Jun, C. K. Hwangbo, et al. Broadband epsilon-near-zero perfect absorption in the near-infrared. *Scientific reports* **5**, 1 (2015).

[100] M. Habib, D. Briukhanova, N. Das, B. C. Yildiz, and H. Caglayan. Controlling the plasmon resonance via epsilon-near-zero multilayer metamaterials. *Nanophotonics* **9**, 3637 (2020).

[101] C. T. DeVault, V. A. Zenin, A. Pors, K. Chaudhuri, J. Kim, A. Boltasseva, V. M. Shalaev, and S. I. Bozhevolnyi. Suppression of near-field coupling in plasmonic antennas on epsilon-near-zero substrates. *Optica* **5**, 1557 (2018).

[102] D. Briukhanova. *Plasmonic nanoantennas on Epsilon-Near-Zero Metamaterial substrates*. B.S. thesis (2020).

[103] Y. C. Jun, T. S. Luk, A. Robert Ellis, J. F. Klem, and I. Brener. Doping-tunable thermal emission from plasmon polaritons in semiconductor epsilon-near-zero thin films. *Applied Physics Letters* **105**, 131109 (2014).

[104] E. Alvear-Cabezón, T. Taliercio, S. Blin, R. Smaali, F. Gonzalez-Posada, A. Baranov, R. Teissier, and E. Centeno. Epsilon near-zero all-optical terahertz modulator. *Applied Physics Letters* **117**, 111101 (2020).

[105] R. Liu, C. M. Roberts, Y. Zhong, V. A. Podolskiy, and D. Wasserman. Epsilon-near-zero photonics wires. *ACS Photonics* **3**, 1045 (2016).

[106] P. Fehlen, G. Thomas, F. Gonzalez-Posada, J. Guise, F. Rusconi, L. Cerutti, T. Taliercio, and D. Spitzer. Gas sensing of organophosphorous compounds with III–V semiconductor plasmonics. *Sensors and Actuators B: Chemical* **376**, 132987 (2023).

[107] M. A. Herman and H. Sitter. *Molecular beam epitaxy: fundamentals and current status*, volume 7. Springer Science & Business Media (2012).

[108] Y. Chen. Nanofabrication by electron beam lithography and its applications: A review. *Microelectronic Engineering* **135**, 57 (2015).

[109] F. M. Huang, T. S. Kao, V. A. Fedotov, Y. Chen, and N. I. Zheludev. Nanohole Array as a Lens. *Nano Letters* **8**, 2469 (2008).

[110] A. Zilli, D. Rocco, M. Finazzi, A. Di Francescantonio, L. Duó, C. Gigli, G. Marino, G. Leo, C. De Angelis, and M. Celebrano. Frequency Tripling via Sum-Frequency Generation at the Nanoscale. *ACS Photonics* **8**, 1175 (2021).